EPFL

Thèse n° 8398

First indication of the Λ^0_b baryon decay to a charmless baryonic final state

Présentée le 5 novembre 2021

Faculté des sciences de base
Laboratoire de physique des hautes énergies OS
Programme doctoral en physique

pour l'obtention du grade de Docteur ès Sciences

par

Vladimir MACKO

Acceptée sur proposition du jury

Prof. F. Carbone, président du jury
Dr F. Blanc, Prof. T. Nakada, directeurs de thèse
Prof. S. Monteil, rapporteur
Dr E. Rodrigues, rapporteur
Prof. P. Crivelli, rapporteur

École
polytechnique
fédérale
de Lausanne

2021

To my parents…

Acknowledgements

First and foremost, my gratitude goes to my thesis supervisor, Fred Blanc. I am immensely thankful for his truly invaluable guidance, for all the explanations and priceless advice. Thank you Fred for everything you taught me, for finding time even during hectic weeks, for your incredible sense for details and for your critical yet constructive and humane way of thinking. Thank you for all your support throughout last nearly five years, I appreciate it greatly.

I am also very grateful to my second supervisor, Tatsuya Nakada, for giving me a rare gift of freedom – I could choose myself the topic of my research and my collaborators. I am genuinely thankful that I could work on a project in which I personally believed and where I could profit from my skills the most. Thank you very much Tatsuya. Thank you also for all your insightful questions and incredibly expert comments which helped me to understand my work better.

I would like to also thank other senior members of LPHE: Olivier Schneider, Aurelio Bay and Guido Hafaeli who, along with my supervisors, gave me a chance to do the PhD in this lab – I am truly thankful I could be part of it. Thank you for all your questions and discussions not only at the meetings but also during lunches and random coffee breaks.

Many thanks go also to Plamen Hopchev for introducing me to the scintillating fibre detector production at EPFL and explaining me all the technical details needed for its quality assurance.

My sincere appreciation goes to Eduardo Rodrigues for being a great collaborator throughout all the steps of my searches for purely baryonic decays. Thank you for adding practical aspects to our discussions and for all your expertise and invaluable advice, it helped a lot.

I am thankful to the members of Charmless Working group at CERN for all the lively discussions and for opportunities to give a presentation on behalf of the group which I very much enjoyed. In particular, I am very thankful to Daniel O'Hanlon for all his advice and expertise of charmless three-body decays. I am also very thankful to María Vieites Díaz for her effort as a simulation liaison that was greatly helpful in the early stages of the analysis, and for her help and great knowledge of fitting methods at the final analysis stages.

My thanks also go to Violaine Belle and many other young LHCb members for investing their time and effort in contributing to Starterkit – a small lighthouse reducing countless hours spent in the darkness of vast chaos called the *LHCb software*. I am happy you convinced me to help with my bit.

I have enjoyed my time at LPHE and it would be no near as great without its amazing and positive atmosphere – I am very thankful to my fellow students and post-docs which made our lab so great. Of course, I could not forget our wonderful secretaries Esther, Corinne and Erika which helped me immensely, way beyond one could expect. It is simple, amazing atmosphere is made by amazing people... In particular, I would like to thank Guido and Chitsanu for their friendly welcome in our office when I first arrived and for being always a great company. My thanks also go to my current office mates Sara, Serhii and Paul with whom I have enjoyed sharing office greatly too. It is such a pity we had so much time of home-office last year... Distinguished mentions belong to: Pali, Seb, Lino, Violaine, Veronica, María, Carina, Marie, Sonia, Surapat, Elena, Tara, Michel, Ettore, Alison, Matthieu, Philippe, Guillaume, Axel, Brice, Vincenzo, Olivier, Luca and so many others. Honourable credits go to Rita who gave me her honest personal opinions about dangers of choosing people to work with and her wholehearted recommendation to work with Fred. Thank you Rita, you were so right in every single point.

My very special thanks go to my awesome house mates, current and past, Seb, Michele, Thommaso, Gabriel, Clemens and Max. I am genuinely happy to live with you and that our house has always been such a good place to come back to after a long day.

My further thanks belong to my great friends which I could not see as often as I would want to but I know they are there anyway. Thank you Peter & Teresa, Jana, Fero, Edo, Peta, Mata, Martina, Juan, Thomas and Marcel.

Many thanks also to our Czechoslovak mini-community here in Lausanne. It has been so nice to have you around. My truly special thanks go to Eva & Dominik and, of course, Pali, I am so happy to have people like you in my life.

Last but definitely not least, my final words belong to my entire family and, in particular, my parents and my brother. For your care, for unconditional love and life-long support, you have my sincere and profound gratitude.

Lausanne, 30 July 2021 V. M.

Abstract

The Standard Model of particle physics provides predictions of many fundamental processes. One of them is the existence of charmless processes involving only baryons, namely charmless purely baryonic decays of baryons. Yet none of these decay modes has been experimentally observed so far. Following theoretically predicted branching fractions, the LHCb experiment is currently the only one capable of measurements concerning these rare decays. The work presented in this thesis describes the measurement techniques and the results of the study of Λ_b^0 baryon decays to a charmless baryonic final state using the LHCb detector involving the rare $\Lambda_b^0 \to \Lambda p \overline{p}$ and $\Xi_b^0 \to \Lambda p \overline{p}$ decays. The significance of existence of the $\Lambda_b^0 \to \Lambda p \overline{p}$ signal channel is found to be 4.82 σ, constituting the first evidence of existence of this channel. In the case of the $\Xi_b^0 \to \Lambda p \overline{p}$ channel the found significance is 2.26 σ, which is compatible with the non observation of this channel with the present level of statistics. Preliminary measurements of branching fraction of $\Lambda_b^0 \to \Lambda p \overline{p}$ are reported. In addition, the production of Scintillating Fibre (SciFi) Tracker, an essential part of the upgrade of the LHCb detector, is also discussed.

Key words: baryons, purely baryonic states, rare decays, branching fraction, hadrons, charmless decays, Large Hadron Collider, LHCb detector, CERN

Résumé

Le modèle standard de physique des particules fournit des prédictions pour de nombreux processus fondamentaux. L'une d'elles est l'existence de processus impliquant seulement des baryons sans quark c, à savoir des désintégrations purement baryoniques de baryons sans quark c. Pourtant, aucun de ces modes de désintégration n'a été observé expérimentalement jusqu'à présent. Suivant les rapports de branchement prédits théoriquement, l'expérience LHCb est actuellement la seule capable de mesurer ces désintégrations rares. Les travaux présentés dans cette thèse décrivent les techniques de mesure et les résultats de l'étude des processus de désintégration purement baryoniques sans quark c utilisant le détecteur LHCb et impliquant les désintégrations rares $\Lambda_b^0 \to \Lambda p\overline{p}$ et $\Xi_b^0 \to \Lambda p\overline{p}$. La significance de l'existence du mode de signal $\Lambda_b^0 \to \Lambda p\overline{p}$ est de 4.82 σ, constituant de la première évidence de l'existence de ce mode. Dans le cas du mode $\Xi_b^0 \to \Lambda p\overline{p}$, la significance obtenue est de 2.26 σ, qui est compatible avec la non observation de ce mode au niveau actuel de statistiques. Les résultats préliminaires des mesures de la fraction de branchement de $\Lambda_b^0 \to \Lambda p\overline{p}$ sont rapportés. De plus, la production du trajectographe à fibres scintillantes (appelé SciFi), un élément essentiel de la mise à niveau du détecteur LHCb, est également décrite.

Mots clefs : baryons, états purement baryoniques, désintégrations rares, rapport de branchement, hadrons, désintégrations sans charme, Large Hadron Collider, détecteur LHCb, CERN

Contents

1 Introduction

The Standard Model (SM) of particle physics, built on the principles of the Quantum Field Theory, is able to explain and predict the outcome of particle interactions at a very high level of precision [1, 2]. Despite the indisputable success of the SM and the recent important discovery of the Higgs boson [3, 4], the SM is not sufficient to fully describe the properties of elementary particles. Standard Model shortcomings include its inability to explain the absence of antimatter in the Universe [5], the neutrino masses [6], the presence of Dark Matter [7], as well as its incompleteness in terms of gravitational interactions. Furthermore, there are still some unexplored *corners* of the SM, which are accessible and in which predictions can be tested. It is, therefore, essential to conduct measurements in order to better understand the nature of elementary particles, limitations of the SM and possibly shed light on physics beyond the SM. However, to make these measurements possible, advanced experimental facilities are required. Furthermore, these facilities must be regularly upgraded in order to achieve state-of-the-art results.

It is known that all the stable hadrons in the Universe are baryons. Therefore, examination of SM predictions concerning processes involving baryons and their properties is of particular interest. One of these predictions is the existence of processes involving only charmless baryons, *charmless purely baryonic decays*. Yet none of these decay modes has been experimentally observed so far, therefore they constitute an unexplored class of decays.

One of the simplest modes of this kind is the decay $\Lambda_b^0 \to n p \overline{p}$. However, due to the presence of a hardly identifiable neutron in the final state, other modes like $\Lambda_b^0 \to \Lambda p \overline{p}$ or $\Xi_b^0 \to \Lambda p \overline{p}$ are more suitable to study properties of these decays. In case of a successful first observation of any of these processes, it might be possible to measure the corresponding branching fraction and allow for the first measurements of *CP* violation in charmless purely baryonic decays, which could be compared with theoretical predictions [8]. Furthermore, these decays might provide an opportunity to study the baryonic structure of intermediate resonance bound states [9, 10]. However, the ability to perform these measurements is strongly dependent of the availability of sufficient experimental statistics.

This thesis presents the experimental search for the charmless purely baryonic decay processes $\Lambda_b^0 \to \Lambda p \overline{p}$ with data collected between 2015 and 2018 by the LHCb experiment, as well as the work on a scintillating fibre tracker production.

2 Motivation for the search for charmless purely baryonic decays

This chapter provides a brief overview of the leading theory in the domain of particle physics followed by a short summary of theoretical predictions relevant to the study of charmless purely baryonic decays of baryons.

2.1 The Standard Model of particle physics

The Standard Model of particle physics represents a description of elementary particles and their interactions in terms of a relativistic quantum field theory. In the framework of the SM, fundamental particles with half-integer spin, so-called fermions, constitute the building blocks of matter. Fermions are divided into quarks and leptons based on how they interact with other SM particles. There are six quark types and six lepton types differing in their *flavour* quantum numbers and they are organised into three generations. For each fermion, there is also an *anti-particle* - a particle which has all quantum numbers indicating additive charges (electric charge, colour charge) opposite to those of the corresponding particle. For instance, the antiparticle of the bottom quark b is an anti-bottom quark, noted $\bar{b}$ [1].

The exchange of force mediator bosons, particles with integer spin, describes in the SM the fundamental interactions between the elementary particles. To be specific, the SM provides description of three following interactions [1]:

- Electromagnetic interaction, mediated by the massless photon, affects the electrically charged particles. Its range is infinite. Thanks to this interaction, atoms can be formed by bounding electrons to atomic nuclei. The theory of quantum electrodynamics provides a very-well-verified description of electromagnetic interactions.
- Weak interaction, with Z^0 and $W^{\pm}$ bosons as mediators, affect all fermions. However, due to the relatively high mass of these bosons, the range of the weak interaction reaches only 10^{-18} m. It is commonly observed in radioactive decays.
- Strong interaction mediated by *gluons*, which are massless bosons carrying no electric charge. Nevertheless, there is the so-called *colour charge* which gluons do carry. Following the SU(3) symmetry of the SM, eight combinations of colour and anti-colour

quantum numbers are allowed resulting in eight types of gluons. Given that both colour and anti-colour charge can be carried by a gluon, self-interactions are also possible. The range of the strong interaction reaches approximately 10^{-15} m. On the other hand, its intensity grows with increasing distance between the quarks. As a consequence, strong interactions of quarks on short distances is negligible to the first order resulting in *asymptotic freedom* of quarks. Also, thanks to the gluon field retention, the distance between the quarks is limited by the *confinement radius*. As the colour neutrality is observed in all stable particles, quarks are always confined into colourless *hadrons*. Hadrons are divided into two dominant groups: *baryons*, composite states of three quarks, and *mesons*, states of a quark and an anti-quark. Strong interactions, described by the theory of quantum chromodynamics, not only give rise to hadron formation but also to the residual field responsible for binding neutrons and protons into nuclei in the atomic cores.

In addition to the force mediation bosons, the SM includes also the *Higgs boson* [2] as a key component. The existence of the Higgs boson serves as evidence for the *Brout-Englert-Higgs mechanism*, which gives rise to the masses of the elementary particles in the SM [2]. The Higgs boson was experimentally discovered in 2012 as the last of the SM particles [3, 4, 11].

The complete overview of elementary particles in the SM summarising also their standard properties (invariant mass, electric charge and spin) is given in Fig. 2.1.

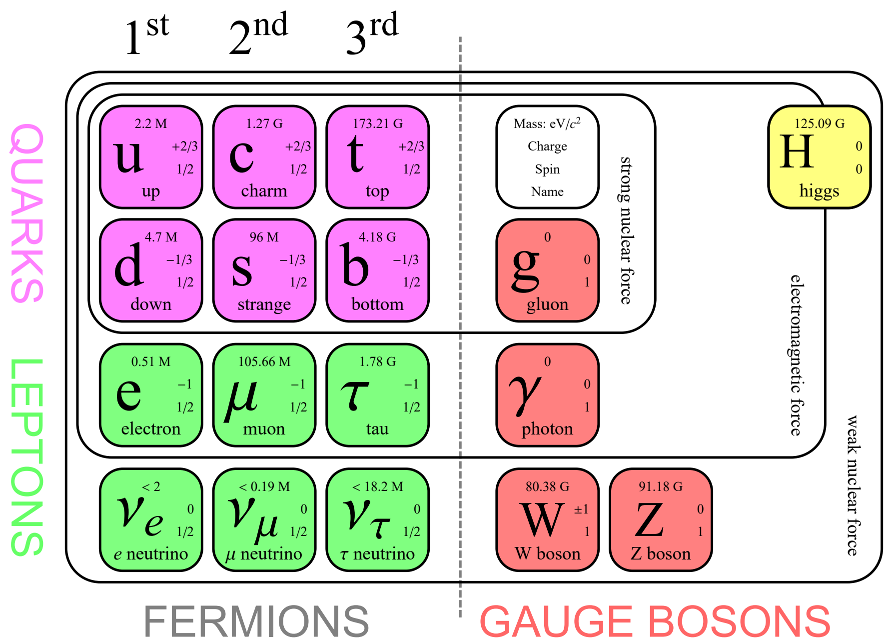

Figure 2.1 – Overview of elementary particles in the SM summarising also their standard properties: invariant mass, electric charge and spin. Figure taken from Ref. [12].

2.1.1 Shortcomings of the Standard model

Many experimental results are predicted by the SM with high accuracy. Nevertheless, there are phenomena which indicate that the SM is not complete. For example, it does not provide answers to the questions concerning the observation of *Neutrino oscillations*, the *Baryon number asymmetry* - asymmetry between amounts of ordinary matter and anti-matter in the universe - nor the origin of *dark matter* and the *dark energy* established by cosmological observations [1, 2]. Also, the *fine-tuning* of the fundamental parameters of the SM is another imperfection of the theory. While these shortcomings are already known, the SM predictions continue to be tested in hope to identify the limits of the SM and, hence, understand better the features of a future more complete theory.

2.2 Purely baryonic decays of baryons

The origin of the baryon number asymmetry of ordinary matter remains unknown to the present day. This motivates studies leading to deeper understanding of the nature of baryons. One of them could be the study of *purely baryonic decays of baryons* in which a baryon decays into a final state containing only baryons [8]. While first charm decay modes have been already observed [13], the charmless sector of purely baryonic decays remains unexplored [6]. Following baryon number conservation, processes of this kind must lead to final states that contain at least 3 baryons, such as $B_h \to B_{l1}\overline{B}_{l2}B_{l3}$ where h denotes a decaying heavy hadron and l_i denote light spin 1/2 baryons [9]. In view of the known conservation laws, the simplest decays of this kind are $\Lambda_b^0 \to p\overline{p}n$, $\Lambda_b^0 \to \Lambda\overline{\Lambda}\Lambda$ and the corresponding variants with $\Xi_b^{0,-}$ baryons as a decaying particle [8]. However, these decays are experimentally difficult to measure. Suitable alternatives for experimental searches are the decay channels $\Lambda_b^0 \to \Lambda p\overline{p}$ and $\Xi_b^0 \to \Lambda p\overline{p}$, which lead to more easily reconstructed final states. Theoretical calculations give the following branching fraction predictions [14]:

$$\mathscr{B}(\Lambda_b^0 \to \Lambda p\overline{p}) = (3.2^{+0.8}_{-0.3} \pm 0.4 \pm 0.7) \times 10^{-6}$$

$$\mathscr{B}(\Xi_b^0 \to \Lambda p\overline{p}) = (1.4 \pm 0.1 \pm 0.1 \pm 0.4) \times 10^{-7},$$

where the uncertainties are associated with non-factorisable effects, CKM matrix elements, and hadronic form factors, respectively. Describing Feynman diagrams of the signal channel $\Lambda_b^0 \to \Lambda p\overline{p}$ are presenting in Fig. 2.2.

The LHCb experiment at CERN is currently the only experiment capable of examining these rare processes [14]. If their existence is established, they would constitute an unexplored territory for future charge-parity, CP, asymmetry measurements. These measurements could challenge the theoretical predictions claiming the following direct CP asymmetry[I] values [14]:

$$\mathscr{A}_{CP}(\Lambda_b^0 \to \Lambda p\overline{p}) = (3.4 \pm 0.1 \pm 0.1 \pm 1.0)\%$$

[I] Examples of experimental techniques of direct CP asymmetry measurements can be found in Ref. [15, 16]

$$\mathscr{A}_{CP}(\Xi_b^0 \to \Lambda p\overline{p}) = (-13.0 \pm 0.5 \pm 1.5 \pm 1.1)\%.$$

The stated uncertainties correspond to non-factorisable effects, the experimental knowledge of the CKM matrix elements, and the hadronic form factors.

Furthermore, if the existence of charmless purely baryonic decays of baryons is confirmed, it would allow for studies of the dibaryon invariant mass spectra in the decay products searching for possible intermediate resonant states. This could help understanding further the *enhancement at the production threshold* observed in the dibaryonic sub-systems in decays of B mesons [17]. More recent examples of this enhancement are also observed in the LHCb experiment in the decays $B_s^0 \to p\overline{\Lambda}K^-$ [18] and $B_s^0 \to p\overline{p}h^+h^{'-}$ [19]. Branching fractions of these decay modes are of the order of 10^{-6}, for example:

$$\mathscr{B}(B_s^0 \to p\overline{\Lambda}K^-) + \mathscr{B}(\overline{B}_s^0 \to \overline{p}\Lambda K^+) = [5.46 \pm 0.61 \pm 0.57 \pm 0.50(\mathscr{B}) \pm 0.32(f_s/f_d)] \times 10^{-6},$$

where the uncertainties are stated in the following order: statistical, systematic, experimental uncertainty on the branching fraction of the $B^0 \to \overline{\Lambda}\pi^-$ decay used for normalisation, uncertainty on the knowledge of the ratio of b-quark hadronisation probabilities f_s/f_d.

These branching fractions are similar to that predicted for the charmless purely baryonic

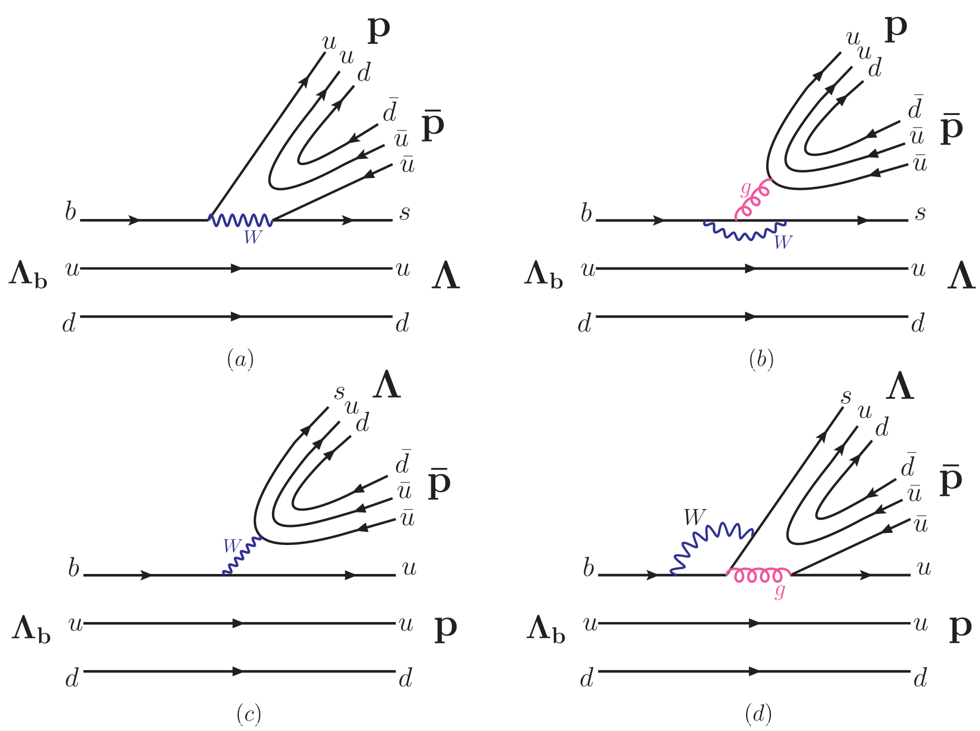

Figure 2.2 – Feynman diagrams describing the purely baryonic decays. Figures taken from Ref. [14].

Table 2.1 – A list of branching fractions of established decay channels which are topologically close to the studied channels $\Lambda_b^0 \to \Lambda p\overline{p}$ and $\Xi_b^0 \to \Lambda p\overline{p}$. Values taken from Ref. [6] and Ref. [20].

Decay channel	Branching fraction
$\Lambda_b^0 \to \Lambda\pi^+\pi^-$	$(4.7 \pm 1.9) \times 10^{-6}$
$\Lambda_b^0 \to \Lambda K^+\pi^-$	$(5.7 \pm 1.3) \times 10^{-6}$
$\Lambda_b^0 \to \Lambda K^+ K^-$	$(15.9 \pm 2.6) \times 10^{-6}$
$B^0 \to p\overline{K}^0\pi^-$	$(13 \pm 4) \times 10^{-6}$
$B^0 \to p\overline{\Lambda}\pi^-$	$(3.14 \pm 0.29) \times 10^{-6}$

decay of $\Lambda_b^0 \to \Lambda p\overline{p}$. Theoretically predicted enhancements at the production threshold in the charmless purely baryonic decays of $\Lambda_b^0 \to \Lambda p\overline{p}$ and $\Xi_b^0 \to \Lambda p\overline{p}$ are illustrated in Fig. 2.3.

For comparison, a list of branching fractions of established decay channels that are topologically close to the studied channels $\Lambda_b^0 \to \Lambda p\overline{p}$ and $\Xi_b^0 \to \Lambda p\overline{p}$ is provided in Table 2.1.

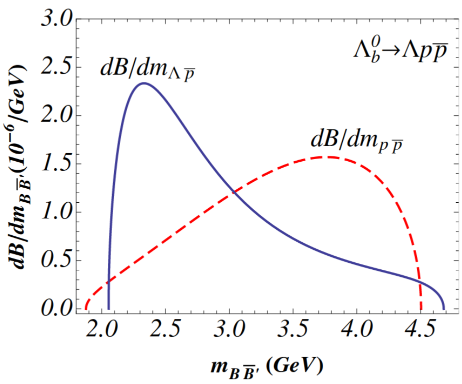

(a) $\Lambda_b^0 \to \Lambda p\overline{p}$.

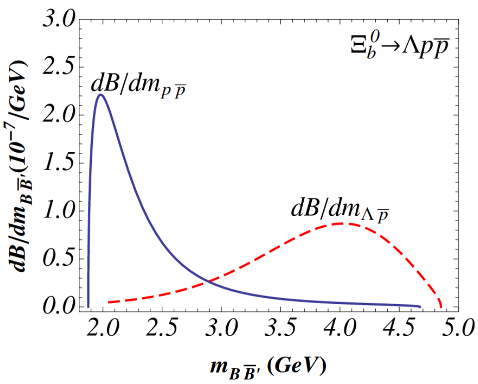

(b) $\Xi_b^0 \to \Lambda p\overline{p}$.

Figure 2.3 – The dibaryon invariant-mass spectra for the (a) $\Lambda_b^0 \to \Lambda p\overline{p}$ featuring threshold-enhanced $\Lambda\overline{p}$-system (blue) and $p\overline{p}$-system (red) and (b) $\Xi_b^0 \to \Lambda p\overline{p}$ featuring threshold-enhanced $p\overline{p}$-system (blue) and $p\Lambda$-system (red). Figures taken from Ref. [14].

3 Experimental apparatus

The work presented in this thesis is based on the data collected by the *LHCb* detector at the Large Hadron Collider (LHC) located at the European Organisation for Nuclear Research (CERN). This chapter provides an overview of these experimental facilities.

3.1 The Large Hadron Collider

The LHC [21], built at CERN at the Swiss-French border near Geneva , is currently the largest particle accelerator in the world. It is designed to deliver proton-proton collisions at the energy of 14 TeV (or heavy Pb ions with an energy of 2.8 TeV per nucleon) to its interaction points where the main experiments, *ATLAS*, *CMS*, *ALICE* and *LHCb*, are built.

In order to produce collisions at these high energies, particles must have certain kinetic energy already at the injection to the LHC. This implies the need for a pre-acceleration system. The complete chain of acceleration is illustrated in Fig. 3.1 and is part of the CERN accelerator complex. Its major parts are:

- A hydrogen gas bottle serving as a source of protons.
- Linear accelerator *Linac2* accelerating protons to an energy of 50 MeV.
- *Proton Synchrotron Booster (Booster)* accelerating protons further to 1.4 GeV.
- *Proton Synchrotron (PS)* where energy of protons is increased to 25 GeV.
- *Super Proton Synchrotron (SPS)* providing the final acceleration to 450 GeV of protons before they are delivered to the LHC beam pipes.

Besides the energy, accelerators are characterised by another key quantity for experimental purposes - *the luminosity*. Let two bunches of particles containing n_1 and n_2 particles characterised by transverse beam size root mean squares (RMS) σ_x and σ_y collide in an accelerator with a frequency of collision f_c, then the instantaneous luminosity is defined as:

$$L = f_c \frac{n_1 n_2}{4\pi\sigma_x\sigma_y}. \tag{3.1}$$

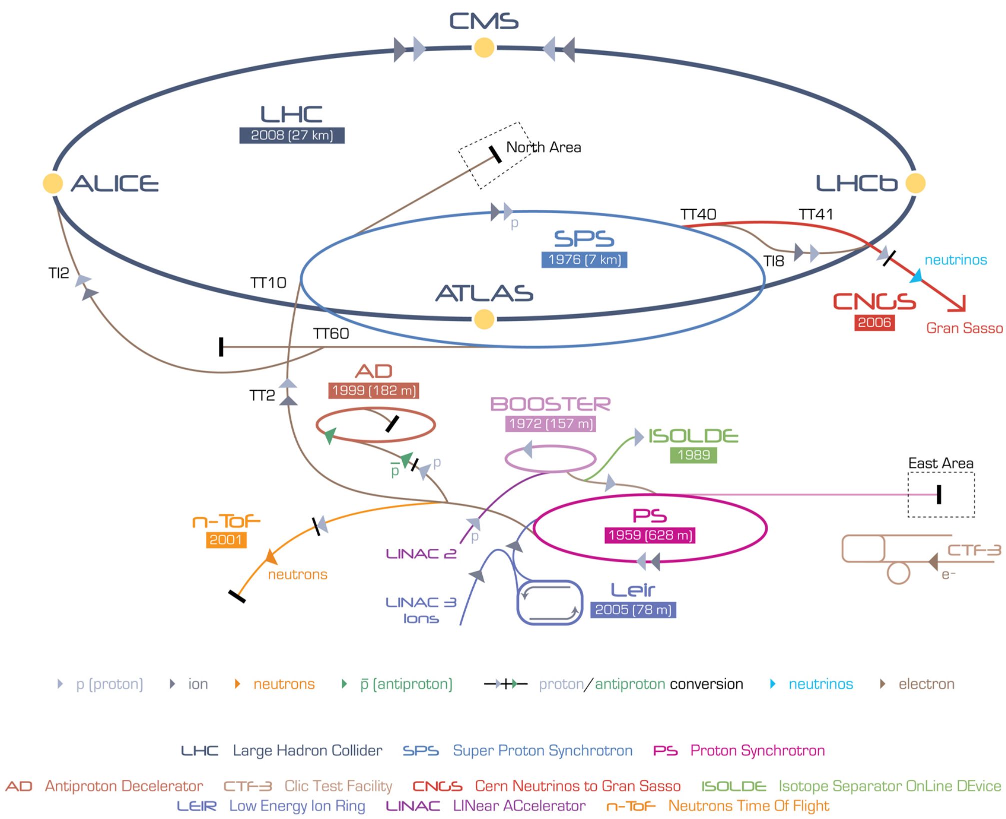

Figure 3.1 – Scheme of the CERN accelerator complex. Figure taken from Ref. [22].

More commonly used *time integrated luminosity* $\mathscr{L}$, is defined as

$$\mathscr{L} = \int L \mathrm{d}t. \tag{3.2}$$

One can link it with the experimental reconstruction efficiency ϵ and the cross-section of the studied process σ to obtain the number of reconstructed events N in an experiment:

$$N = \epsilon \sigma \mathscr{L}. \tag{3.3}$$

3.2 The LHCb detector

The LHCb detector [23], illustrated in Fig. 3.2, is a single-arm forward spectrometer covering the pseudo-rapidity range $2<\eta<5$. It is designed for the study of particles containing b or c quarks. Hadrons containing b or c quarks can be used for flavour physics measurements, such as high-precision measurements of rare decays and *CP* violation, and hence, to search for new physics phenomena [23].

The LHCb detector consists of a vertex detector, a tracking system combining silicon strip

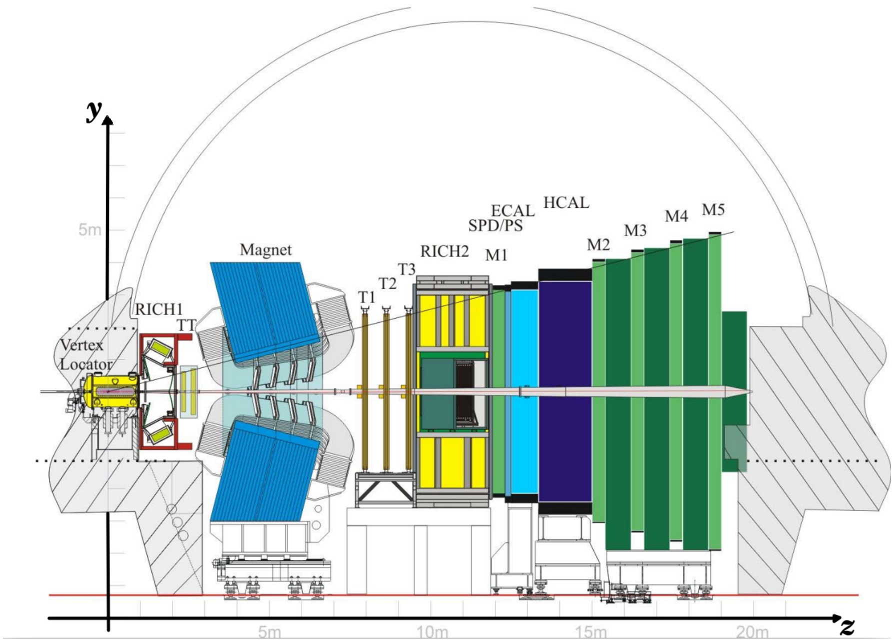

Figure 3.2 – View of the LHCb detector [23].

and straw tube detectors upstream of the magnet, two ring imaging Cherenkov detectors, the electromagnetic and hadronic calorimeters, and a muon system. A right-handed coordinate system is used to described the LHCb detector: origin of the coordinate system at the interaction point, z-axis follows the beam line in direction of the spectrometer, x-axis in the horizontal direction and y-axis is upward in the vertical direction.

The following sections provide a concise description of the main subsystems of the LHCb detector based on the full description provided in Ref. [23].

3.2.1 Tracking system

Precise reconstruction of the trajectories of charged particles is essential for the measurements performed with the LHCb detector. Trajectories are described by *tracks* in the detector. These are curved lines reconstructed from points, so called *hits*, where charged particles interacted with the detector active material. Tracks are also used to reconstruct decay vertices of particles decaying in the detector, which is crucial for the reconstruction of the full decay topology in each registered event.

In order to reconstruct tracks and decay vertices of the charged particles traversing the detector, a tracking system featuring the following sub-detectors is deployed:

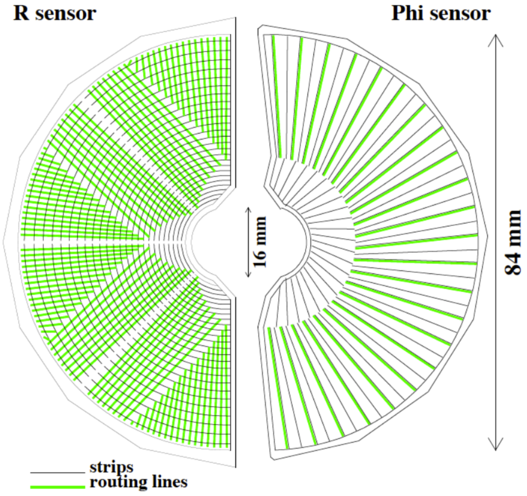

Figure 3.3 – Cross-section in the xz-plane at y=0 of the sensors and a view of the sensors in the xy-plane. The detector is shown in its closed position. Figure taken from Ref. [24].

The Vertex Locator (VELO)

The Vertex Locator (VELO) is a detector designed to precisely measure the trajectory of charged particles. It is installed in the region (approximately 1 m along the beam pipe) surrounding the interaction point to allow for precise determination of the primary and secondary vertices of short-lived particles. The VELO is built from 21 circular silicon micro-strip detector modules presented in Figs. 3.3 and 3.4. They are designed to determine the azimuthal angle and radial distance of points where a particle traversed the detector, and the z-coordinates which are obtained from the module location.

The VELO is composed of two separate halves which can be positioned in two configurations: Firstly, *Open* - there is a distance of 6 cm between the halves in order to prevent the radiation damage of the active materials in the VELO after the LHC beam injection and when the particle beams of LHC are not in a stable regime. Secondly, *Closed* - there is no distance between the

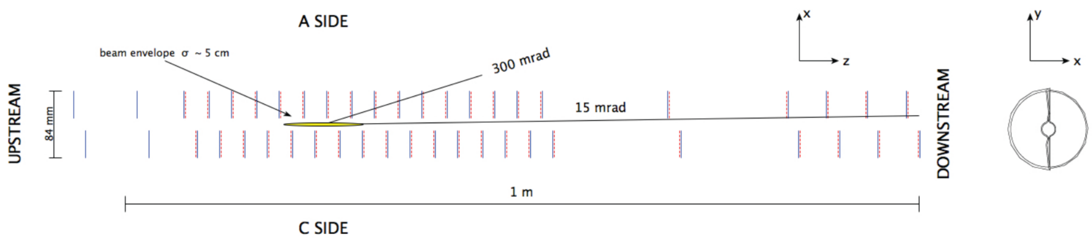

Figure 3.4 – Schematic representation of an R and a Φ sensor. The R sensor strips are arranged into four approximately 45° segments and have routing lines perpendicular to the strips. The Φ sensor has two zones with inner and outer strips. The routing lines of the inner strips are orientated parallel to the outer strips. Figure taken from Ref. [24].

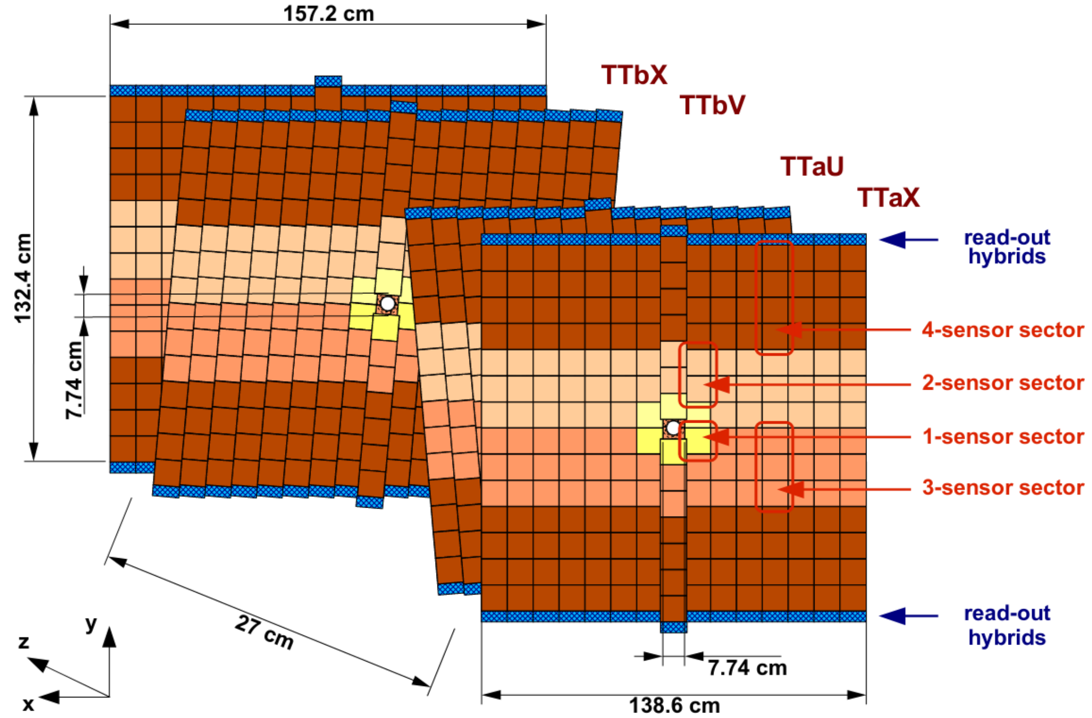

Figure 3.5 – Layout of the TT, with the LHC beam pipe passing through an opening in the centre of the detection layers. The four detection layers are labelled TTaX, TTaU, TTbV and TTbX. The four different types of read-out sectors employed in each of the detection layers are indicated by different shading: read-out sectors close to the beam pipe consist of a single silicon sensor,other read-out sectors consist of two, three or four silicon sensors that are connected together in series. Figure taken from Ref. [26].

halves as they are placed in contact to provide the best coverage of the area during data taking, and the first channels are as close as 8 mm of the beamline [25].

The Tracker Turicensis

The Tracker Turicensis (TT) is a detector which consists of two planar tracking stations. Each station contains two layers of silicon micro-strip sensors: one layer with vertically aligned strips and another with strip directions tilted at the angle of $\pm 5°$ with respect to the vertical direction as illustrated in Fig. 3.5. The TT is installed upstream of the magnet, described in Section 3.2.2.

The Inner Tracker

The Inner tracker (IT) is composed of three tracking stations (T1–T3), each shaped in cross-like surface centred around the beam pipe as illustrated in Fig. 3.6. It is placed in the area between

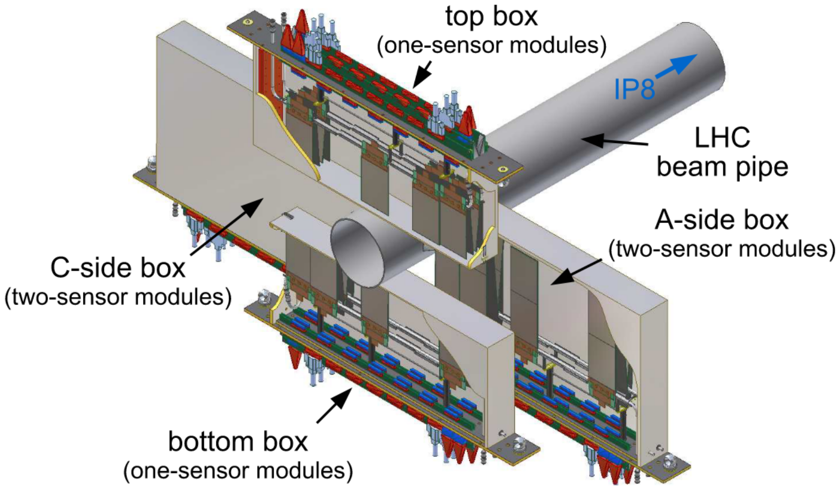

Figure 3.6 – View of the four IT detector boxes arranged around the LHC beam pipe. Figure taken from Ref. [23].

the magnet and the *RICH2* sub-detector (see Section 3.2.3). The stations consist of a single-sided silicon micro-strip based sensors designed to withstand high occupancy and radiation damages associated with high flux of charged particles from the collision point ($\approx 20\%$ of all produced).

The Outer tracker

The Outer tracker (OT), shown in Fig. 3.7, is a drift-time detector composed of straw gas drift tubes. The OT is arranged in three stations which extend the coverage of the IT and hence provide tracking information about the tracks further from the beam pipe. Each station is formed from four detection layers built up from 18 detector modules each. The first and last layers in each station are vertically aligned while central layers are tilted by $\pm 5°$.

Tracks in the LHCb detector

Depending on the trajectory of the particle and number of sub-detectors where it interacted, the reconstructed track belongs to one of the following categories as illustrated in Fig. 3.8:

- *Long tracks* are reconstructed from hits in all tracking systems, which allows for the most precise particle momentum measurement.
- *Upstream tracks* originate from particles which interacted only with VELO and TT and are mostly used as inputs to PID algorithms in order to better discriminate backgrounds.
- *Downstream tracks* originate from long-lived, for example Λ baryons or K_S mesons, particles which decay after traversing VELO and leave hits in TT and T1–T3 stations.

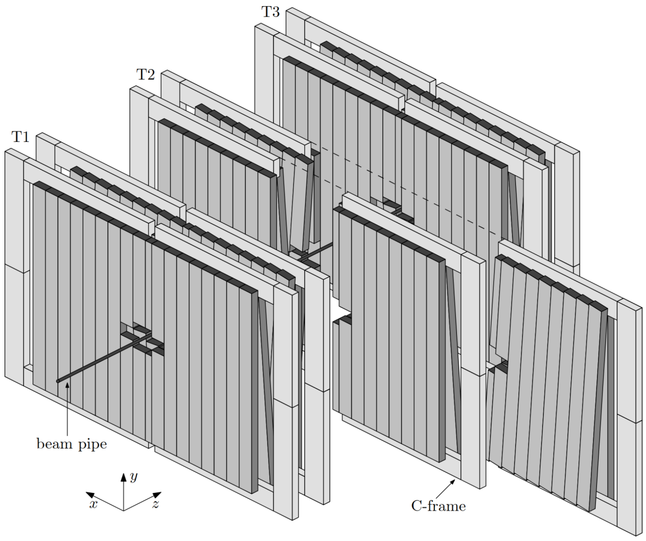

Figure 3.7 – Arrangement of OT straw-tube modules in layers and stations. Figure taken from Ref. [27].

- *VELO tracks* interacted only in VELO given they are created by particles which likely leave it at large angles or even in the backward direction. Nevertheless, these tracks are crucial for primary vertex reconstruction.
- *T tracks* traverse only the T-stations. They likely originate from secondary interactions and serve as addition of information for particle identification.

3.2.2 Magnet

In order to allow for precise measurements of momenta of charged particles, a suitable, well characterised magnetic field is needed. This is managed by a conventional warm dipole magnet placed between the first and the second tracking station (TT and T1) at the distance of approximately 5 m from the interaction point [28]. It delivers the integrated magnetic field with a magnitude of 4 Tm. The main component of the magnetic field follows the direction of y-axis, hence, charged particles bend in the $x-z$ plane. In order to minimise potential biases from possible asymmetries in the detector, the magnet is operated at two different polarities: Data taking with the configurations *MagUp* or *MagDown* indicate that the magnetic field was oriented in the positive or negative y-axis direction, respectively. Illustration of the magnetic field profile is shown in Fig. 3.8

3.2.3 Particle identification

Particle identification (PID) is essential for decay topology reconstruction and hence is crucial for the LHCb physics program. In order to identify the nature of the final state particles (pions,

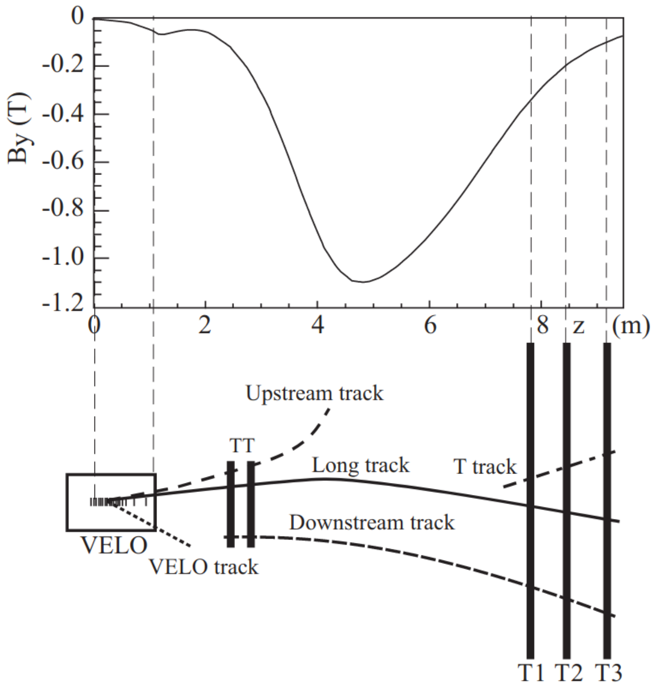

Figure 3.8 – A schematic illustration of the various track types: long, upstream, downstream, VELO and T tracks. For reference the main B-field component (By) is plotted above as a function of the z-coordinate. Figure taken from Ref. [29].

kaons, protons, muons, etc.), the following sub-detectors are in use:

The Ring Imaging Cherenkov detectors

Two *Ring Imaging Cherenkov (RICH) detectors* assure coverage of the full range of particle momentum: While, low momentum (1 – 60 GeV) particles are registered by *RICH1* (see Fig. 3.9a) located upstream of the magnet, those with high momentum (~ 15 – 100 GeV and beyond) are measured by *RICH2* (see Fig. 3.9b) located downstream of the magnet. The measured Cherenkov angle depends on particle momentum and the type of the particle. Therefore, particle types can be identified from the measured Cherenkov angle using the momentum values obtained from tracking detectors as illustrated in Fig. 3.10.

Calorimeters

Electromagnetic and hadronic calorimeters, as shown in Fig. 3.11, are designed to measure the energy of particles such as electrons, photons and hadrons (protons, kaons, pions, etc.). Furthermore, they provide additional information about their nature as each particle type leads to a different detection pattern. Examples of these patterns can be seen in Fig. 3.12. To be specific, calorimeters detect particle showers propagating through alternating layers of active detector

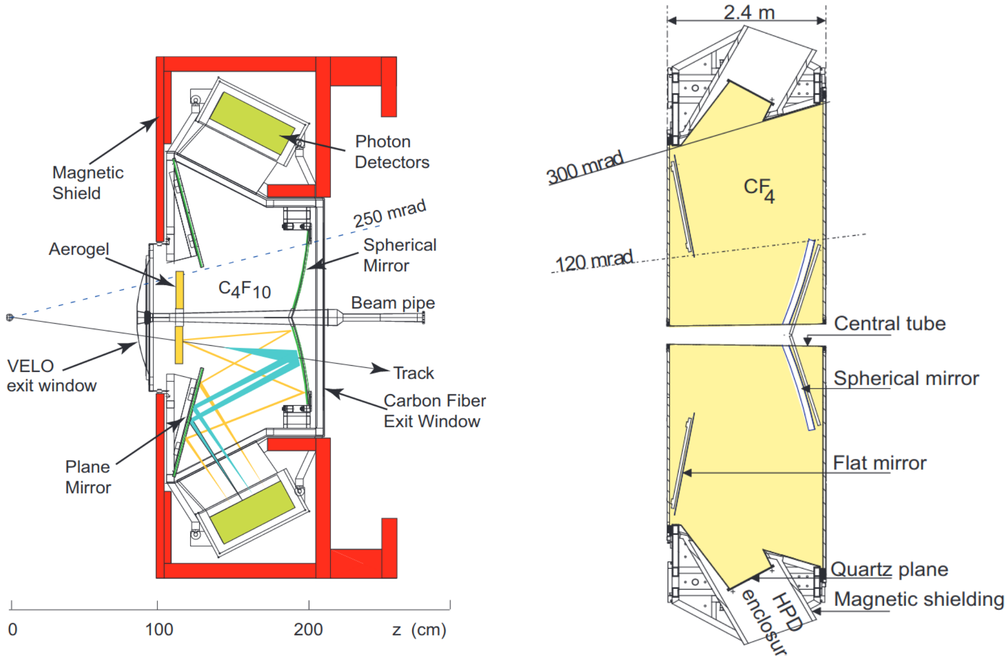

(a) Side view schematic layout of the RICH 1 detector.

(b) Top view schematic of the RICH 2 detector.

Figure 3.9 – Illustrations of the RICH 1 and RICH 2 detectors. Figures taken from Ref. [23].

materials and layers of absorber (lead in Electromagnetic and iron in hadronic calorimeter). In order to better differentiate electromagnetic an hadronic particles, a pre-shower (PS) detector and Scintillating Pad Detectors (SPD) are installed in front of the electromagnetic calorimeter. They are not only intended to start the electromagnetic showers when photons or electrons reach them but also assure longitudinal separation and hence increase discrimination from pions.

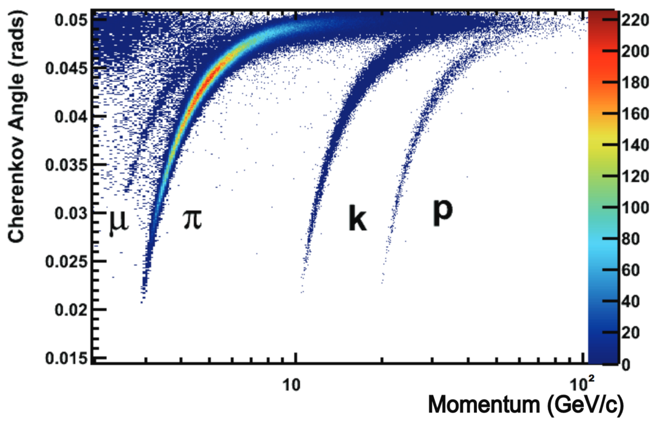

Figure 3.10 – Reconstructed Cherenkov angle as a function of track momentum in the C_4F_{10} radiator of *RICH1*. Figure taken from Ref. [29].

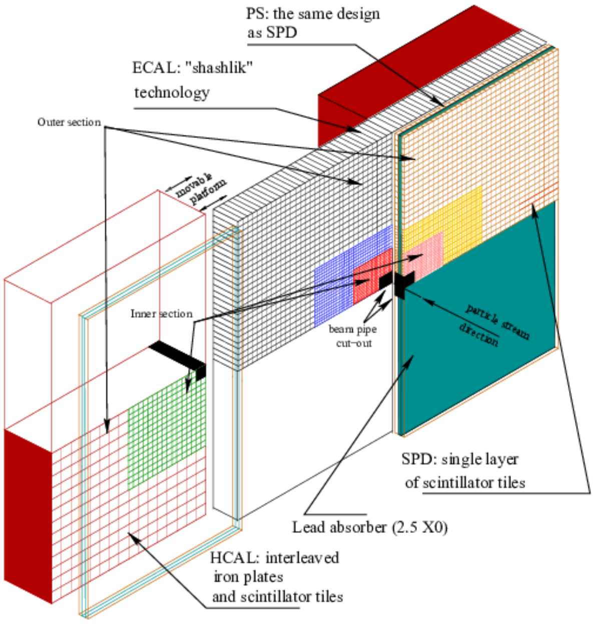

Figure 3.11 – Layout of the calorimeter system. Figure taken from Ref. [30].

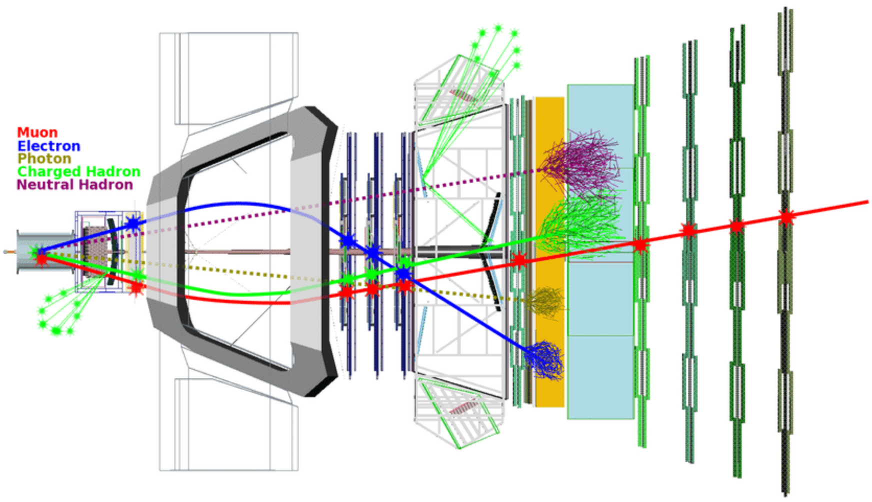

Figure 3.12 – Schematic view of the different particle signatures in the LHCb detector,with corresponding hits in the tracking system and muon stations, rings in the RICH and showers in the calorimeter. Figure taken from Ref. [31].

Muon system

The *Muon system* in LHCb consists of Multi-Wire Proportional chamber detectors arranged in 5 stations (M1–M5) and Gas Electron Multiplier detectors installed in the high occupancy

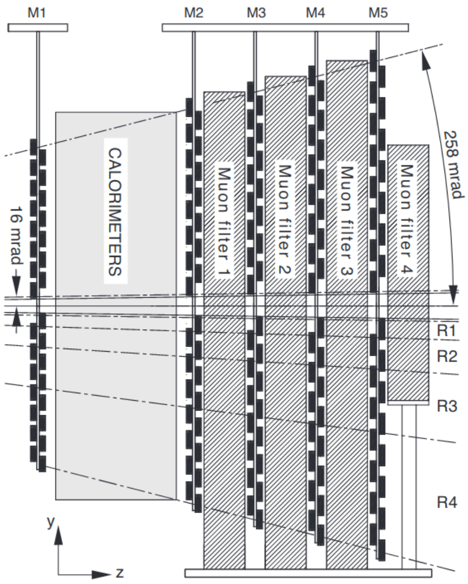

Figure 3.13 – Side view of the muon system. Figure taken from Ref. [23].

region in the centre of the first station, M1. While the M1 station is placed just after the *RICH2* detector, stations M2–M5 are at the end of the LHCb detector, with layers of absorber material (filters) placed in between them as illustrated in Fig. 3.13. The Muon system assures measurement of muon trajectories and also constitutes an important element of the LHCb trigger system thanks to its fast response.

3.2.4 The Trigger system

The LHC delivers particle collisions at a rate reaching 40 MHz to the LHCb detector. However, the vast majority of them contains no relevant information for the scientific searches and precision measurements and, therefore constitute *background*. Furthermore, given the limited storage space of the experiment it is not possible to record events at this rate. Therefore, a fast decision needs to be taken imminently after the collision, indicating whether the collision event is going to be recorded or discarded. For this purpose, a *Trigger system* is deployed. The trigger system of the LHCb detector consists of three consecutive stages of decisions. Depending on the type of events of interest, each physics analysis requires a specific set of selection requirements, so called *Trigger Lines* at each trigger stage. Generally, an event is recorded for later processing only if it passes at least one trigger line at each trigger stage. The trigger system consists of the following selection stages, so called *levels*:

- *Level-0 Trigger (L0)* is a hardware based system designed to filter events down to the rate of approximately 1 MHz with the aim to select events that indicate signatures of high transverse energy E_T or high transverse momentum p_T particles. Given that the speed of the decision is a priority, the L0 trigger uses only information from sub-detectors with the shortest response time - The Calorimeters and Muon system.

- *High Level Trigger 1 (HLT1)* is a *C++* software based system operating on a dedicated computer farm designed to reduce the rate of events further down to ~30 kHz. It takes decisions based on partial event reconstruction using information from the tracking system in addition to the Calorimeters and Muon system. To be specific, it searches for presence of tracks with good quality of reconstruction, high momentum or high impact parameter (see 5.3.2) values.
- *High Level Trigger 2 (HLT2)* is also a software based system. It evaluates further all information from the complete detector with the full event reconstruction. Events passing any of the analysis specific trigger lines are recorded for further processing at the rate of ~12.5 kHz (years of data-taking 2015-2018).

3.2.5 Event reconstruction

The full event reconstruction is performed as a sequence of steps as follows:

- *Brunel* software is applied on the output from the electronic read-out system of all sub-detectors to identify *hits* in the detector from which particle *tracks* are extrapolated and combined with information from particle identification algorithms.
- *Moore* software operates high level triggers and assigns *Trigger Configuration Key* to every event specifying the used trigger configuration during the data taking.
- *DaVinci* software applies centrally processed skimming and trimming for all physics analysis working groups, so called *stripping* [32]. This means that final state particles are subjects to requirements based on the specific analysis needs encoded in *stripping lines* specific to the studied decay channels and is a part of *a stripping campaign* which corresponds to the processing of the data from a certain period of data taking, for example 2016 data sample. Generally, stripping lines apply selection criteria on final state particles, which are subsequently used to reconstruct the full decay topology. Reconstructed intermediate particles in the decay chain may be also subject to additional selection requirements.

3.2.6 Monte-Carlo simulation

In order to validate experimental techniques and methods, *Monte Carlo (MC)* simulation is essential. MC simulation samples are produced centrally using the GAUSS software framework [33]. Production involves the following steps:

- PYTHIA generator [34] is used to generate *pp* collisions and consequent hadronisation.
- EVTGEN framework [35] simulates decays of hadrons.

- PHOTOS package [36] adds the final-state radiation.
- GEANT4 platform [37] provides simulation of interactions of generated particles with the detector materials.
- BOOLE program imitates the response of electronics in the detector after an interaction with a particle.
- Full event reconstruction is applied as described in Section 3.2.5.

TruthMatched events

A simulated event is called *TruthMatched* if tracks in the event are matched with the generator-level information corresponding to the particle which created them in the simulation.

3.2.7 Datasets recorded by the LHCb detector

Particle collisions recorded by the LHCb detector are organised into datasets based on the year of their collection. In the beginning of operations in 2010 collisions were produced at an energy of 3.5 TeV per beam, later the energy increased to 4.0 TeV per beam in 2012 and finally to 6.5 TeV per beam from 2015 onwards. Yearly datasets also differ in recorded integrated luminosity including corresponding final values. Fig. 3.14 provides an overview of integrated recorded luminosity in the different years of data taking. Years 2011 and 2012 are collectively referred to as *Run 1* and years 2015-2018 (after a two-year-long LHC shutdown period, *LS1*) are collectively referred to as *Run 2*.

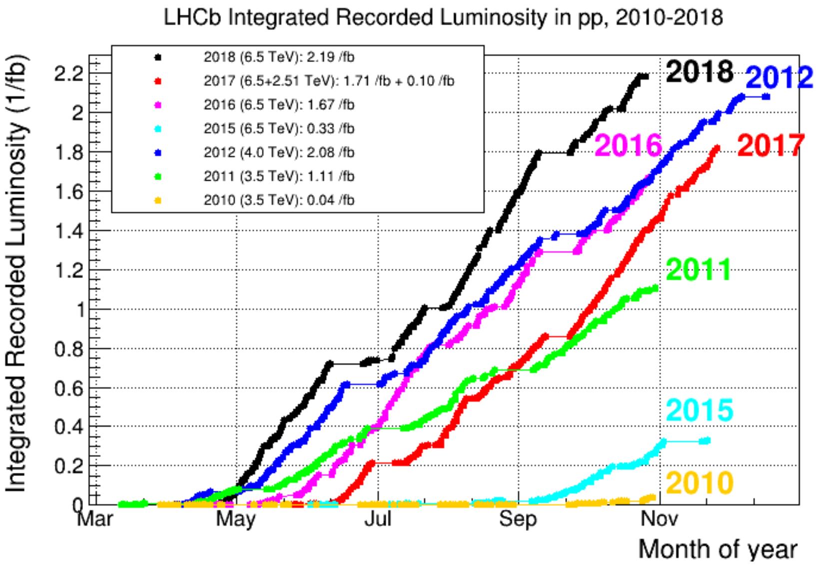

Figure 3.14 – Overview of integrated recorded luminosity over months in the different years of data taking. Figure taken from Ref. [38].

3.3 LHCb upgrade, Phase I

The LHCb experiment has already proven that measurements of excellent quality can be made in the heavy-flavour sector delivering results based on data collected during the LHC Run 1 [39], and even more results are expected from the LHC Run 2 data. However, with the ongoing upgrade of the LHC machine scheduled for the Long Shutdown II which started in 2019, the LHCb detector is also under a major upgrade programme [40].

The upgraded LHCb detector [40] aims at collecting data for an integrated luminosity of at least 50 fb^{-1} in 10 years of operation (approximately 10-times more than so far collected by the current detector), and therefore improve precision and broaden the physics programme of the experiment. To achieve this goal, the major innovations, such as 40 MHz read-out based on software event selection [41], new sub-detectors and front-end electronics for operation at 40 MHz, are deployed. The tracking systems will consist of the upgrade [42] of the current VELO detector, installation of the *Upstream Tracker* (UT) [43] as an upgrade to the TT [44] and replacement of three tracking stations T1–T3 made of the IT [45] and the OT [46] by a new sub-detector, the *Scintillating Fibre (SciFi)* tracker [43]. Start of the data-taking is is expected in 2022 as scheduled in the LHC long-term plan shown in Fig. 3.15.

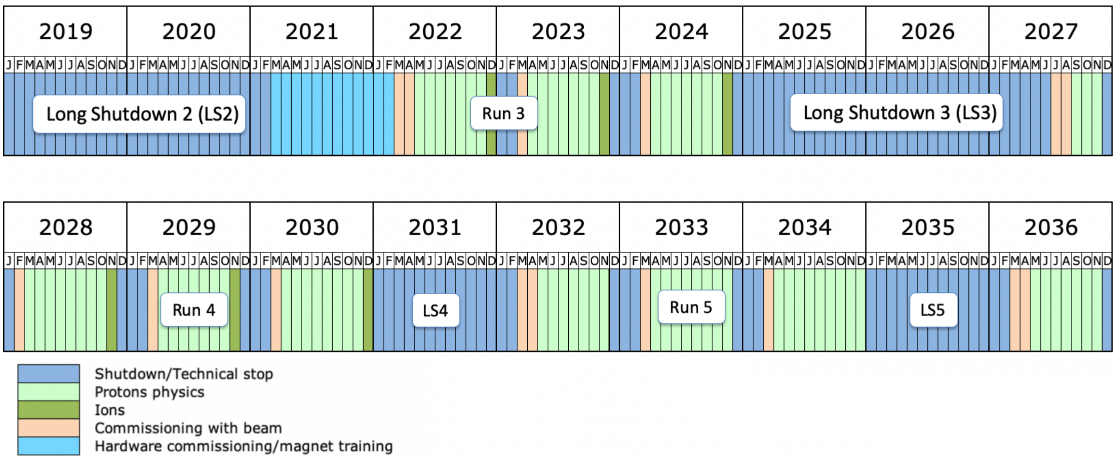

Figure 3.15 – Longer term LHC schedule. Figure taken from Ref. [47].

4 SciFi tracker fibre mat production for the LHCb upgrade

This chapter provides a short overview of the SciFi tracker and the production of thin mattresses made of layers of scintillating fibres, called *fibre mat*, needed for the LHCb upgrade.

4.1 SciFi tracker

The SciFi tracker [43, 48], shown in Fig. 4.1, is a single tracking detector covering an active detection area of 340 m^2. It is designed to have a high track hit efficiency of ~98% and a hit resolution of better than 100μm, to operate at 40 MHz readout frequency with sufficient radiation hardness for the LHC environment. The SciFi tracker is composed of three tracking stations and each of them consists of four detection layers. Its operation principle is based on charged tracks producing scintillation light in 2.42 m long scintillating fibres with a diameter of 250 μm and read out by silicon photo-multipliers (SiPM).

4.2 The production of the SciFi tracker fibre mats

The production of the SciFi tracker consists of several steps: firstly, ~10000 km of commercially produced scintillating circular fibre is delivered to the *Fibre quality centre* (at CERN) for a quality control of the fibres. After documenting all imperfections, the fibre is distributed to the *Fibre winding centres*[I] where it is arranged into six fibre-layer arrays forming a *fibre mat*, shown in Fig. 4.2. The fibre mats are transported to *Module production centres*[II] where they are assembled into modules composed of eight fibre mats each. The modules are then shipped to CERN and each one equipped with a silicon-photomultiplier read-out system and front-end electronics in the final step, during which 12 detection planes are assembled using 128 produced modules [48].

A stable fibre mat production procedure consists of multiple steps: The first step of the scintillating fibre mat production is so called *winding*, during which the scintillating fibre wound around a metallic wheel until a layer is finished; then a layer of glue is applied and

[I] Rheinisch-Westfälische Technische Hochschule Aachen , Technische Universität Dortmund, National Research Centre Kurchatov Institute Moscow and École Polytechnique Fédérale de Lausanne (EPFL).

[II] Ruprecht-Karls-Universität Heidelberg and Nationaal instituut voor subatomaire fysica (Nikhef).

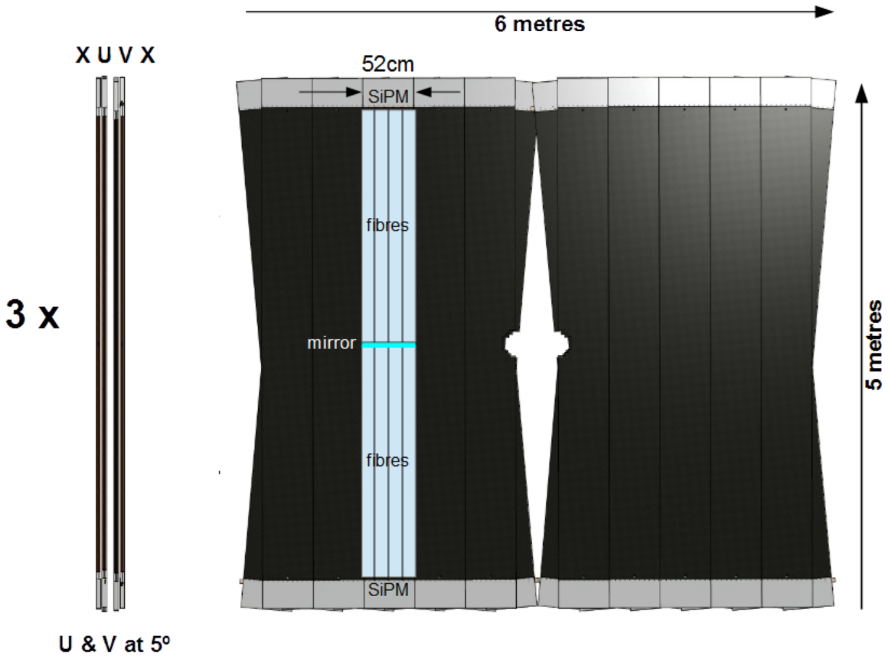

Figure 4.1 – A sketch of 1 station of the SciFi tracker. Each station will have 4 layers (X, U, V, X) oriented at 0, +5, -5 and 0 degrees with respect to the vertical. Each layer will have 10-12 modules depending on the acceptance required and can open away from the beam-pipe at the centre. Each module will have 2.5 m long fibre mats, mirrored at the end nearest the centre, and read out with SiPMs at the far end outside of the acceptance [48].

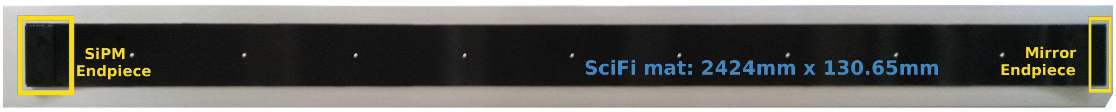

Figure 4.2 – A photograph of the top view of fibre mattress for SciFi tracker (black) on the metallic plate with end-pieces highlighted by yellow rectangles.

a new fibre layer is wound. This process is repeated until six layers of fibres and glue are wound. Thereupon, the wheel is placed into a tent with controlled temperature and humidity conditions, for so called *curing*, where the glue dries. To protect the fibres from mechanical damage and to avoid light exposure, a black plastic foil is laminated on the fibres while on the winding wheel. Once the glue is dry, the fibres on the wheel are cut using a hot wire cutter and *unformed* from the wheel to become a fibre mat which is then placed into the *tempering* setup (plates with regulated temperature) to reduce the mechanical bending. The plastic foil is laminated on the second side of the fibre mat in the next step. This is followed by gluing of plastic end-pieces to the fibre mat ends. Next, the *optical cut* is performed, which means that a fibre mat is placed into a jig and the end-piece with fibres is cut to have desired geometry and surface quality, and finally, a mirror is glued on the mirror-side end-piece.

To ensure that each produced fibre mat meets the design requirements, quality assurance

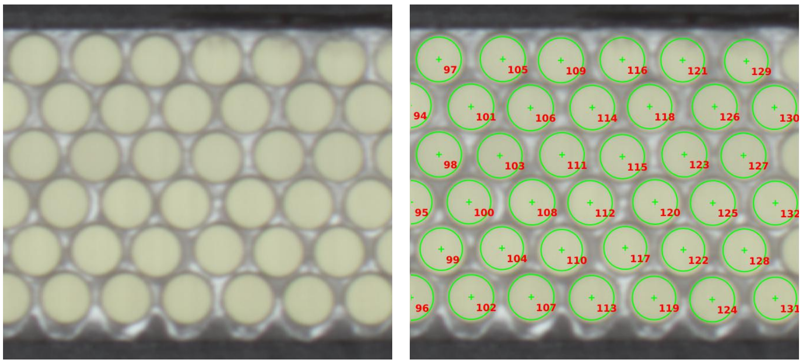

(a) (b)

Figure 4.3 – Section of an optical scan image before (a) and after (b) software fibre identification.

measurements are performed. The first measurement is called *optical scan*, during which one fibre mat end-piece with fibres is placed in front of a commercial high-resolution scanner and the other side end-piece is in contact with a white LED light source. Once the surface of the end-piece is scanned, a dedicated software is used to identify fibres from the image as illustrated in Fig. 4.3.

The main purpose of the optical scan is to identify all the imperfections related to the fibres such as fibre dislocations, fibre mat cracks, dark fibres and, more importantly, to measure all the positions of the fibres to document cases where fibres are outside of detection limits of the SiPM read-out system. The optical scan is carried out for both the SiPM and the mirror end-piece.

Precision holes are made on the plastic end-piece for the SiPM side and used to align the position of the SiPMs. Therefore, the positions of those holes must be measured accurately in order to ensure that the SiPM fully captures the light produced by the fibres. The positions of the holes are measured from the optical scan image by fitting the observed edge of the hole to a circle, where the centre of the circle gives the position of the hole. It was noticed that the edge of the hole in the image was often not sharply defined, leading to increased uncertainties for the measured positions of the holes. Fig. 4.4a demonstrates the fuzziness of the edge. In order to define the circular edges better, a precision pin with different colour is temporarily inserted into the hole. As seen from Fig. 4.4b, those pins provide clear circular edges with a brighter colour, which are used in the fit of a circle. It should be noted that the small hole is produced on the pin, which is used to insert and extract the pin into the hole, appearing as a dark circle in Fig. 4.4b in the middle of the pin. Many checks were made in order to ensure that this procedure would not introduce any systematic effect in the measurement.

Another quality assurance measurement is the *light yield test* where the fibre mat is placed into a dark box and a SiPM read-out system is positioned close to the SiPM end-piece and the fibre mat is exposed to radiation from a ^{90}Sr source in order to measure its response. The number

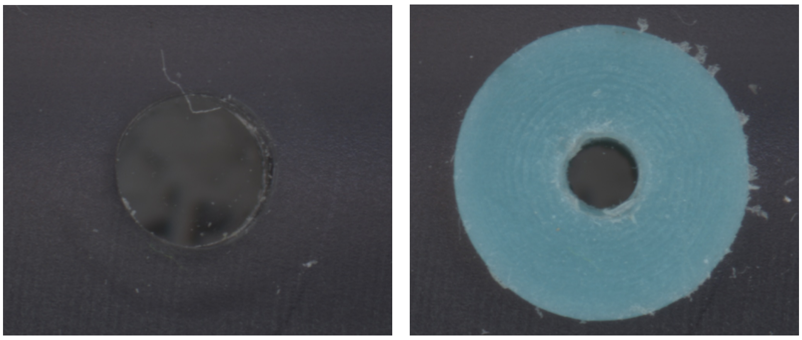

(a) (b)

Figure 4.4 – Comparison of a scan of the empty SiPM-support hole (a) and one with a plastic cylinder-hat shaped pin (b).

of photons reaching the SiPM is counted for each detection channel and the distributions are recorded. This measurement is performed before and after the mirror gluing.

The light yield test is followed by the final geometry measurement and classification of each fibre mat based on its mechanical properties and performance in the optical scan and the light yield test. Finally, a comprehensive online documentation is prepared for all produced fibre mats and they are shipped to the module centres. The timeline of the fibre mat production at EPFL, shown in Fig. 4.5, was well in agreement with the production plan finishing by the end of April 2018.

The collected data can be used to observe possible changes and trends in production quality.

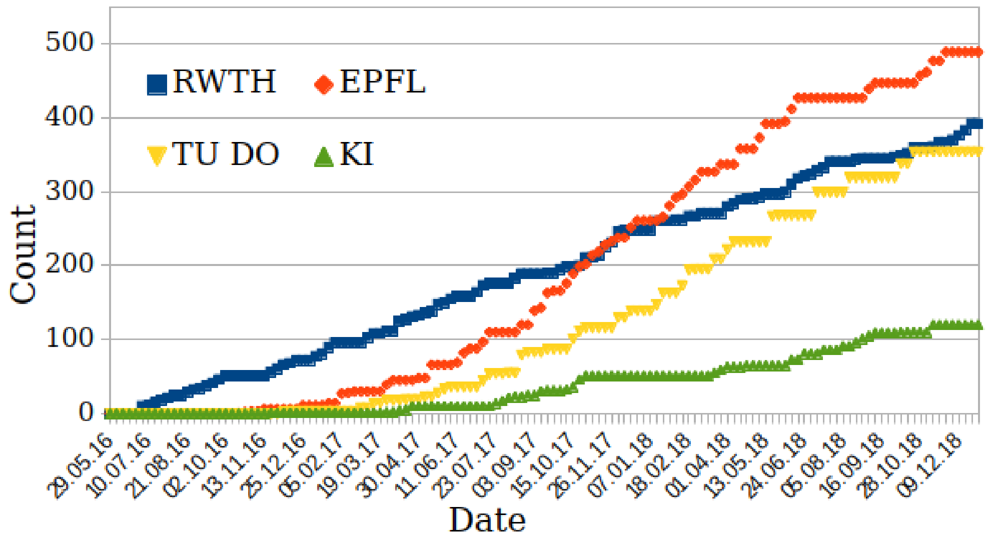

Figure 4.5 – Time evolution of cumulative count of finalised fibre mats at the production sites.

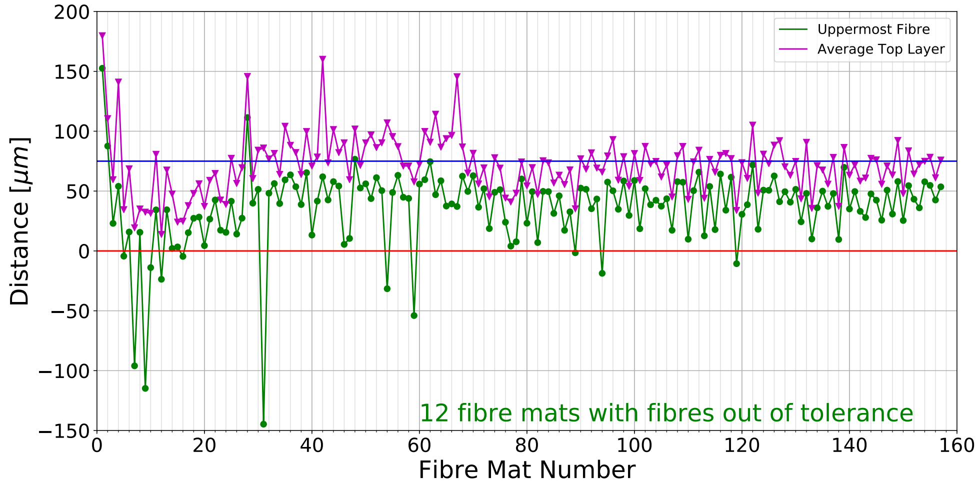

Figure 4.6 – Distance between the SiPM tolerance upper limit (red line) and the centre of the uppermost fibre (green) and average position calculated from the fibre centres in the uppermost layer (magenta) compared to the nominal distance (blue). Negative distance indicates that a fibre is outside of the SiPM tolerance limit which means that not all of delivered photons will be detected.

For example, Fig. 4.6 shows the dependence of the distance between uppermost fibre centre and the upper SiPM read-out limit as a function of fibre mat number. The data indicates no significant trend, but fluctuations from the mean are decreasing with increasing fibre mat numbers. This demonstrates that the production procedure became more stable with time.

Personal Contribution

EPFL production site delivered more then 35% of the total number of produced fibre mats for the LHCb SciFi tracker as indicated in Fig. 4.5. To be specific, 489 fibre mats are finalised out of more than 500 fibre mats that have been produced at EPFL (some produced mats are not finalised because they suffer from defects). During the 1.5 years of production I took the responsibility of quality assurance. This implies performing the optical scans before and after mirror gluing and rating the quality of the mat and collaborating with the technicians with various production steps such as geometrical measurements. I have also improved the reliability and performance of the setup by introducing the plastic pins for better measurement for the centres of the SiPM mounting holes. My other responsibility was to document all the operations performed on the fibre mats into the comprehensive online database to make this information available for the module production centres. Also, I used fibre-mat data collected from the performed optical scans to study possible trends and effects of changes in the fibre mat productions, such as the one described above.

5 Measurement techniques for the search of $\Lambda_b^0 \to \Lambda p\overline{p}$

This chapter presents the developed measurement techniques and studies performed for the first experimental search for purely baryonic decays involving only baryons in the decay channel $\Lambda_b^0 \to \Lambda p\overline{p}$. It is based on a physics analysis performed using the experimental data collected by the LHCb detector during years of data-taking 2015–2018. Firstly, the overall goals and the analysis strategy are presented. Secondly, a description of the data samples is provided. This is followed by details of the event selection tailored for this search. As not all events passing this selection originate from the studied channel, a discussion of possible background contributions is presented. On the other hand, it is inevitable that some of the signal events are lost after the selection, therefore, a detailed summary of efficiencies in this search is also included. Finally, the fit model essential for the measurement is introduced and validated.

5.1 Analysis strategy

The analysis strategy is that of a relative branching fraction measurement of the signal channel and a normalisation channel in order to cancel or minimise systematic effects – the uncertainties in the b-quark cross-section, b hadronisation probability and luminosity cancel. Also, by choosing a normalisation channel topologically identical to the signal channel, the differences in the ratios of efficiencies entering the branching fraction (ratio) calculation cancel to a large extent, the differences between signal and normalisation channels being due to small differences in decay kinematics on the bachelor (Λ_b^0-baryon charged decay product) hadron-pair.

In practical terms, the $\Lambda_b^0 \to \Lambda p\overline{p}$ branching fraction is calculated relative to that of the $\Lambda_b^0 \to \Lambda K^+K^-$ normalisation channel, which was first observed by LHCb and has a measured branching fraction of [20]

$$\mathcal{B}(\Lambda_b^0 \to \Lambda K^+K^-) = (15.9 \pm 1.2 \pm 1.2 \pm 2.0) \times 10^{-6} \quad . \tag{5.1}$$

The first quoted uncertainty is statistical, the second is systematical and the last quoted uncertainty is due to the precision with which the normalisation channel branching fraction is known. The $\Lambda_b^0 \to \Lambda p\overline{p}$ branching fraction is obtained from

$$\mathscr{B}(\Lambda_b^0 \to \Lambda p\overline{p}) = \frac{N(\Lambda_b^0 \to \Lambda p\overline{p})}{N(\Lambda_b^0 \to \Lambda K^+K^-)} \cdot \frac{\epsilon_{\Lambda_b^0 \to \Lambda K^+K^-}}{\epsilon_{\Lambda_b^0 \to \Lambda p\overline{p}}} \cdot \mathscr{B}(\Lambda_b^0 \to \Lambda K^+K^-) \quad , \tag{5.2}$$

where $\mathscr{B}$ stands for the branching fraction and ϵ contains the product of all efficiencies for the decay final state particles to be in the LHCb acceptance, for triggering, reconstruction, stripping and final selection (charge conjugation is implicit throughout this document). The Λ baryon is reconstructed in its dominant decay mode $\Lambda \to p\pi^-$.

5.1.1 Primary signal channel $\Lambda_b^0 \to \Lambda p\overline{p}$

Fig. 5.1 illustrates the full decay topology of the signal channel: a Λ_b^0-baryon is produced from the collision at the point reconstructed as *primary vertex* (PV) and it travels typically ≈0.5 cm of distance before it decays. The Λ_b^0 decay leads to the creation of a Λ-baryon and a $p\overline{p}$ pair. As Λ-baryon is a neutral particle, only tracks from $p\overline{p}$ pair are used to locate the point of Λ_b^0 decay, so called *secondary vertex*. Nevertheless, Λ-baryon properties can be reconstructed after its decay to a proton-pion pair after travelling up to 2 m in the detector. Depending on the location where the Λ-baryon decays, final state particles create different types of tracks as discussed in Section 3.2.1. This implies that the data analysis is split not only per year but also according to the track type of the reconstructed daughters of the long-lived Λ baryon: Long-Long (LL) and Downstream-Downstream (DD) subsamples are defined, respectively, when both Λ daughters have tracks present in the VELO or neither daughter produces tracks in the VELO. As the normalisation channel $\Lambda_b^0 \to \Lambda K^+K^-$ is nearly identical to the signal channel $\Lambda_b^0 \to \Lambda p\overline{p}$- a K^+K^- pair is present instead of the $p\overline{p}$ pair - the same set of event selection steps is applied on both samples as discussed in Section 5.3.

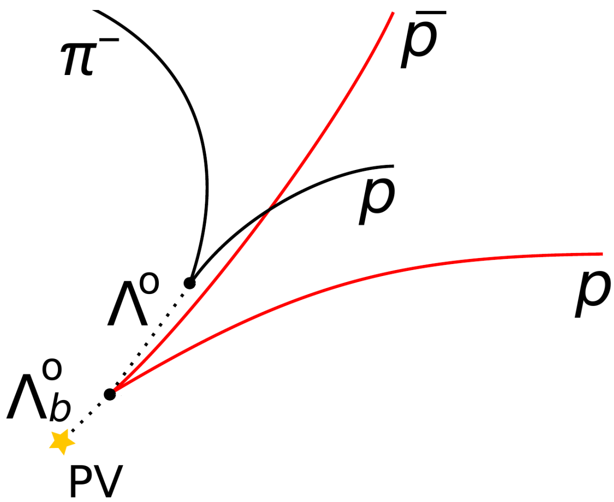

Figure 5.1 – Decay topology of the signal $\Lambda_b^0 \to \Lambda p\overline{p}$ channel.

5.1.2 Secondary signal channel $\Xi_b^0 \rightarrow \Lambda p\overline{p}$

Analysis of potential contribution from the $\Xi_b^0 \rightarrow \Lambda p\overline{p}$ decay channel is performed. This is motivated by the fact that it has the same final state as the principal signal channel $\Lambda_b^0 \rightarrow \Lambda p\overline{p}$ and the reconstructed invariant mass of the $\Lambda p\overline{p}$-system is higher only by ≈174.9 MeV [6]. However, following the theoretical predictions stated in Section 2.2 it is not expected to be observed.

5.1.3 Blind analysis

In order to assure that there is no bias in the final results the methods of *blind analysis* are deployed. This means that once the blind regions are defined at the very beginning of the data analysis their content is excluded and inaccessible until all the methods used are finalised and validated.

Blind regions in this analysis are defined as intervals of the reconstructed invariant mass of the $\Lambda p\overline{p}$ system. To be specific, they are chosen to cover the range of ±50 MeV around the nominal Λ_b^0-baryon and Ξ_b^0-baryon masses. Resulting blind intervals are[I]:

$$m(\Lambda p\overline{p}) \in [5569, 5669]\,\text{MeV}$$

$$m(\Lambda p\overline{p}) \in [5738, 5838]\,\text{MeV}$$

In this work, samples from normalisation channel, MC simulations and the upper and the lower intervals of invariant mass of $(\Lambda p\overline{p})$-system, so called *side-bands*, are used to develop and validate all the methods used.

5.1.4 Measurement outline

Firstly, the event selection is used to identify the decay candidates relevant for this analysis in the data samples recorded by the LHCb detector. Then they are subject to a statistical analysis deploying a maximum likelihood fit performed simultaneously in the normalisation and signal channels. The statistical significance of the examined channels is then evaluated, and the branching fractions and the invariant masses of two-body sub-systems are studied.

5.2 Event samples

5.2.1 Data

The dataset analysed amounts to the full Run 2 sample 2015–2018. Two stripping lines (see

[I]Natural units $\hbar = c = 1$ are used

Table 5.1 – The integrated luminosities corresponding to the used samples.

Year	$\mathscr{L}_{\mathrm{int}}$ [fb^{-1}]
2015	0.29
2016	1.66
2017	1.63
2018	2.08
Total	5.66±0.11

Section 3.2.5) are used: `Lb2V0hh` for the decay mode $\Lambda_b^0 \to \Lambda K^+ K^-$ and `Lb2V0pp` for the $\Lambda_b^0 \to \Lambda p\overline{p}$ mode hypothesis. These stripping lines are discussed in detail in Section 5.3.2.

The integrated luminosities corresponding to the used samples are summarised in Table 5.1.

5.2.2 Monte Carlo simulation

Several Run 2 Monte Carlo (MC) samples are used to assess efficiencies and acceptances, and to study background contributions. Table 5.2 lists the used MC samples. Each sample contains approximately the same number of events per magnet polarity and twice or thrice as many events reconstructed with each of 2016, 2017, and 2018 conditions than with 2015 conditions.

Generators of the MC simulation can be configured to produce samples such that the distributions of events are constant in certain variables. For example, it is possible to choose uniform generation in so called *Dalitz variables.* They are commonly used to describe the three-body decay phase-space. Generally, there are three possible combinations of two-body subsystems. Two of these three combinations are sufficient to fully describe the studied decay. Dalitz variables are invariant masses squared of the two selected two-body subsystems [49]. However, they are not always practical in the study of heavy hadron decays to light final state particles. This is because regions approaching the kinematic boundaries of the Dalitz variables are most populated by both signal and background events [50]. Therefore, another, more convenient choice of variables is preferred in this analysis. To be specific, all the used MC samples are generated uniformly across the phase-space defined by the so-called *Square Dalitz variables.* These are defined analogically to the definitions previously published in Ref. [50], explicitly for the normalisation mode (definitions for the signal mode $\Lambda_b^0 \to \Lambda p\overline{p}$ are trivially adapted):

$$m'_{K^+K^-} \equiv \frac{1}{\pi} \arccos\left[\frac{2(m_{K^+K^-} - 2m_K)}{m_{\Lambda_b^0} - m_\Lambda - 2m_K} - 1\right], \tag{5.3}$$

$$\theta'_{K^+K^-} \equiv \frac{1}{\pi}(\theta_{K^+K^-}), \tag{5.4}$$

Table 5.2 – Run-2 MC samples used notably for efficiencies determination and background studies. Number of events is a total of events in all samples available (certain samples are not simulated for all years of data-taking following the early studies indicating that the contribution in the corresponding decay channel is not expected).

Decay channel	Number of events	Years
$\Lambda_b^0 \to \Lambda p\overline{p}$	17438087	15-18
$\Lambda_b^0 \to \Lambda K^+ K^-$	17027392	15-18
$\Lambda_b^0 \to \Lambda K^+ \pi^-$	9061774	15-18
$\Lambda_b^0 \to \Lambda \pi^+ \pi^-$	9079868	15-18
$B^0 \to K_S^0 K^+ K^-$	6013840	15-17
$B_s^0 \to K_S^0 p\overline{p}$	6030791	15-17
$B_s^0 \to K_S^0 K^\pm \pi^\mp$	6034988	15-17
$\Lambda_b^0 \to K_S^0 p \pi^-$	4016321	16

$$\theta_{K^+K^-} \equiv \arccos\left(-\frac{{}^{MAX}m^2_{\Lambda K^-} + {}^{MIN}m^2_{\Lambda K^-} - 2m^2_{\Lambda K^-}}{{}^{MAX}m^2_{\Lambda K^-} - {}^{MIN}m^2_{\Lambda K^-}}\right), \tag{5.5}$$

where the superscripts *MIN* and *MAX* indicate minimal and maximal kinematically allowed values for a given two-body subsystem. Note that these variables are implicitly dependent on the invariant mass of the two-body K^+K^- system, $m_{K^+K^-}$.

Both variables $m'_{K^+K^-}$ and $\theta'_{K^+K^-}$ have validity ranges between 0 and 1 taking into account the kinematic boundaries of the considered decay. The variable $m'_{K^+K^-}$ represents the normalised invariant mass of the two-body K^+K^- subsystem and $\theta_{K^+K^-}$ is the helicity angle of the K^+K^- subsystem (the angle between the Λ and the K^+ meson in the K^+K^- rest-frame). The main advantage of Square Dalitz variables is embedded in their defining transformation which deforms the plane of original Dalitz variables in a way that most populated regions are extended and hence preferentially generated in simulation.

5.3 Event selection

The event selection used in this analysis is a sequence of selection requirements described in the following subsections applied on the data samples discussed in Section 5.2.

5.3.1 Trigger

For every candidate passing the trigger selection, each trigger line indicates to which of the following *trigger decision categories* [51] candidate event belongs:

Table 5.3 – List of trigger lines with required categories used to select the signal candidates.

Trigger level	Requirements	Description
L0	`L0Hadron_TOS` or `L0Global_TIS`	A hadron from signal detected or triggered independently of signal
HLT1	`Hlt1TrackMVADecision_TOS` or `Hlt1TwoTrackMVADecision_TOS`	1-or-2 good quality tracks interest reconstructed based on the decision of a MVA classifier
HLT2	`Hlt2Topo2BodyBBDT_TOS` or `Hlt2Topo3BodyBBDT_TOS`	2-or-3-body decay of interest reconstructed based on the decision of a boosted decision tree classifier

- *Triggered On Signal (TOS)*: The presence of the signal is sufficient to generate a positive trigger decision for the event.
- *Triggered Independent of Signal (TIS)*: A positive trigger decision for the event is generated even after applying an operational procedure consisting in removing the signal and all detector hits belonging to it.
- *Triggered On Both (TOB)*: Events that are neither TIS nor TOS; neither the presence of the signal alone nor the rest of the event alone are sufficient to generate a positive trigger decision, but rather both are necessary.

The trigger selection represents a set of requirements on trigger lines of choice required for a trigger positive decision. Table 5.3 lists the trigger lines (see Section 3.2.4) with required categories used to select the $\Lambda_b^0 \to \Lambda p\overline{p}$ signal and the $\Lambda_b^0 \to \Lambda K^+K^-$ normalisation candidates. These lines are standard lines for hadronic b-hadron decays. The choice follows the results of a study of the contribution of each trigger line to the overall selection efficiency.

5.3.2 Stripping selection

The events passing the trigger selection are then subject to the stripping selection offline, after storage for subsequent analysis. The data samples are split into the `Long` (`LL`) and `Downstream` (`DD`) track samples via the dedicated lines. For each event, each stripping line first applies a global requirement on the number of `Long` tracks in the event, $N_{\text{Long}} < 250$, and requires that the tracks used in the signal decays have χ^2_{track}<3 (χ^2_{track} corresponds to the quality of the fit of the particle trajectory reconstructed from the detector hits) and *GhostProbability*<0.5 (probability that the reconstructed track does not correspond to a real particle but it is a random set of hits in the detector). The lines then apply the complete decay reconstruction and selection requirements. Generally, this corresponds to: Λ reconstruction and selection, reconstruction of a final state hadron (a proton in case of the $\Lambda_b^0 \to \Lambda p\overline{p}$ mode and a kaon in case of $\Lambda_b^0 \to \Lambda K^+K^-$) called *bachelor reconstruction*, requirements for combining the Λ with the bachelors and, finally, requirements on the reconstructed Λ_b^0 candidate.

This analysis exploits two sets of stripping lines:

- `StrippingLb2V0hhLLLine and StrippingLb2V0hhDDLine` for the candidates in the normalisation mode $\Lambda_b^0 \to \Lambda K^+ K^-$. These lines were used in the previous analysis of this mode [20].

- `StrippingLb2V0ppLLLine and StrippingLb2V0ppDDLine` for the candidates in the signal mode $\Lambda_b^0 \to \Lambda p\overline{p}$. These lines are designed based on StrippingLb2V0hhLLLine and StrippingLb2V0hhDDLine. However, the selections are optimized for the observation of the searched signal mode following the simulation-based studies[II].

Λ and bachelor candidates reconstruction

All used stripping lines apply the same Λ reconstruction procedure. Firstly, the Λ candidates are taken from `StdLooseLambdaLL` and `StdLooseLambdaDD` *containers* (lists of particles fulfilling the reconstruction requirements applied on the tracks). The Λ candidates are reconstructed from p and π^- tracks drawn from the corresponding containers indicated in Table 5.4. Common requirements and requirements specific to the given stripping line are indicated in Table 5.5. The `StdLooseLambdaDD` container has no particle identification requirements whereas the protons forming the `Long` track Λ candidates (from the `StdLooseLambdaLL` container) are required to satisfy the loose cut $DLL(p-\pi^+) > -5.0$ (difference in logarithms of likelihoods of particle being a proton or a pion as determined by the RICH detectors), which is identical for both the normalisation and signal modes.

[II] No particle-identification information is used at this stage (see Section 5.3.4)

Table 5.4 – Particle containers for the Λ reconstruction including (direct or inherited from more global containers) selection criteria on candidates in corresponding containers.

	p candidate	π^- candidate
	`StdLooseLambdaLL`	
	`StdLooseProtons`	`StdLoosePions`
Transverse momentum	$p_{\mathrm{T}} > 250\,\mathrm{MeV}$	$p_{\mathrm{T}} > 250\,\mathrm{MeV}$
χ^2 distance of trajectory to PV	$\chi^2(\mathrm{IP}) > 4$	$\chi^2(\mathrm{IP}) > 4$
Hypothesis consistent signature	calorimeters	calorimeters
Signature required in sub-detectors	RICH	-
Difference in log. likelihood	$\mathrm{DLL}(p-\pi^+) > -5.0$	-
	`StdLooseLambdaDD`	
	`StdNoPIDsDownProtons`	`StdNoPIDsDownPions`
No cuts applied	-	-

Table 5.5 – Selection requirements for the Λ candidates.

Variable Definition	Selection Requirement
`StdLooseLambdaLL`	
Mass difference wrt nominal Λ mass	$\lvert m_{p\pi} - m_{\Lambda}\rvert < 35$ MeV
χ^2 of Λ vertex fit	$\chi^2_{\Lambda\,\mathrm{vtx}} < 30$
Λ daughter track momentum	$p_{\Lambda\,\mathrm{daug}} > 2\,\mathrm{GeV}/c$
Λ daughter minimum impact parameter χ^2 wrt PVs	$\chi^2(\mathrm{IP})_{\mathrm{min}} > 9$
Maximum distance of the closest approach χ^2 of Λ daughters	$\chi^2(\mathrm{DOCA})_{\mathrm{max}} < 25$
Extra requirements on LL Λ candidates from Lb2V0hh line	
Mass difference wrt nominal Λ mass	$\lvert m_{p\pi} - m_{\Lambda}\rvert < 20$ MeV
χ^2 of Λ vertex fit	$\chi^2_{\Lambda\,\mathrm{vtx}} < 15$
χ^2 separation of Λ vertex and associated PV	$\chi^2_{\Lambda-\mathrm{PVVD}} > 80$
Extra requirements on LL Λ candidates from Lb2V0pp line	
Mass difference wrt nominal Λ mass	$\lvert m_{p\pi} - m_{\Lambda}\rvert < 20$ MeV
χ^2 of Λ vertex fit	$\chi^2_{\Lambda\,\mathrm{vtx}} < 9$
χ^2 separation of Λ vertex and associated PV	$\chi^2_{\Lambda-\mathrm{PVVD}} > 0$
Maximum distance of the closest approach χ^2 of Λ daughters	$\chi^2(\mathrm{DOCA})_{\mathrm{max}} < 30$
`StdLooseLambdaDD`	
Mass difference wrt nominal Λ mass	$\lvert m_{p\pi} - m_{\Lambda}\rvert < 64$ MeV
χ^2 of Λ vertex fit	$\chi^2_{\Lambda\,\mathrm{vtx}} < 25$
Λ daughter track momentum	$p_{\Lambda\,\mathrm{daug}} > 2\,\mathrm{GeV}/c$
Λ daughter minimum impact parameter χ^2 wrt PVs	$\chi^2(\mathrm{IP})_{\mathrm{min}} > 4$
Extra requirements on DD Λ candidates from Lb2V0hh line	
Mass difference wrt nominal Λ mass	$\lvert m_{p\pi} - m_{\Lambda}\rvert < 25$ MeV
χ^2 of Λ vertex fit	$\chi^2_{\Lambda\mathrm{vtx}} < 15$
χ^2 separation of Λ vertex and associated PV	$\chi^2_{\Lambda-\mathrm{PVVD}} > 50$
Λ flight distance from primary vertex	$\Lambda_{FD} > 300\,\mathrm{mm}$
Λ momentum	$p_{\Lambda} > 5\,\mathrm{GeV}/c$
Extra requirements on DD Λ candidates from Lb2V0pp line	
Mass difference wrt nominal Λ mass	$\lvert m_{p\pi} - m_{\Lambda}\rvert < 20$ MeV
χ^2 of Λ vertex fit	$\chi^2_{\Lambda\mathrm{vtx}} < 9$
χ^2 separation of Λ vertex and associated PV	$\chi^2_{\Lambda-\mathrm{PVVD}} > 50$
Λ flight distance from primary vertex	$\Lambda_{FD} > 300\,\mathrm{mm}$
Λ momentum	$p_{\Lambda} > 5\,\mathrm{GeV}/c$

Table 5.6 – Selection requirements for combining Λ with bachelors into a Λ_b^0 decay candidate.

Variable Definition	Selection Requirement
Combination Cuts `Lb2V0hh` lines:	
IP wrt PV of highest p_T of Λ_b^0 daughter	IP > 0.05 mm
p_T of at least 2 Λ_b^0 daughters	$p_\mathrm{T} > 800$ MeV
Mass of the Λ_b^0 candidate	$4301 < m_{\Lambda hh} < 6220$ MeV
Max. distance of the closest approach χ^2 of any 2 daughters	$\chi^2(\mathrm{DOCA})_{\max} < 5$
Sum of the daughters' transverse momenta (DD)	$\sum_\mathrm{daug} p_\mathrm{T} > 4200$ MeV
Sum of the daughters' transverse momenta (LL)	$\sum_\mathrm{daug} p_\mathrm{T} > 3000$ MeV
Transverse momenta of the sum 4-vector of daughters	$p_\mathrm{T}(\sum_\mathrm{daug} P) > 1000$ MeV
Combination Cuts `Lb2V0pp` lines:	
IP wrt PV of highest p_T of Λ_b^0 daughter	IP > 0.05 mm
p_T of at least 2 Λ_b^0 daughters	$p_\mathrm{T} > 405$ MeV
Mass of the Λ_b^0 candidate	$5201 < m_{\Lambda hh} < 6221$ MeV
Max. distance of the closest approach χ^2 of any 2 daughters (DD)	$\chi^2(\mathrm{DOCA})_{\max} < 16$
Max. distance of the closest approach χ^2 of any 2 daughters (LL)	$\chi^2(\mathrm{DOCA})_{\max} < 5$
Sum of the daughters' transverse momenta (DD)	$\sum_\mathrm{daug} p_\mathrm{T} > 2000$ MeV
Sum of the daughters' transverse momenta (LL)	$\sum_\mathrm{daug} p_\mathrm{T} > 3000$ MeV
Transverse momenta of the sum 4-vector of daughters	$p_\mathrm{T}(\sum_\mathrm{daug} P) > 1000$ MeV

The charged bachelors of the Λ_b^0 candidate, *i.e.* the pairs of charged kaons or protons, are taken from the `StdNoPIDsPions` and `StdLooseProtons` containers, respectively. Both containers construct list of charged particles with transverse momentum $p_\mathrm{T} > 250$ MeV and value of the minimum impact parameter $\chi^2 > 4$.

Λ_b^0 reconstruction and requirements

The Λ candidate is combined with the pair of opposite-charge hadrons to form the Λ_b^0 candidate. The Λ_b^0 candidates are first formed by simple four-momentum addition, before a set of loose *combination cuts*. They take advantage of following variables: transverse momentum p_T, distance of closest approach of the track to the reference vertex (usually the primary vertex) called *impact parameter (IP)*, the difference in reconstruction fit χ^2 between a vertex reconstructed with and without a track that has minimal IP called *minimum impact parameter* χ^2, distance of the closest approach of two particles *DOCA*, and angle between the momentum vector of the particle and the direction of flight from the PV to the decay vertex *Direction angle (DIRA)*.

Combination cuts, listed in Table 5.6, are applied to reduce the number of events that undergo the full vertex fit. Further quality *mother cuts* - a set of selection requirements applied to the vertex-fitted Λ_b^0 candidate listed in Table 5.7 - are applied to the vertex-fitted Λ_b^0 candidate.

Table 5.7 – Selection requirements applied to the vertex-fitted Λ_b^0 candidate.

Mother Cuts Lb2V0hh lines	
Transverse momentum of the Λ_b^0 candidate	$p_{\mathrm{T}} > 800$ MeV
χ^2 of Λ_b^0 vertex fit	$\chi^2_{\Lambda_b^0\,\mathrm{vtx}} < 12$
Cosine of Λ_b^0 pointing angle	$\cos(\mathrm{DIRA}_{\Lambda_b^0}) > 0.995$
Minimum Λ_b^0 IP χ^2 wrt PVs	$\chi^2(\mathrm{IP})_{\mathrm{min}} < 15$
Minimum vertex distance wrt PVs	$\left\lvert \Lambda^0_{b\mathrm{vtx}} - PV \right\rvert_{\mathrm{min}} > 1\,\mathrm{mm}$
χ^2 separation of Λ_b^0 vertex and associated PV	$\chi^2_{\Lambda_b^0-\mathrm{PVVD}} > 30$
Mother Cuts Lb2V0pp lines	
Transverse momentum of the Λ_b^0 candidate	$p_{\mathrm{T}} > 1050$ MeV
χ^2 of Λ_b^0 vertex fit	$\chi^2_{\Lambda_b^0\,\mathrm{vtx}} < 16$
Cosine of Λ_b^0 pointing angle	$\cos(\mathrm{DIRA}_{\Lambda_b^0}) > 0.999$
Minimum Λ_b^0 IP χ^2 wrt PVs	$\chi^2(\mathrm{IP})_{\mathrm{min}} < 25$
Minimum vertex distance wrt PVs	$\left\lvert \Lambda^0_{b\mathrm{vtx}} - PV \right\rvert_{\mathrm{min}} > 0.8\,\mathrm{mm}$
χ^2 separation of Λ_b^0 vertex and associated PV	$\chi^2_{\Lambda_b^0-\mathrm{PVVD}} > 0.5$

5.3.3 Decay tree fitting

The *Decay Tree Fitter* (DTF) algorithm [52] is applied to the candidate decay chains (candidate Λ_b^0 decay followed by the Λ decay) when they are selected. The DTF uses a Kalman filter to refit the decay chain given a mass hypothesis of the daughter particles – K^+K^- or $p\overline{p}$. It constrains the decay products of the Λ_b^0 candidates to originate from a common vertex. Also, the mass of the Λ candidates is constrained to the nominal Λ mass. Its value is taken from Ref. [6] and rounded to 1115.68 MeV. Furthermore, the Λ_b^0 candidate is constrained to originate from the primary vertex (PV). Variables resulting from the constraints imposed by the DTF are stored in parallel with their counterparts without constraints which are also exploited.

5.3.4 Combined MVA-PID event selection

An efficient event selection is essential to suppress combinatorial background (events formed from random track combinations reconstructed in the detector), which contaminates in samples collected with the LHCb detector, and to reduce the amount of background from other b-hadron decays.

The event selection combines a *Multivariate analysis (MVA)*, based on Machine learning (ML) algorithms evaluating topological variables, and *particle identification (PID)* based on ML algorithms operating on detector related variables. In order to maximise the performance, the event selection is designed and optimised to profit from all the available information. It consists of the following steps:

1. *Application of a set of pre-selection requirements.*
2. *The optimisation of a multivariate classification (MVA) variable.*
3. *The definition of a combined particle identification (PID) variable.*
4. *The simultaneous optimisation of the combined MVA and PID selection requirements.*

Pre-selection

Firstly, the distributions of signal and background events are studied in several variables in order to identify which of them exhibit differences between signal and background. Examples of studied variables are: the distribution of the z-coordinates of the Λ_b^0 and Λ decay vertices, p_{T} and η of the Λ_b^0 and Λ, etc. Distributions of selected variables are provided in Fig. 5.2 (DD) and in Fig. 5.3 (LL). The signal distributions are obtained from MC simulation, and the combinatorial background (see Section 5.4) distributions are established from the upper mass side-bands. Lower mass side-bands are generally not considered due to the potential contributions of the partially reconstructed backgrounds which could bias the selection.

Selection requirements on some of the variables are applied directly given clear signal-background difference is observed in the data. Note that pre-selection exploits the variables without DTF constraints (see Section 5.3.3).

Firstly, the studied interval of reconstructed invariant mass of the Λ_b^0 (Ξ_b^0) candidates is restricted to be:

$$m(\Lambda p\overline{p}) \in (5350, 6050)\,\mathrm{MeV}$$

The resulting requirements, applied both signal and normalisation channels, are summarised in Table 5.8. These requirements are motivated as follows:

- The distribution of the z-coordinate of the Λ decay vertex exhibits a peak in the background at the location of the TT sub-detector at $z = 2232$mm in the DD tracks samples. For consistency reasons, this cut is also applied for LL candidates despite having only a marginal effect on them.
- Distribution of the difference in z-coordinates, Δz, of the decay vertices of the Λ and Λ_b^0 exhibits a peak in the background in the region $z_{\Lambda}^{DV} - z_{\Lambda_b^0}^{DV} < 30$ mm with a maximum close to zero distance in the LL sample. This background peak is related to events with incorrectly reconstructed secondary vertices. In fact, decreasing the distance between the primary and secondary vertices leads to experimental difficulties to reliably identify the origin of all tracks involved. For example, a secondary vertex may be falsely reconstructed from the tracks which originated from the primary vertex due to

resolution effects. As the Λ in signal events of the DD sample typically travels longer distances than in case of LL samples, signal events in DD sample are not affected.

- From fitting the Λ mass spectrum of MC simulation *TruthMatched* events (see Section 3.2.6) with a Gaussian distribution we obtain the Gaussian parameters μ=1115.83 MeV and σ=1.608 MeV. In order to reduce background events, the cut $|m_{p\pi^-} - \mu| < 3\sigma$ is introduced.

- At the stripping selection level, an event is accepted if it contains at least one candidate which passes the selection requirements. In order to remove additional candidates that do not satisfy the selection requirements, we require: Minimum Λ_b^0 IP χ^2 with respect to PVs, $\chi^2(\text{IP})_{\text{min}} < 15$.

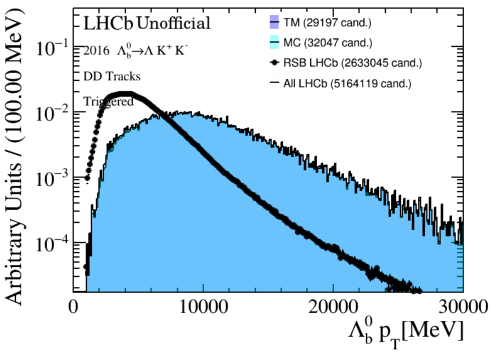

(a) Transverse momentum of Λ_b^0, p_{T}.

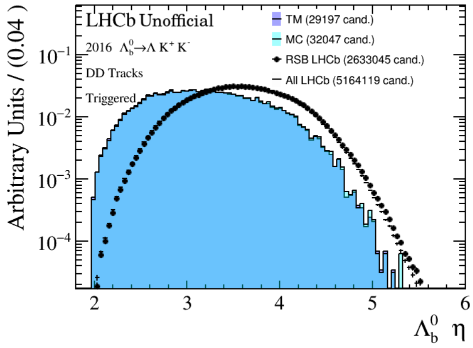

(b) Pseudo-rapidity of Λ_b^0, $\eta_{\Lambda_b^0}$.

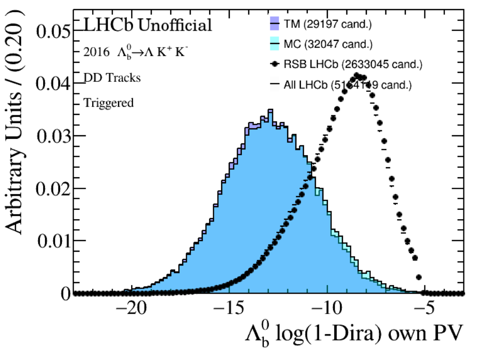

(c) $\log(1 - D_{\Lambda_b^0})$, where $D^{\Lambda_b^0}$ is DIRA of Λ_b^0 with respect to own PV.

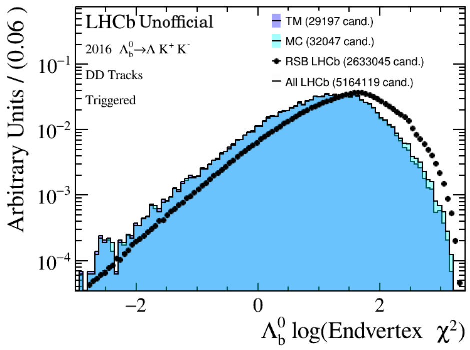

(d) $\log(\chi^2_{\Lambda_b^0}{}^{\text{Endvertex}})$, where $\chi^2_{\Lambda_b^0}{}^{\text{Endvertex}}$ is the χ^2 of the Λ_b^0 decay vertex.

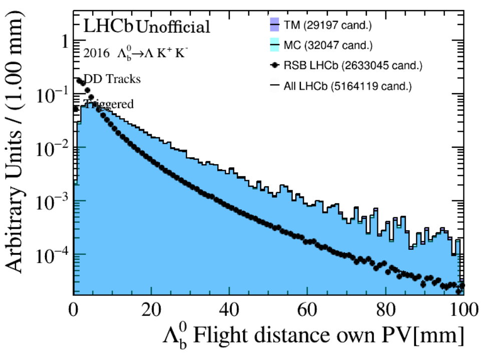

(e) Flight distance of Λ_b^0 with respect to its own PV.

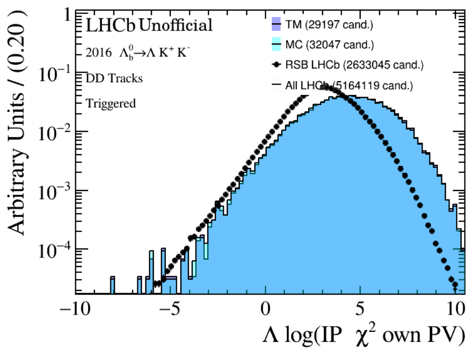

(f) $\log(\chi^2_{\Lambda}{}^{\text{OwnPV}})$, $\chi^2_{\Lambda}{}^{\text{OwnPV}}$ is χ^2 of the decay in which Λ would originate from its own PV (not from Λ_b^0 decay).

Figure 5.2 – Distributions of examples of input variables for *DD track* ML classifier training. The distribution of simulated MC events (blue) is overlapping with MC *TruthMatched* events (light blue). Normalised distribution of upper mass side band events (black dots) overlays with the distribution of all events (black lines).

Table 5.8 – Pre-selection criteria applied to both signal and normalisation decay channels.

Studied interval of reconstructed Λ_b^0 invariant mass	$m \in (5350, 6050)$ MeV
z-coordinates of decay vertex	$z_{\Lambda}^{DV} < 2232$ mm
Δz of the decay vertices of the Λ and Λ_b^0	$z_{\Lambda}^{DV} - z_{\Lambda_b^0}^{DV} > 30$ mm
Reconstructed Λ mass	$\lvert m_{p\pi^-} - 1115.83\,\text{MeV}\rvert < 3 \times 1.608$ MeV
$\Lambda_b^0 IP\chi^2$ with respect to PVs	$\chi^2(\text{IP})_{\text{min}} < 15$

The *TruthMatching* requirement is applied to the signal MC after the pre-selection. Its effect is found to affect MC event distributions only marginally. To be specific it removes ≈ 9% of events passing the trigger selection. While it has little to no impact on distribution shapes, a systematic uncertainty may be assigned given the removed events may have signal-like distribution.

Events which pass the Pre-selection are used in the next selection step (see Section below). As an example, normalised distributions of the invariant mass of $\Lambda K^+ K^-$ system in the normalisation mode are shown in Fig.5.4 for 2016 DD and LL samples.

Multivariate classification (MVA)

The set of simple cuts defined in event pre-selection is based on the constraints of the studied decay. In order to further exploit the underlying differences between signal decays and random track combinations forming the combinatorial background, a classifier training needs to be performed with events in a representation constructed from the physics quantities exhibiting a difference between signal and background. Hence distributions of various physics quantities have been studied after applying the trigger requirements and after applying stripping and the pre-selection. Also various variable transformations, such as taking logarithms, were tested in order to help identifying quantities exhibiting the best performance at separating signal and background. The identified quantities are used as input variables in the next event selection step, the multivariate classification (MVA).

Variables related to properties of particles reconstructed under $\Lambda_b^0 \to \Lambda K^+ K^-$ (or $\Lambda_b^0 \to \Lambda p\bar{p}$) decay hypothesis (particle momentum, decay vertex position, impact parameter, etc.) are used as an input to a Machine Learning (ML) framework. It features a classifier with automatised hyper-parameter optimisation (based on methods from the *Yandex Reproducible Experiment Platform project*) [53] and *k-folding* method [54] with $k = 5$ folds. *DD track* and *LL track* sub-samples are addressed independently, leading to two independent classifiers. The classifiers are trained using *TruthMatched* 2016 MC samples of $\Lambda_b^0 \to \Lambda K^+ K^-$ to model the signal category and the 2016 LHCb events reconstructed under $\Lambda_b^0 \to \Lambda K^+ K^-$ hypothesis falling into the upper-mass side-band $(\Lambda K^+ K^-) \in [5838, 6050]$ MeV (see *RSB LHCb* dotted distributions in

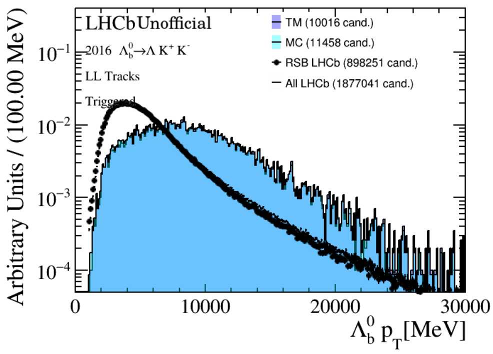

(a) Transverse momentum of Λ_b^0, p_{T}.

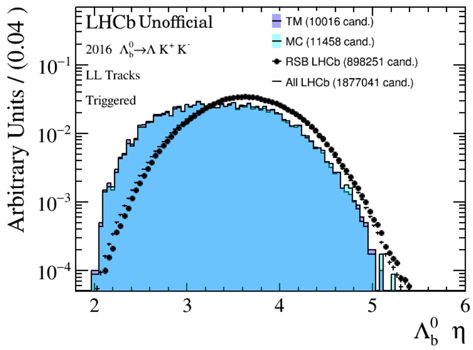

(b) Pseudo-rapidity of Λ_b^0, $\eta_{\Lambda_b^0}$.

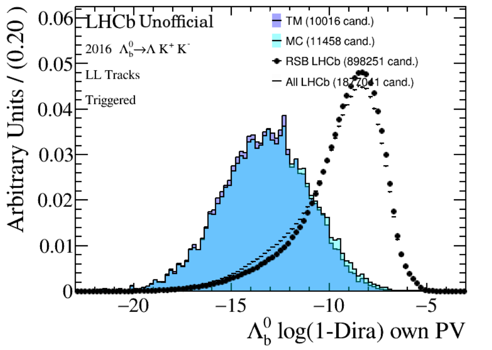

(c) $\log(1 - D_{\Lambda_b^0})$, where $D^{\Lambda_b^0}$ is DIRA of Λ_b^0 with respect to own PV.

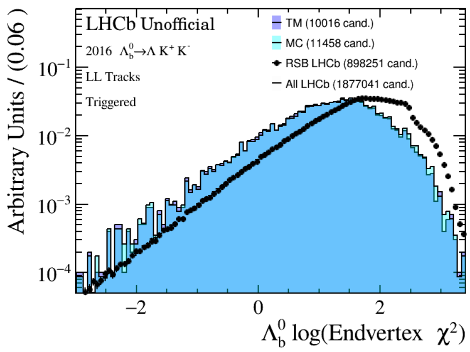

(d) $\log(\chi^{2\ \mathrm{Endvertex}}_{\Lambda_b^0})$, where $\chi^{2\ \mathrm{Endvertex}}_{\Lambda_b^0}$ is the χ^2 of the Λ_b^0 decay vertex.

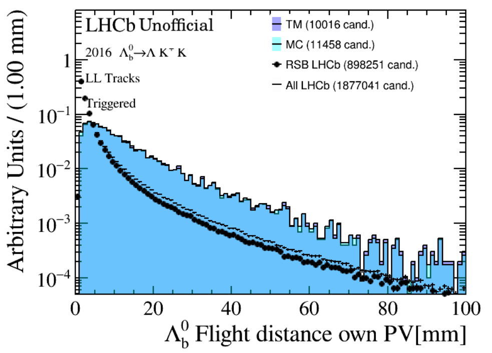

(e) Flight distance of Λ_b^0 with respect to its own PV.

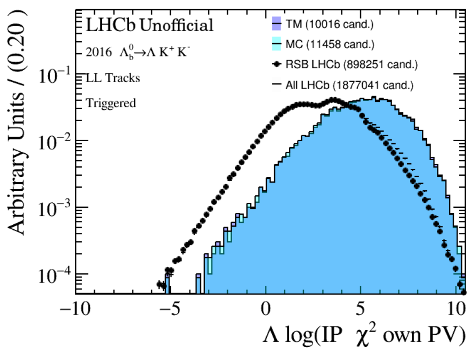

(f) $\log(\chi^{2\ \mathrm{OwnPV}}_{\Lambda})$, $\chi^{2\ \mathrm{OwnPV}}_{\Lambda}$ is χ^2 of the decay in which Λ would originate from its own PV (not from Λ_b^0 decay).

Figure 5.3 – Distributions of examples of input variables for *LL* ML classifier training. The distribution of simulated MC events (teal) is identical with MC *TruthMatched* events (light blue). Normalised distribution of upper mass side band events (black dots) overlays with the distribution of all events (black lines).

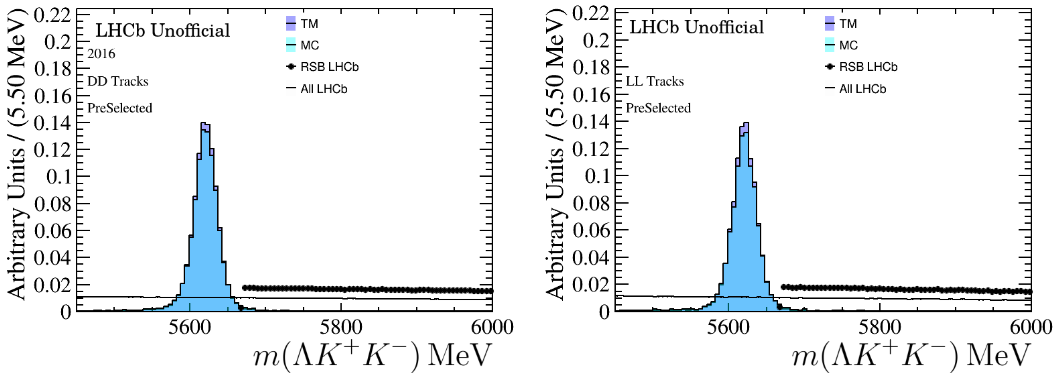

(a) DD sample in 2016 (b) LL sample in 2016

Figure 5.4 – Normalised invariant-mass distributions of the ΛK^+K^- system in the normalisation mode 2016 sample. Each distribution is normalised to unity. Overlaying histograms correspond to the MC simulated events (light-blue) and their subset - TruthMatched events (purple). The black line represents events recorded by the LHCb detector and their subset - upper mass side-band is represented by black points.

Fig. 5.4) to model combinatorial background.

Firstly, an iterative evaluation of the performance of classifiers trained with various sets of input variables is established, then the minimal-size set of input variables that exhibit maximal separation power is identified and used for the final training.

The *XGBoost* algorithm [55] is selected as an optimal classifier for this analysis both in *DD* and *LL* samples. The decision is based on a comparison of receiver operating characteristics (*ROC*) - a graphical representation for analysing the performance of a classifier using a pair of statistics true positive rate and false positive rate - for all the algorithms considered. The final set of variables used for training consists of:

- Transverse momentum of the Λ_b^0 candidate, p_{T}.
- Pseudo-rapidity of the Λ_b^0 candidate, $\eta_{\Lambda_b^0}$.
- $\ln(1 - D_{\Lambda_b^0})$, where $D_{\Lambda_b^0}$ is DIRA of the Λ_b^0 candidate with respect to its *own PV* - the primary vertex from which it originates. The own PV is selected as the vertex with the lowest value of $\chi^2(IP)$ in a set of reconstructed vertices aligned with the decay topology (decay chain is “pointing” towards the vertex).
- $\ln(\chi^{2\ \mathrm{Endvertex}}_{\Lambda_b^0})$, where $\chi^{2\ \mathrm{Endvertex}}_{\Lambda_b^0}$ is the χ^2 of the Λ_b^0 decay vertex.
- Λ_b^0 flight distance with respect to its own PV.
- $\ln(\chi^{2\ \mathrm{OwnPV}}_{\Lambda})$, $\chi^{2\ \mathrm{OwnPV}}_{\Lambda}$ is χ^2 of the decay in which Λ would originate from its own PV (not from the candidate Λ_b^0 decay).

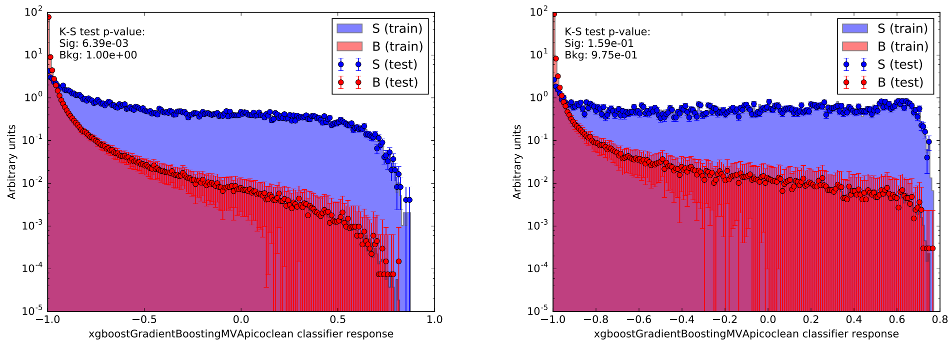

(a) DD track sample.

(b) LL track sample.

Figure 5.5 – The distributions of the classifier response to training signal events (blue histogram), testing signal events (blue dots), training background events (red histogram) and testing background events (red points).

The ML framework is developed and used to evaluate each of the studied events and calculate its classifier value S_{MVA}, which numerically indicates whether this event is signal-like or background-like. It was checked that no correlation is observed in background events between the reconstructed invariant mass of the system and the classifier output S_{MVA} nor any of the selected input variables.

The respective classifier response distributions are shown in Fig. 5.5 for signal and background. The corresponding p-values of the Kolmogorov–Smirnov test [56] are also indicated in the figures confirming that signal identification does not suffer from over-training. [III]

The use of the second classifier trained with $\Lambda_b^0 \to \Lambda p\overline{p}$ events is considered and tested. Yet it is found to be unnecessary given the resulting performance is equivalent to the nominal one within the uncertainties. Therefore, the classifiers trained on $\Lambda_b^0 \to \Lambda K^+K^-$ samples are used both for the $\Lambda_b^0 \to \Lambda K^+K^-$ and $\Lambda_b^0 \to \Lambda p\overline{p}$ channels.

Particle identification (PID)

Particle identification (PID) is used to estimate for each of Λ_b^0 daughter particles the compatibility with hypothesis of being a pion, proton, kaon, etc. The PID is based on detector-related information. These are for example: information from the *RICH sub-detectors* (See Section 3.2.3), number of tracks and their properties, quality of the track fit, activation of specific regions of the detector and other LHCb sub-detector systems, etc. These variables are evaluated with ML algorithms trained on reference particle signatures in the LHCb detector. A combined PID selection variable for reconstructed daughters K^+ K^- is constructed from

[III] Kolmogorov–Smirnov test performs the hypothesis testing of independence of distributions obtained from training and testing samples. The null hypothesis is that the two distributions are identical, rejecting the null hypothesis indicates potential over-training as the classifier response potentially differently to the training and testing samples.

above mentioned compatiblities in the normalisation channel as follows:

$$P_C^K = P_K^{K^+}.P_K^{K^-}.(1-P_\pi^{K^+}).(1-P_\pi^{K^-}).(1-P_p^{K^+}).(1-P_p^{K^-}),$$

where $P_K^{K^{+(-)}}$ indicates the compatibility of the particle reconstructed as $K^{+(-)}$ with being a kaon, $P_\pi^{K^{+(-)}}$ the compatibility of the particle reconstructed as $K^{+(-)}$ with being a pion, and $P_p^{K^{+(-)}}$ the compatibility of the particle reconstructed as $K^{+(-)}$ with being a proton. The combined PID selection for proton daughters in the $\Lambda_b^0 \to \Lambda p\overline{p}$ signal channel, P_C^p, is defined similarly (kaons and protons are interchanged with respect to the normalisation channel). The mentioned compatiblities are obtained as an output from the *ProbNN* [57], classifier trained separately for each of the particle species. In order to account for differences between PID distributions observed in MC simulations and measured in the LHCb experiment, a correction using the *PIDCorr* package is applied and only the corrected values are used.

The PID correction using the *PIDCorr* package is calculated based on track kinematic properties (momentum and pseudo-rapidity) and event multiplicity (number of reconstructed tracks). The correction is done with an unbinned approach, where the calibration *Probablilty density functions (PDFs)* in four dimensions (nominal PID response, P_{T}, η, N_{tracks}) are described by a kernel density estimation procedure using the *Meerkat library* [58] and so called *Calibration samples*. These are dedicated data samples collected by the LHCb detector that contain a set of specific calibration decay channels. Tracks associated with the known final state particles in these calibration channels are used as a reference. Coverage of the full momentum range of the calibration samples is verified.

Simultaneous optimisation of the combined MVA-PID selection

In order to select optimal requirements on the MVA output, S_{MVA}, and the S_{PID} on the output of described PID function function P_C^K, the maximum of the Punzi figure of merit [59] is found in the 2-dimensional plane of the MVA versus P_C^K variables. The Punzi figure of merit is defined as:

$$F = \frac{\varepsilon_S(S_{MVA}, S_{PID})}{\frac{a}{2} + \sqrt{N_B(S_{MVA}, S_{PID})}}, \tag{5.6}$$

where ε_S is the efficiency estimated from signal simulation samples, $a = 5$ is the desired significance and N_B is the expected number of background events inside the signal invariant mass region (5620.2 ± 18.0 MeV). Signal invariant mass region size around the nominal invariant mass is motivated by the simulation as a vast majority of simulated signal events is present in this interval.A linear function which describes the background populating the upper-mass side-band is established by fitting. The N_B value is calculated using an extrapolation of this function and its subsequent integration over the signal region. Simultaneously optimised values are found separately for each of the two Λ categories (*DD* and *LL*) in the corresponding optimisation planes. The binning of each plane is a result of an iterative optimisation with

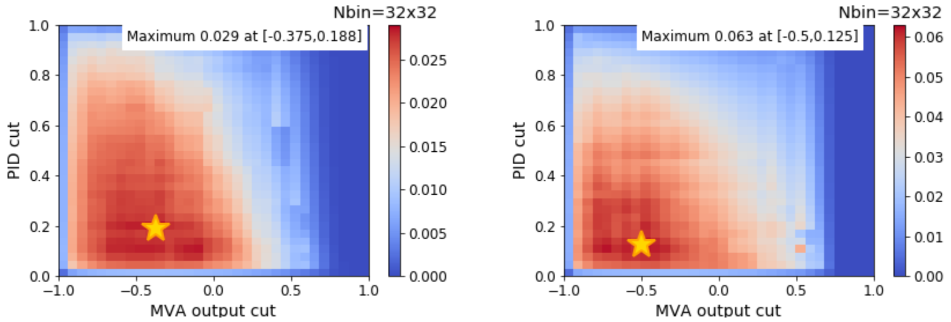

(a) DD track sample for $\Lambda_b^0 \to \Lambda K^+K^-$. (b) LL track sample for $\Lambda_b^0 \to \Lambda K^+K^-$.

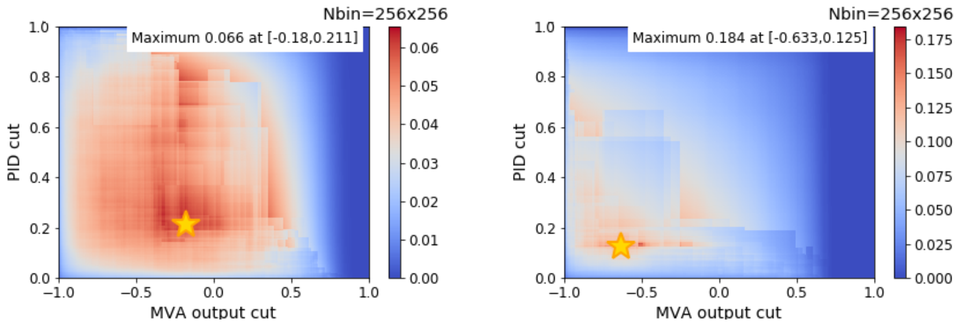

(c) DD track sample for $\Lambda_b^0 \to \Lambda p\overline{p}$. (d) LL track sample for $\Lambda_b^0 \to \Lambda p\overline{p}$.

Figure 5.6 – Values of the Punzi figure of merit across the the 2-dimension optimisation plane constructed from all possible MVA cut P_C^K cut values combinations. The optimum is indicated with a star.

doubling number of bins on each axis (2 × 2, 4 × 4, 8 × 8, etc.). After each bin split, the position of the maximum is identified. If the maximum is found in a sub-bin of the bin in which it was contained at the previous iteration, bins are further split. If not, the binning and optimal points from the previous iteration are considered final. This final binning choice is the last stable configuration before the minimum is found outside of the region where it was previously localised due to low per-bin statistics. Results can be seen in Fig 5.6. To be explicit the MVA and PID requirements in the normalisation mode are −0.375 and 0.188 in the *DD* sample, and −0.5 and 0.125 in the *LL* sample. Similarly for the signal channel, the requirements are −0.18 and 0.211 in the *DD* sample and −0.633 and 0.125 in the *LL* sample.

The following numbers of bins are used: 32x32 in normalisation channel $\Lambda_b^0 \to \Lambda K^+K^-$ and 256x256 in the signal channel $\Lambda_b^0 \to \Lambda p\overline{p}$. The larger number of bins in the signal channel $\Lambda_b^0 \to \Lambda p\overline{p}$ is related to a higher population density in the region of the optimum (the sample sizes used for the evaluation are equivalent).

As a complementary study, an alternative approach to the optimisation of the combined MVA-PID selection is presented in Appendix A.1.

5.3.5 Charm vetoes

As it will become evident from the background studies presented in Section 5.4, several vetoes are required in order to remove potential contamination from charm hadron intermediate states. The full list of charm vetoes is summarised in Table 5.9. The cut values in place are motivated by estimates of the mass resolution of the relevant particle combinations. The restriction to the region $m_{h\bar{h}} < 2.85\,\text{GeV}$, where h is a kaon or a proton, is motivated by the observation of resonance-like structure in the invariant mass spectra of the K^+K^- subsystem, which is consistent with $\chi_{c0}(1P)$ meson and hence, suggests $\Lambda_b^0 \to \Lambda\chi_{c0}(1P)$ as a new decay mode. As the decay $\Lambda_b^0 \to \Lambda\chi_{c0}(1P)$ with the subsequent $\chi_{c0}(1P) \to K^+K^-$ decay is a charm mode, it is not investigated further in this analysis.

Table 5.9 – Selection requirements applied to the vertex-fitted Λ_b^0 candidate. The symbol $m_{K^+K^-}^{K^+\pi^-}$ represents invariant mass of the K^+K^- two-body sub-system in which the pion invariant mass is assigned to the K^-, $m_{K^+K^-}^{\pi^+K^-}$ is defined analogously. Nominal invariant masses are taken from Ref. [6].

$\Lambda_b^0 \to \Lambda K^+K^-$	
$\lvert m_{K^+K^-} - m_{D^0}\rvert$	$> 30\text{MeV}$
$\lvert m_{\Lambda K^+} - m_{\Lambda_c^+}\rvert$	$> 30\text{MeV}$
$\lvert m_{\Lambda K^+} - m_{\Xi_c^+}\rvert$	$> 30\text{MeV}$
$\lvert m_{K^+K^-}^{K^+\pi^-} - m_{D^0}\rvert$	$> 30\text{MeV}$
$\lvert m_{K^+K^-}^{\pi^+K^-} - m_{D^0}\rvert$	$> 30\text{MeV}$
$m_{K^+K^-}$	$< 2.85\,\text{GeV}$
$\Lambda_b^0 \to \Lambda p\overline{p}$	
$m_{p\bar{p}}$	$< 2.85\,\text{GeV}$

5.3.6 Multiple candidates

There is more than one signal candidate in a small fraction of events ($\leq 0.41\%$ of all events). For each of those events, only one randomly selected of the reconstructed candidates is chosen.

5.3.7 Event selection summary

After applying the requirements based on the simultaneously optimised values of S_{MVA} and P_C, the resulting distributions are studied. For the LHCb samples, the distributions for each of the considered years of data taking (2016-2018) are consistent with each other while samples from 2015 have lower number of recorded events. As an example, distributions of LHCb events collected during 2016 are provided in Fig 5.7.

The regions of invariant mass of Λ_b^0 and Ξ_b^0 for the signal channel are blinded since the

Table 5.10 – The overall summary of events passing the full selection

Channel	$\Lambda_b^0 \to \Lambda K^+K^-$		Blinded $\Lambda_b^0 \to \Lambda p\overline{p}$	
Sample	DD	LL	DD	LL
2015	69	37	12	6
2016	471	218	59	28
2017	530	203	82	28
2018	537	231	106	31

beginning of the analysis. The remaining side-bands and the central region between two blinded sections are presented in Figure 5.8. Distributions of the signal and normalisation channel events in MC simulations are discussed along with backgrounds in Section 5.4 below. The overall summary of events passing the full selection is provided in the Table 5.10. Indicated values correspond to the number of events in the full studied range in case of the normalisation mode $\Lambda_b^0 \to \Lambda K^+K^-$ and to the non-blinded regions of the signal mode $\Lambda_b^0 \to \Lambda p\overline{p}$.

5.4 Background studies

There is in principle a variety of sources of background to the ΛK^+K^- and $\Lambda p\overline{p}$ spectra, which we discuss below. Their relevance for the description of the LL and DD samples is evaluated independently.

In order to estimate the expected contributions from the background modes in the studied spectra of $\Lambda_b^0 \to \Lambda K^+K^-$ and $\Lambda_b^0 \to \Lambda p\overline{p}$ channels, events passing the full selection without charm vetoes are studied. The charm vetoes are not included in these estimates as their efficiencies cannot be obtained from the simulations. This is because the distributions of variables describing the invariant mass of two-body subsystems in the used simulation do not model the LHCb data correctly. In fact, simulation is produced with uniform distributions in

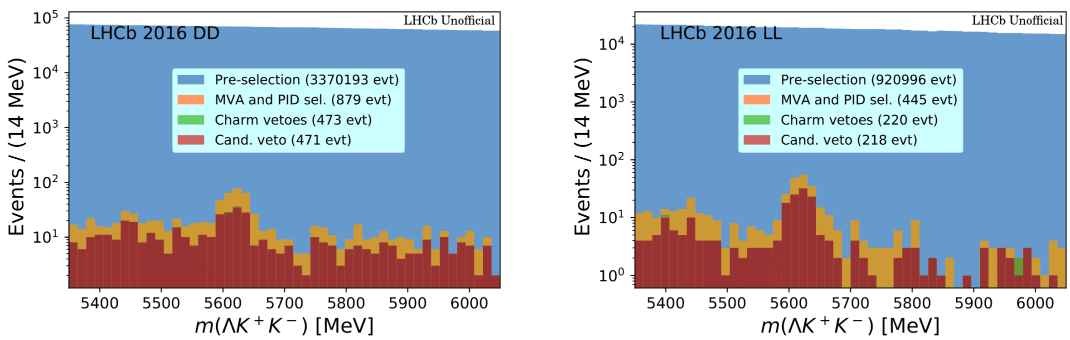

(a) DD sample. (b) LL sample.

Figure 5.7 – Invariant mass distributions of the ΛK^+K^- system in the normalisation channel $\Lambda_b^0 \to \Lambda K^+K^-$ in the 2016 data samples.

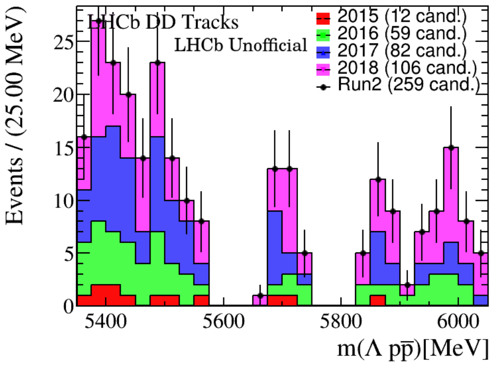

(a) DD sample.

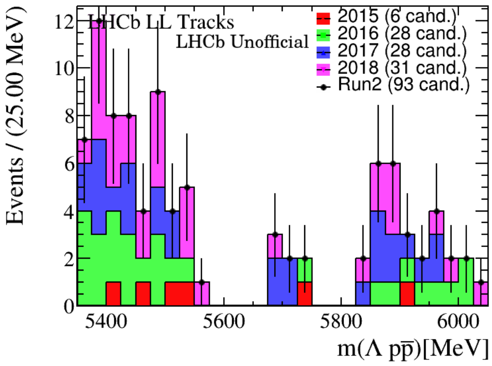

(b) LL sample.

Figure 5.8 – Invariant mass distributions of the $\Lambda p\overline{p}$-system in the signal channel $\Lambda_b^0 \to \Lambda p\overline{p}$ with blinded signal regions in the 2016 data samples.

Squared Dalitz variables as discussed in Section 5.2.2. As charm vetoes can only reduce the background yields, the expected yields of background contributions without charm vetoes are known to be potentially overestimated (considered conservative).

Values of branching fractions $\mathscr{B}$ are taken from Ref. [6] for the established channels. In case of non-established channels, values are estimated based on similarity to already established channels and on phenomenological considerations. In case of the signal channel $\Lambda_b^0 \to \Lambda p\overline{p}$, value of branching fraction discussed in Section 2.2 is used. Calculations also involve the estimates of fragmentation fractions[IV] $\mathscr{F}$ based on the quark content of involved particles, detector acceptances ϵ^{Acc} and event selection efficiencies calculated without the charm vetoes ϵ^{Sel}. Finally, the yield in the normalisation channel $N^{fit}_{LHCb,\Lambda_b^0\to\Lambda K^+K^-}$ is used for the background calculations. It is based on the fit model discussed in Section 5.8, which is applied to the 2016 LHCb sample passing the selection *without* charm vetoes.

The resulting estimates Y_j of background mode j contribution to the normalisation channel $Y^{\Lambda_b^0\to\Lambda K^+K^-}$ and the signal $Y^{\Lambda_b^0}\to\Lambda p\overline{p}$ are products of the following equation

$$Y_j = N^{fit}_{LHCb,\Lambda_b^0\to\Lambda K^+K^-} \frac{\mathscr{F}_j \mathscr{B}_j \epsilon_j^{Acc} \epsilon_j^{Sel}}{\mathscr{F}_{\Lambda_b^0\to\Lambda K^+K^-} \mathscr{B}_{\Lambda_b^0\to\Lambda K^+K^-} \epsilon^{Acc}_{\Lambda_b^0\to\Lambda K^+K^-} \epsilon^{Sel}_{\Lambda_b^0\to\Lambda K^+K^-}} \tag{5.7}$$

and they are summarised in Table 5.11 showing that none of the considered background contributions is significant.

The estimates are calculated from the numbers of simulated events passing the event selection without vetoes, corrected using the respective fragmentation fractions, detection acceptances,

[IV] Fragmentation fractions used in terms of ratios depending on the particle of of origin. The particle of origin in the normalisation mode is Λ_b^0 baryon. If that particle of origin in the examined decay mode is also Λ_b^0 baryon, the relative fragmentation fraction used is equal to 1. If the particle of origin is B_s (B_0) meson, the values of the relative fragmentation fraction 0.56 (2.36).

events selection efficiencies and branching fractions. Estimates for the signal channel decays are calculated based on theoretically predicted signal branching fractions discussed in Section 2.2.

In addition to the discussed physics background sources, *combinatorial background* formed by random track combinations is also considered to contribute significantly and it is therefore included in the fit model.

Distributions of reconstructed invariant mass for the decay products in the normalisation channel $\Lambda_b^0 \to \Lambda K^+K^-$ are shown in Figure 5.9, where we can observe the effects of the selection on the simulated signal decays and on the background channels that are considered. Similarly, Figure 5.10 shows the corresponding distributions for the signal channel $\Lambda_b^0 \to \Lambda p\overline{p}$[V].

5.4.1 Reflections from $\Lambda_b^0 \to \Lambda hh'$ decays

A single or double meson misidentification in $\Lambda_b^0 \to \Lambda hh'$ decays could possibly contaminate the ΛK^+K^- and $\Lambda p\overline{p}$ spectra. However, as the values of the estimated yields in the considered channels indicate in Table 5.11, none of those backgrounds would contribute significantly. Hence none of them is studied further nor included in the final fit model.

5.4.2 Background from decays of charmed hadrons

In order to prevent signal contamination with charm intermediate states formed by the two bachelor final-state hadrons, candidates with K^+K^- (normalisation $\Lambda_b^0 \to \Lambda K^+K^-$ spectrum)

[V]Distributions in the simulated samples of 2016,2017 and 2018 are nearly identical, 2018 example for the signal $\Lambda_b^0 \to \Lambda p\overline{p}$ is provided

Table 5.11 – Signal and normalisation mode along with the list of considered sources j of background and the corresponding expected yields in LHCb 2016 dataset in normalisation $Y_j^{\Lambda_b^0 \to \Lambda K^+K^-}$ and signal $Y_j^{\Lambda_b^0 \to \Lambda p\overline{p}}$ modes for LL and DD track Λ candidates.

Mode j	$Y_{j,DD}^{\Lambda_b^0 \to \Lambda K^+K^-}$	$Y_{j,LL}^{\Lambda_b^0 \to \Lambda K^+K^-}$	$Y_{j,DD}^{\Lambda_b^0 \to \Lambda p\overline{p}}$	$Y_{j,LL}^{\Lambda_b^0 \to \Lambda p\overline{p}}$
$\Lambda_b^0 \to \Lambda K^+K^-$	257	177	$\ll$1	$\ll$1
$\Lambda_b^0 \to \Lambda p\bar{p}$	$\ll$1	$\ll$1	71	39
$B_s \to K_S p\bar{p}$	$\ll$1	$\ll$1	1.2	$\ll$1
$\Lambda_b^0 \to K_S\pi^+\bar{p}$	$\ll$1	$\ll$1	$\ll$1	$\ll$1
$\Lambda_b^0 \to \Lambda\pi^+\pi^-$	$\ll$1	$\ll$1	$\ll$1	$\ll$1
$B_s \to K_S K^+\pi^-$	1.6	0.2	$\ll$1	$\ll$1
$\Lambda_b^0 \to \Lambda K^+\pi^-$	5.0	2.7	$\ll$1	$\ll$1
$B_0 \to K_S K^+K^-$	6.6	0.7	$\ll$1	$\ll$1

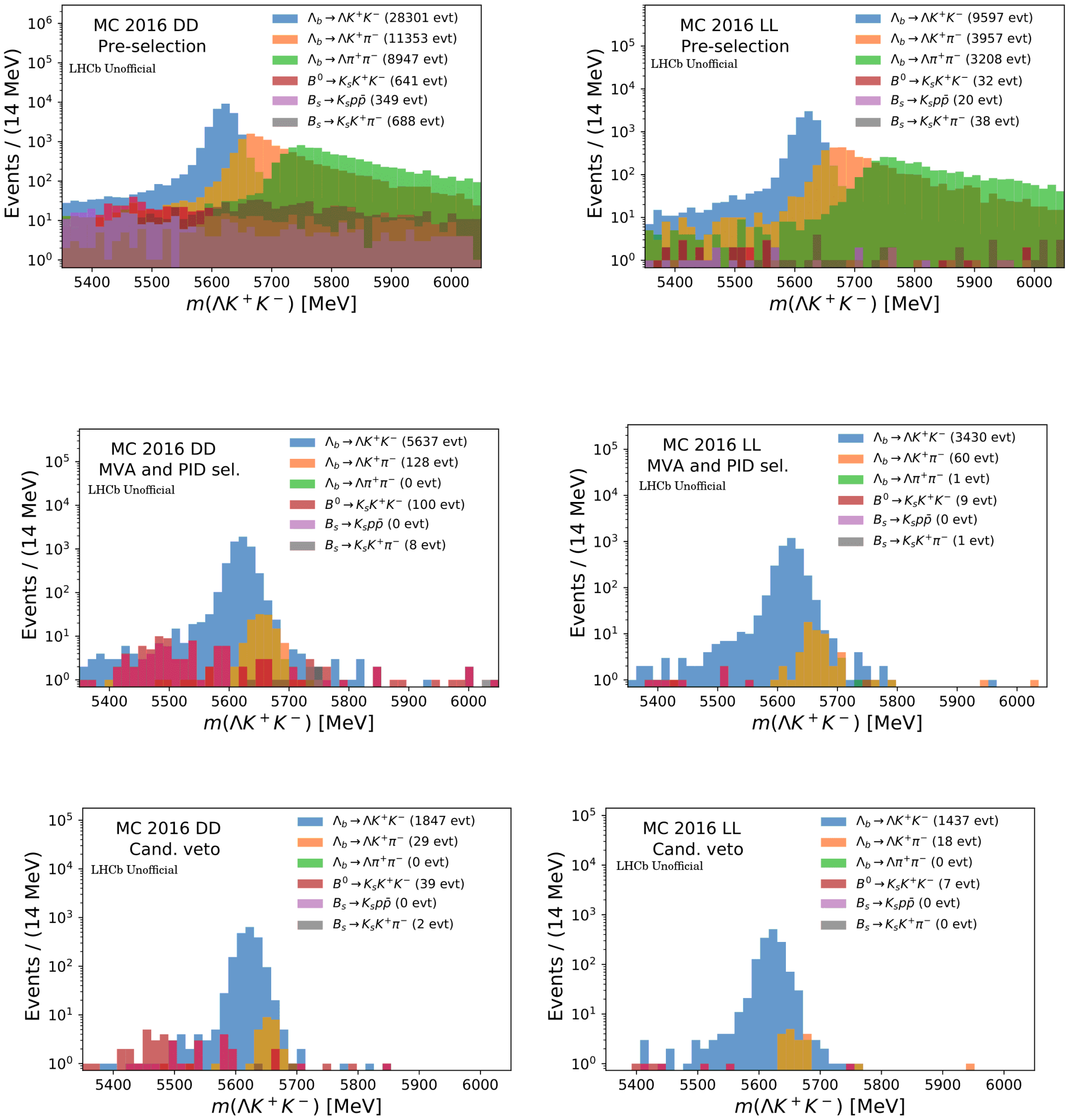

Figure 5.9 – MC distributions of the reconstructed invariant mass of the decay products in the normalisation $\Lambda_b^0 \to \Lambda K^+K^-$ channel on MC events corresponding to the 2016 period of data taking in DD samples (left) and LL samples (right). They show the effect of different stages of the event selection: After the trigger, stripping and pre-selection (top), after the MVA and PID selection (middle), and after charm vetoes and multiple candidate removal. Selections are not only suppressing combinatorial background by three orders of magnitude but also suppressing possible background contributions from other b-hadron decay modes. Note that the yields in the simulated channels are not normalised with respect to each other as after the normalisation none of the background modes would be visible.

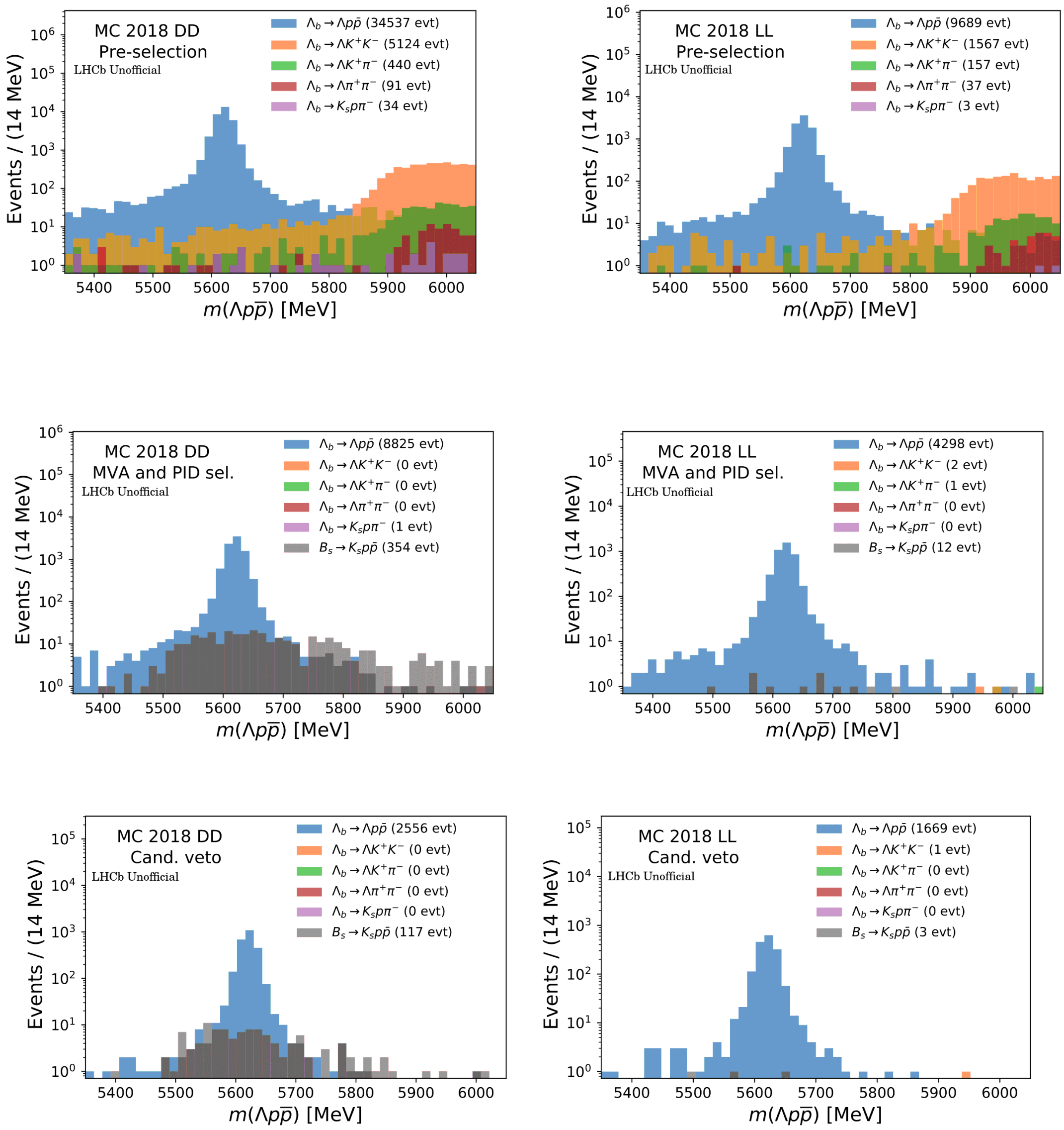

Figure 5.10 – MC distributions of the reconstructed invariant mass of the decay products in the signal $\Lambda_b^0 \to \Lambda p\overline{p}$ channel on MC events corresponding to the 2018 period of data taking in DD samples (left) and LL samples (right). They show the effect of different stages of the event selection: After the trigger, stripping and pre-selection (top), after the MVA and PID selection (middle), and after charm vetoes and multiple candidate removal. Selections are not only suppressing combinatorial background by three orders of magnitude but also suppressing possible background contributions from other b-hadron decay modes. While the contributions from the background channels pass the pre-selection (optimised for combinatorial background substraction) they are eliminated after the MVA and PID selection. Note that the yields in the simulated channels are not normalised with respect to each other as after the normalisation none of the background modes would be visible .

or $p\overline{p}$ (signal $\Lambda_b^0 \to \Lambda p\overline{p}$ spectrum) invariant mass higher than 2.85 GeV are removed. This requirement value is motivated by the excess at the $\chi_{c0}(1P)$ mass, 3414 MeV, in the K^+K^- invariant mass spectra in the normalisation mode.

The evidence for this charmonium resonance in the sample raises the concern that the charmless decay $\Lambda_b^0 \to \Lambda K^+K^-$ may be contaminated by $b \to c$ transitions in $\Lambda_b^0 \to \Lambda\chi_{c0}(1P)$ decays or similar decays with $c\bar{c}$ resonances. Since it is difficult to identify the charmonium resonances that contribute to $\Lambda_b^0 \to \Lambda K^+K^-$, and because most of these resonances decay to the $p\overline{p}$ final state, all potential charmonium contributions for both modes are removed. The requirement value of 2.85 GeV is motivated by the mass and width of non-trivial structure of η_c-meson contribution contaminating the region. Fig. 5.11 distributions without this veto are showing the reconstructed invariant mass of two-body subsystems K^+K^- in the combined Run2 sample with $\Lambda_b^0 \to \Lambda K^+K^-$ decays in the signal region $m(\Lambda K^+K^-) \in [5602.2, 5638.2]$ MeV.

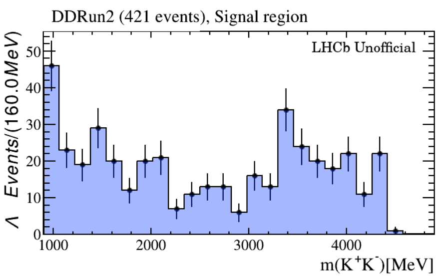

(a) Events with Λ-baryons in DD sample.

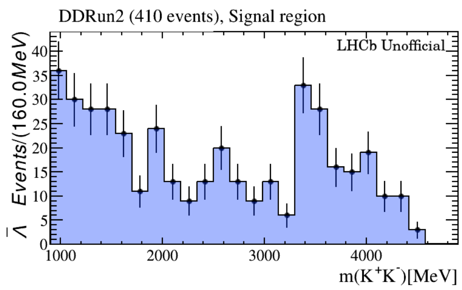

(b) Events with $\overline{\Lambda}$-baryons in DD sample.

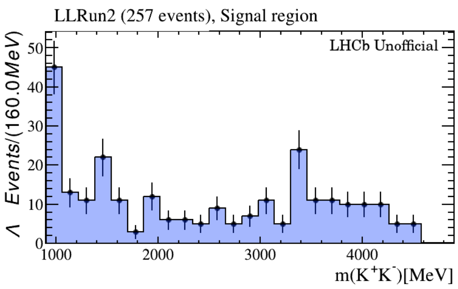

(c) Events with Λ-baryons in LL sample.

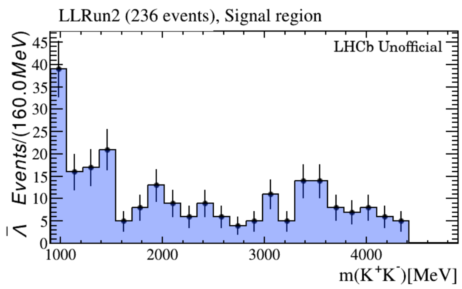

(d) Events with $\overline{\Lambda}$-baryons in LL sample.

Figure 5.11 – Distributions of the reconstructed invariant mass of two-body subsystems K^+K^- in the combined Run2 sample with $\Lambda_b^0 \to \Lambda K^+K^-$ decays in the signal region $m(\Lambda K^+K^-) \in [5602.2, 5638.2]$ MeV.

One can consider reducing the range of the vetoes to include the region of m($p\overline{p}$)>3.75 GeV. This value marks the charmonia the $D\bar{D}$ meson pair production threshold. Therefore, it should not lead to a peaking contribution in the signal mode above this threshold. Consequently, the full region outside of 2.85 GeV<m($p\overline{p}$)<3.75 GeV is stored for the future studies.

For the $\Lambda_b^0 \to \Lambda K^+K^-$ mode, states formed in combination with a Λ baryon are also removed if the invariant mass of the ΛK^+ system is close to the invariant mass of a Λ_c^+ or a Σ_c^+ baryon. Furthermore, those $\Lambda_b^0 \to \Lambda K^+K^-$ candidates for which the invariant mass of the two-body

K^+K^- sub-system is close to the invariant mass of the D^0 meson are vetoed. All these vetoes are collected in Table 5.9.

5.4.3 Background from decays containing K_S^0 mesons

The influence of proton-pion misidentification in the reconstruction and selection of the Λ baryon arising from K_S^0 cross-feed is also checked. Related sources of background to the $\Lambda p\overline{p}$ spectra could arise *e.g.* from the family of $B^0_{(s)} \to K_S^0 hh'$ decays, from $B^0_{(s)} \to K_S^0 p\bar{p}$ decays, or from $\Lambda_b^0 \to K_S^0 ph$ decays.

In order to possibly improve discrimination between the K_S^0 and the Λ without any PID the Armenteros-Podolanski (AP) plot [60] is exploited: One defines

$$\begin{aligned} Q_T &= p^+ \sin\phi^+ = p^- \sin\phi^- \quad \text{and} \\ \alpha &= \frac{p_L{}^+ - p_L{}^-}{p_L{}^+ + p_L{}^-} \quad \text{with } p_L{}^\pm = p^\pm \cos\phi^\pm \quad , \end{aligned} \tag{5.8}$$

where the $\pm$ superscripts denote the daughter charge, $p^\pm$ are the daughter momenta and $\phi^\pm$ the angle between the daughter and the V^0 momenta in the laboratory frame.

The AP plot for both Λ and K_S^0 candidates after the full $\Lambda_b^0 \to \Lambda K^+K^-$ selection in simulated MC samples as well as selected LHCb events are shown in Fig. 5.12. All figures have been produced without a constraint on the mass of the Λ baryon.

The symmetry of the K_S^0 decay is visible as are the two bands containing the Λ and $\overline{\Lambda}$ candidates. A very small contamination from K_S^0 decays is visible exclusively in the region where K_S^0 and Λ ellipses overlap. Most likely, the contribution is combinatorial background from the formation of a K_S^0 with two other tracks. Therefore, the contribution is thought to be small enough (after applying PID requirements) not to affect the analysis and no AP based requirements are introduced.

5.4.4 Backgrounds from falsely reconstructed Λ baryons

Both normalisation and signal channel contain a reconstructed Λ. We consider backgrounds in which the p and π^- hadrons in the decay products of hypothetical channels $\Lambda_b^0 \to p\overline{p}p\pi^-$ or $\Lambda_b^0 \to K^+K^-p\pi^-$ can be falsely reconstructed as a Λ baryon. However, these cases are heavily suppressed by the pre-selection criteria (see Table 5.8). In particular, the requirement of a distance in z-coordinates of Λ_b^0 and Λ rules out cases where all the final state particle tracks originate from the same point. In addition, selection requirements in stripping such the χ^2 separation of the Λ candidate and its associated PV reduces this possibility even further. Nevertheless, the possible associated systematic uncertainty is addressed in the Section 6.3.5.

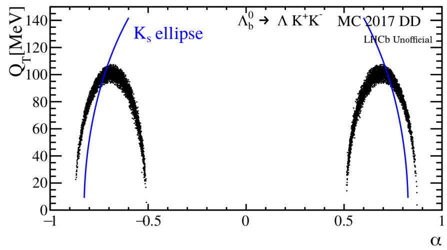

(a) Simulated decays of $\Lambda_b^0 \to \Lambda K^+ K^-$.

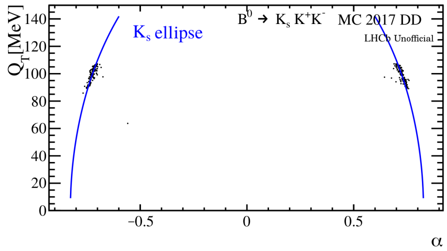

(b) Simulated decays of $B^0 \to K_S^0 K^+ K^-$.

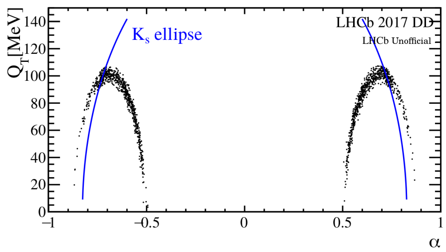

(c) LHCb decays reconstructed under the $\Lambda_b^0 \to \Lambda K^+ K^-$ hypothesis.

Figure 5.12 – Armenteros-Podolansky plots with K_S^0 AP-ellipses. The example uses the 2017 DD dataset after full selection.

5.4.5 Partially reconstructed backgrounds

Decay modes with a π^0

The decay modes $\Lambda_b^0 \to \Lambda p\overline{p}\pi^0$ and $\Xi_b^0 \to \Lambda p\overline{p}\pi^0$, so far unobserved, can in principle contribute to the $\Lambda p\overline{p}$ spectrum, *mutatis mutandis* for the case of the $\Lambda K^+ K^-$ spectrum. Also, the channel $\Lambda_b^0 \to \Lambda K^{*+} K^-$, where K^{*+} decays as $K^{*+} \to K^+\pi^0$, is investigated.

A simplified simulation can be used to determine the expected shape of these partially reconstructed decays based on kinematic considerations. In so called *toy simulation* the distribution of the decay products is uniform in the phase space and the generated events do not undergo the full reconstruction using the same software used to reconstruct the data. Instead, the detector resolution is included by smearing the momentum of the final state particles with an appropriate Gaussian distribution.

With this simulation, Figure 5.13 shows two examples of resulting invariant mass distributions in the channels $\Lambda_b^0 \to \Lambda K^+ K^- \pi^0$ and $\Lambda_b^0 \to \Lambda p\overline{p}\pi^0$. Similarly, $\Lambda_b^0 \to \Lambda K^{*+} K^-$ candidates are illustrated in Figure 5.14. As the spectra of $\Lambda_b^0 \to \Lambda K^+ K^- \pi^0$ and $\Lambda_b^0 \to \Lambda K^{*+} K^-$ are nearly identical, only the mode $\Lambda_b^0 \to \Lambda K^+ K^- \pi^0$ is considered further and it is assumed to cover contributions both from $\Lambda_b^0 \to \Lambda K^+ K^- \pi^0$ and $\Lambda_b^0 \to \Lambda K^{*+} K^-$ decays. Note that the mass shift towards low masses is due to unreconstructed π^0 meson and the endpoint of the distribution is equal to the invariant mass of Λ_b^0 baryon $m_{\Lambda_b^0}$ minus the mass of the unreconstructed particle.

Background from decays with a Σ^0 hadron

Contributions from modes $\Lambda_b^0 \to \Sigma^0 K^+ K^-$ and $\Xi_b^0 \to \Sigma^0 K^+ K^-$ ($\Lambda_b^0 \to \Sigma^0 p\overline{p}$ and $\Xi_b^0 \to \Sigma^0 p\overline{p}$) containing a Σ^0 decaying into $\Sigma^0 \to \Lambda\gamma$, the γ escaping detection and reconstruction, are expected to leak into the normalisation (signal) region due to the small mass difference [6]

$$\Delta m = m(\Sigma^0) - m(\Lambda) = (76.959 \pm 0.023)\mathrm{MeV} \quad . \tag{5.9}$$

This background, modelled by a template shown in Fig. 5.15, again obtained with a toy simulation, is included in the description of normalisation channel spectrum.

Models with partially reconstructed backgrounds

Firstly, fit models with both partially reconstructed background sources (modes $\Lambda_b^0 \to \Lambda K^+ K^- \pi^0$ and modes $\Lambda_b^0 \to \Sigma^0 K^+ K^-$) are tested on LHCb data in the normalisation $\Lambda_b^0 \to \Lambda K^+ K^-$ channel. However, after including both of them to the model fits of the normalisation channel data confirmed that contributions from $\Lambda_b^0 \to \Lambda K^+ K^- \pi^0$ channels is consistent with zero for these unobserved modes. Furthermore, a significant correlation between the considered modes is observed implying model instability as the available data does not allow to distinguish both sources.

Therefore, only the background from $\Lambda_b^0 \to \Sigma^0 K^+ K^-$ decays with a hadron is explicitly included in the final fit model for the nomalisation channel $\Lambda_b^0 \to \Lambda K^+ K^-$ (see Section 5.7).

Also, after studying the side-band in the invariant-mass spectrum of the signal channel $\Lambda_b^0 \to \Lambda p\overline{p}$, it is concluded that neither of the partially reconstructed backgrounds channels

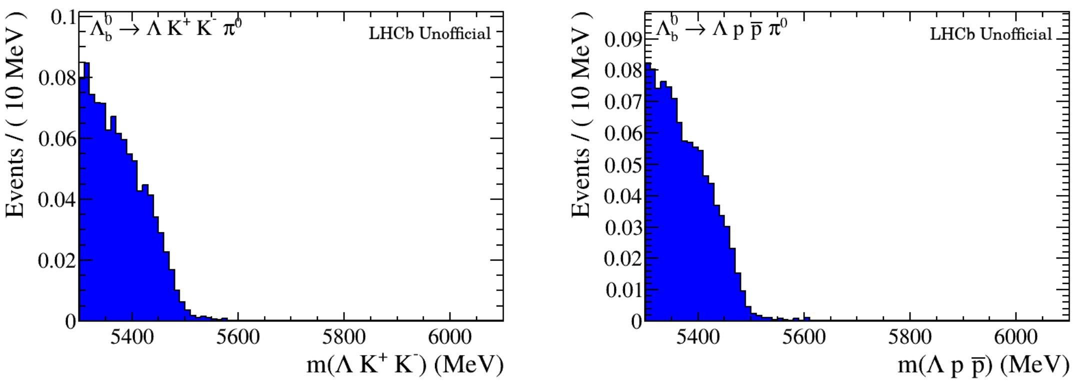

Figure 5.13 – Template (left) for $\Lambda_b^0 \to \Lambda K^+ K^- \pi^0$ decays in the $\Lambda K^+ K^-$ invariant mass and (right) for $\Lambda_b^0 \to \Lambda p\overline{p}\pi^0$ decays in the $\Lambda p\overline{p}$ invariant mass. Refer to the text for details.

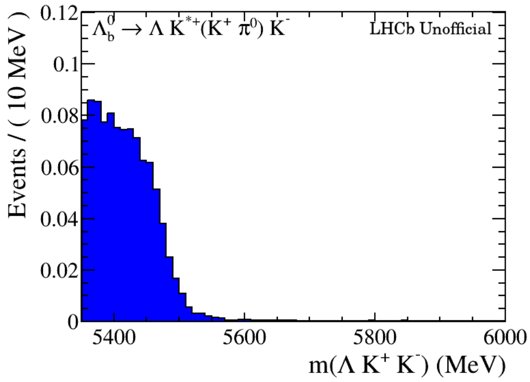

Figure 5.14 – Template for $\Lambda_b^0 \to \Lambda K^{*+}K^-$ decays in the ΛK^+K^- invariant mass.

needs to be included in the fit model describing the signal candidates.

5.4.6 Summary of background contributions

Only two types of backgrounds are included in the final fit model for the $\Lambda_b^0 \to \Lambda K^+K^-$ and the $\Lambda_b^0 \to \Lambda p\overline{p}$ modes. These are: *combinatorial background* formed by random track combinations (both modes), and partially reconstructed background intended to describe all cases with a missing photon ($\Lambda_b^0 \to \Lambda K^+K^-$ only).

5.5 Selection efficiencies

A precise description of the overall selection efficiencies is essential in order to perform the measurement of the branching fraction of $\Lambda_b^0 \to \Lambda p\overline{p}$ with respect to that of $\Lambda_b^0 \to \Lambda K^+K^-$. We calculate efficiencies in the studied interval of reconstructed invariant mass of the Λ_b^0 (Ξ_b^0) candidate:

$$m_{\Lambda hh} \in (5350, 6050)\,\mathrm{MeV}$$

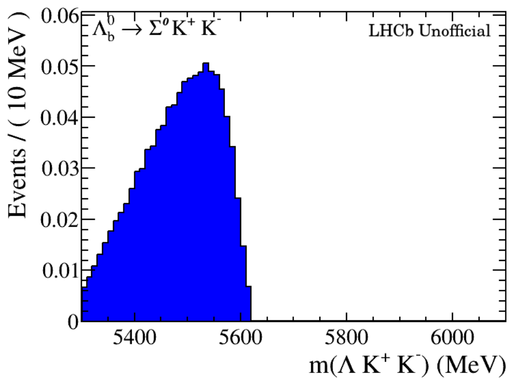

Figure 5.15 – Template for $\Lambda_b^0 \to \Sigma^0 K^+K^-$ decays in the ΛK^+K^- invariant mass.

The total selection efficiency is a combination of the following efficiencies of each selection step:

- Generator-level efficiency $\varepsilon^{\text{Gen.}}$.
- Reconstruction and stripping efficiency $\varepsilon^{\text{Reco.+strip.}}$.
- Trigger efficiency $\varepsilon^{\text{Trig.}}$.
- Offline selection efficiency $\varepsilon^{\text{Off.}}$, which combines pre-selection, MVA and PID efficiencies and efficiencies of the applied vetoes.

In the following sections only phase-space integrated efficiencies are reported. In case a significant signal is observed, corrections based on the phase-space signal distribution will be applied to the efficiencies for the branching fraction measurement.

All efficiencies below are provided with statistical uncertainties only. Systematic uncertainties to the total uncertainty are addressed in Section 6.7. Note that all efficiencies are based on simulated samples. This includes PID efficiencies, which are calculated from simulation after PID corrections based on the calibration samples are applied.

The following sections quote *binomial uncertainties* [61]. If the selection efficiency is calculated from the number of events passing the selection N and the total number of events on which selection is applied N_{Tot} as

$$\epsilon = \frac{N}{N_{Tot}}, \tag{5.10}$$

then the corresponding binomial uncertainty $\Delta\epsilon$ is equal to

$$\Delta\epsilon = \sqrt{N(1-\epsilon)}. \tag{5.11}$$

5.5.1 Generator-level efficiencies

It is required already at the generator level (see Section 3.2.6) that all the daughters are inside the LHCb detector geometrical acceptance. This implies that all daughters must satisfy the constraint on the angle between the particle momentum vector and direction of the beam axis oriented upstream the LHCb detector, θ: $10 < \theta < 400\,\text{mrad}$. Table 5.12 summarises the generator-level phase-space integrated efficiencies for the signal and normalisation channels.

5.5.2 Reconstruction and stripping efficiencies

It is required in the reconstruction of the signal (normalisation) channel that proton (kaon) pairs are reconstructed as `Long` tracks. Also, depending on the decay position of the Λ baryon, its daughters need to form a pair of `Long` tracks (LL) or a pair of `Downstream` tracks (DD).

Table 5.12 – Summary of generator-level efficiencies.

Year	Polarity	$\varepsilon^{\Lambda_b^0 \to \Lambda p\overline{p}}$ [%]	$\varepsilon^{\Lambda_b^0 \to \Lambda K^+K^-}$ [%]
2015	Up	23.81 ± 0.08	22.51 ± 0.08
	Down	23.91 ± 0.08	22.43 ± 0.08
2016	Up	23.73 ± 0.08	22.45 ± 0.08
	Down	23.98 ± 0.08	22.32 ± 0.08
2017	Up	23.84 ± 0.06	22.56 ± 0.06
	Down	23.87 ± 0.06	22.49 ± 0.06
2018	Up	23.96 ± 0.06	22.51 ± 0.06
	Down	23.93 ± 0.06	22.49 ± 0.06

Table 5.13 provides an overview of reconstruction and stripping efficiencies for the signal and normalisation channels.

Table 5.13 – Summary of reconstruction and stripping efficiencies and corresponding binomial errors (see Equation 5.10).

Mode	Year	$\varepsilon_{DD}^{\text{Reco.+strip.}}$ [%]	$\varepsilon_{LL}^{\text{Reco.+strip.}}$ [%]
$\Lambda_b^0 \to \Lambda p\overline{p}$	2015	1.269 ± 0.006	0.284 ± 0.003
	2016	1.301 ± 0.003	0.296 ± 0.002
	2017	1.368 ± 0.004	0.297 ± 0.002
	2018	1.373 ± 0.004	0.298 ± 0.002
$\Lambda_b^0 \to \Lambda K^+K^-$	2015	1.121 ± 0.005	0.294 ± 0.003
	2016	1.109 ± 0.003	0.318 ± 0.002
	2017	1.216 ± 0.003	0.322 ± 0.002
	2018	1.21 ± 0.003	0.321 ± 0.002

Tracking correction

The reported reconstruction efficiencies are based on the studies performed with simulation samples. Generally, these efficiencies may need to be corrected due to the possible differences at the tracking levels between the simulation samples and the data collected by the LHCb detector. Namely, track multiplicity, η and p_T could potentially differ. It is common to assess how events are distributed in p_{T}-vs-η map bins of tracking efficiency and hence calculate the average detection efficiency in the simulated sample taking into account the population of the candidates over the map bins. However, for the branching fraction ratio measurements only the ratio between the corrected efficiencies in signal and normalisation mode is relevant. Following the studies performed in Ref. [62] on channels similar to those studied here, the ratio of corrected tracking efficiencies between the signal and normalisation mode is expected to be consistent with 1 within the uncertainties.

However, the mentioned studies are performed with *TrackCalib* package [63], a tool for creating tracking efficiency correction tables allowing for user-defined track quality requirements, binning and variable combinations. The *TrackCalib* package does not take into account the nature of the particle as it considers only the pseudo-rapidity and transverse momentum. Therefore, this approach is associated with a systematic error (see Section 6.7.3). Based on previous studies [62], the error on the corrected efficiency ratio value is assumed to be negligible in comparison with the systematic error assigned on the method used.

5.5.3 Trigger efficiencies

The list of MC-based trigger efficiencies using *Truth-matched* decays in the analysed data-taking years is presented in Table 5.14. Efficiencies are provided for the L0 hardware trigger, HLT1 and HLT2 along with the total trigger efficiency in both track categories considered. These efficiencies are calculated from events passing stripping and reconstruction.

Table 5.14 – List of efficiencies of used trigger selection with the corresponding binomial errors.

Mode	Tracks	Year	ε^{L0}[%]	$\varepsilon^{\frac{HLT1}{L0}}$ [%]	$\varepsilon^{\frac{HLT2}{HLT1}}$ [%]	$\varepsilon^{Trigger}$[%]
$\Lambda_b^0 \to \Lambda p\overline{p}$	DD	2015	43.98 ± 0.26	84.36 ± 0.29	71.26 ± 0.39	26.44 ± 0.23
	DD	2016	46.83 ± 0.16	82.61 ± 0.18	77.63 ± 0.21	30.03 ± 0.14
	DD	2017	51.14 ± 0.16	82.77 ± 0.17	77.16 ± 0.21	32.66 ± 0.15
	DD	2018	43.25 ± 0.16	83.29 ± 0.18	81.65 ± 0.21	29.42 ± 0.15
$\Lambda_b^0 \to \Lambda p\overline{p}$	LL	2015	42.70 ± 0.53	94.61 ± 0.37	80.29 ± 0.67	32.44 ± 0.50
	LL	2016	45.36 ± 0.31	94.12 ± 0.22	84.03 ± 0.35	35.87 ± 0.30
	LL	2017	49.60 ± 0.32	94.18 ± 0.21	85.03 ± 0.34	39.72 ± 0.42
	LL	2018	41.52 ± 0.32	94.03 ± 0.24	86.84 ± 0.35	33.90 ± 0.32
$\Lambda_b^0 \to \Lambda K^+K^-$	DD	2015	46.62 ± 0.27	88.48 ± 0.25	74.28 ± 0.36	30.64 ± 0.25
	DD	2016	48.27 ± 0.17	87.41 ± 0.16	79.29 ± 0.21	33.45 ± 0.16
	DD	2017	53.38 ± 0.16	87.15 ± 0.15	77.96 ± 0.20	36.27 ± 0.16
	DD	2018	45.29 ± 0.16	87.65 ± 0.16	82.44 ± 0.20	32.73 ± 0.15
$\Lambda_b^0 \to \Lambda K^+K^-$	LL	2015	45.23 ± 0.51	96.37 ± 0.28	84.62 ± 0.56	36.89 ± 0.49
	LL	2016	47.15 ± 0.31	95.75 ± 0.18	86.86 ± 0.31	39.22 ± 0.31
	LL	2017	52.21 ± 0.31	95.77 ± 0.17	86.78 ± 0.30	43.39 ± 0.31
	LL	2018	43.49 ± 0.31	95.66 ± 0.19	89.24 ± 0.30	37.13 ± 0.30

5.5.4 L0 trigger efficiency correction

Imperfections in the MC simulation imply that the L0 trigger efficiencies of `L0Hadron_TOS` trigger line (see Section 3.2.4 and 5.3.1) may not correspond to the efficiencies measured in data. Therefore, a correction factor r can be introduced as

$$\varepsilon^{Corr.} = r\varepsilon^{MC} \tag{5.12}$$

where $\varepsilon^{Corr.}$ is the corrected efficiency and ε^{MC} is the efficiency obtained from MC simulation. For the purpose of the branching fraction measurement, it is essential to obtain the correct efficiency ratio

$$\frac{\varepsilon^{Corr.}_{\Lambda_b^0\to\Lambda p\overline{p}}}{\varepsilon^{Corr.}_{\Lambda_b^0\to\Lambda K^+K^-}} = \frac{r_{\Lambda_b^0\to\Lambda p\overline{p}}}{r_{\Lambda_b^0\to\Lambda K^+K^-}} \frac{\varepsilon^{MC}_{\Lambda_b^0\to\Lambda p\overline{p}}}{\varepsilon^{MC}_{\Lambda_b^0\to\Lambda K^+K^-}} \tag{5.13}$$

where $r_{\Lambda_b^0\to\Lambda p\overline{p}}$, $\varepsilon^{Corr.}_{\Lambda_b^0\to\Lambda p\overline{p}}$ and $\varepsilon^{MC}_{\Lambda_b^0\to\Lambda p\overline{p}}$ correspond to quantities defined for Equation 5.12 obtained for the signal channel $\Lambda_b^0\to\Lambda p\overline{p}$. Quantities for the normalisation channel $\Lambda_b^0\to\Lambda K^+K^-$ are defined analogously.

Given that signal $\Lambda_b^0\to\Lambda p\overline{p}$ and normalisation modes are topologically identical, the possible difference between $r_{\Lambda_b^0\to\Lambda p\overline{p}}$ and $r_{\Lambda_b^0\to\Lambda K^+K^-}$ can be related to the different selections applied in the two channels. Therefore, if one can demonstrate that the r factors are independent on the selection, they would cancel out in the Equation 5.13.

In order to demonstrate this independence, a method inspired by the *TISTOS* efficiency determination [51] is used.

Data driven efficiency determination method

This method takes an alternative approach to the trigger efficiency. It requires a sample where all the selection requirements are applied except the trigger requirement, so called *post-selection sample*. If we consider the number of events N_{Sel} in this sample, and number of events in a sample subset of events passing also the trigger requirements, $N_{Trig|Sel}$, *post-selection trigger efficiency* $\epsilon_{Trig|Sel}$ can be defined as

$$\epsilon_{Trig|Sel} = \frac{N_{Trig|Sel}}{N_{Sel}}. \tag{5.14}$$

The aim of this method is to use this definition for the evaluation of the post-selection trigger efficiency for a specific trigger selection, in our case `L0Hadron_TOS`, using only quantities measurable from the data samples.

From Fig.5.16, assuming the statistical independence of the trigger selection categories, the following relation can be deduced

$$\epsilon_{TOS|Sel} = \frac{N_{TOS|Sel}}{N_{Sel}} = \frac{N_{TISTOS|Sel}}{N_{TIS|Sel}} \tag{5.15}$$

where $N_{TISTOS|Sel}$ refers to the number of events in the post-selection sample which satisfy both TIS and TOS requirements.

Hence, post-selection efficiency of `L0Hadron_TOS` $\epsilon^{\text{L0Hadron\_TOS}}$ trigger requirement can be

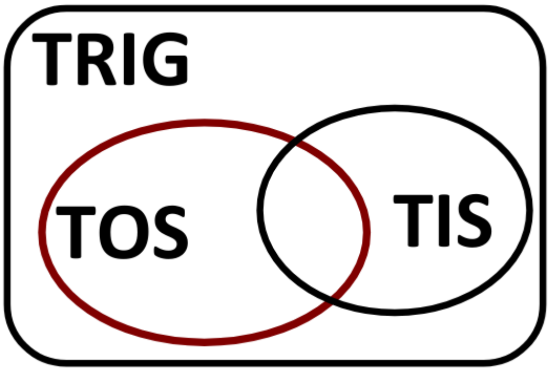

Figure 5.16 – Diagram of trigger categories. Figure taken from Ref. [51].

calculated as

$$\epsilon^{\text{L0Hadron\_TOS}} = \frac{\text{N}_{\text{L0Hadron\_TISTOS|Sel}}}{\text{N}_{\text{L0Hadron\_TIS|Sel}}}. \tag{5.16}$$

Correction factors calculation and results

The post-selection efficiencies are calculated using Equation 5.15 in MC simulated and LHCb measured samples resulting from two different selections in the normalisation mode. To be specific, the first selection is the nominal selection used in the analysis and the second selection is the alternative selection (leading to lower efficiencies) discussed in the Appendix A.1.

Efficiencies are calculated from the numbers of events established by the fits in normalisation mode $\Lambda_b^0 \to \Lambda K^+ K^-$ (see Section 5.7 for fit details) of the combined Run 2 data samples. The combined sample is used because it provides better statistical coverage than any yearly sample alone.

In case of simulated samples, efficiencies are calculated using weighted numbers of events in each trigger category. The weights account for yearly differences in recorded luminosity and differences in numbers of generated events in each simulated sample.

Table 5.15 summarises the efficiencies obtained using the TIS-TOS method applied on the samples of LHCb data and MC simulated samples. As can be seen, the ratios r are consistent in the nominal and alternative selections in both DD and LL track categories. Therefore, the correction factors can be assumed to cancel out at the measured precision in the efficiency ratio in Equation 5.13 and hence they do not play a role in the branching fraction measurement. Nevertheless, the systematic uncertainty on the L0 trigger efficiency is assigned in the Section 6.7.3.

Table 5.15 – Summary of post-selection efficiencies obtained using TISTOS method in the combined Run 2 LHCb data and MC samples, and their ratio r.

Selection	Sample	$\varepsilon_{Trig\|Sel}^{LHCb}$ [%]	$\varepsilon_{Trig\|Sel}^{MC}$ [%]	r
Nominal	DD	51.8 ± 3.9	63.5 ± 0.9	0.816 ± 0.004
Alternative	DD	53.3 ± 4.5	65.7 ± 0.9	0.811 ± 0.005
Nominal	LL	26.8 ± 2.8	39.8 ± 1.0	0.673 ± 0.005
Alternative	LL	24.6 ± 2.6	37.2 ± 0.8	0.661 ± 0.005

5.5.5 Offline selection efficiency

All values reported in the following subsections are based on truth-matched MC samples, as mentioned above.

Pre-selection efficiencies

After applying pre-selection requirements discussed in Section 5.3.4 on the events passing the trigger selection (after passing the reconstruction stage and the stripping selection), the pre-selection efficiencies reported in Table 5.16 are obtained. While signal efficiencies range between 83% to 90%, background selection efficiencies reach only values of ~50% removing nearly a half of the combinatorial background at this early selection stage.

Table 5.16 – List of pre-selection, MVA-selection and PID-selection efficiencies with corresponding binomial errors. As all samples are evaluated with the MVA classifiers trained on 2016 samples, minor differences in its performance are expected.

Mode	Track Cat	Year.	ε^{PreSel}[%]	ε^{MVA}[%]	ε^{PID}[%]
$\Lambda_b^0 \to \Lambda p\overline{p}$	DD	2015	88.58 ± 0.33	46.73 ± 0.54	66.43 ± 0.75
		2016	87.97 ± 0.19	43.29 ± 0.30	65.81 ± 0.44
		2017	88.32 ± 0.16	39.62 ± 0.26	63.85 ± 0.41
		2018	88.37 ± 0.17	40.11 ± 0.27	65.73 ± 0.42
$\Lambda_b^0 \to \Lambda K^+K^-$	DD	2015	89.32 ± 0.30	41.94 ± 0.50	55.74 ± 0.78
		2016	89.64 ± 0.18	38.52 ± 0.30	54.17 ± 0.5
		2017	89.92 ± 0.15	35.65 ± 0.25	61.19 ± 0.43
		2018	89.63 ± 0.16	35.42 ± 0.26	60.28 ± 0.45
$\Lambda_b^0 \to \Lambda p\overline{p}$	LL	2015	83.65 ± 0.69	76.12 ± 0.87	64.56 ± 1.12
		2016	84.45 ± 0.38	72.29 ± 0.51	63.81 ± 0.65
		2017	83.68 ± 0.34	68.62 ± 0.47	63.67 ± 0.59
		2018	84.22 ± 0.36	69.70 ± 0.49	64.61 ± 0.61
$\Lambda_b^0 \to \Lambda K^+K^-$	LL	2015	83.14 ± 0.63	69.48 ± 0.85	56.67 ± 1.09
		2016	84.88 ± 0.36	67.52 ± 0.51	55.92 ± 0.65
		2017	85.73 ± 0.30	66.15 ± 0.44	64.87 ± 0.54
		2018	85.28 ± 0.32	66.19 ± 0.46	63.97 ± 0.58

MVA selection efficiencies

Efficiencies of the MVA selection for the signal and normalisation samples are reported in Table 5.16. The different values of efficiencies between the track categories and between the studied channels are due to the different MVA requirements used in the selection. This is because they result from the respective optimisation procedures as detailed in Section 5.3.4. The reported efficiencies are obtained from events passing the pre-selection (also trigger and stripping and reconstruction).

PID efficiencies

The summary of PID efficiencies is provided in Table 5.16. These are calculated from the numbers of events passing the PID selection out of those which passed previous stages of the selection. As it was the case for MVA efficiencies, the PID efficiencies also have different values corresponding to different selection optimal points determined in Section 5.3.4. Note that the PID response in MC samples is corrected using the *PIDcorr* package (see Section 5.3.4) in order to ensure agreement between the *ProbNN* distributions in simulation and in data.

5.5.6 Efficiencies of applied vetoes

The efficiencies of the applied vetoes cannot be obtained directly from the simulation. This is because simulated distributions of variables describing the invariant mass of two-body subsystems used in the vetoes do not model the LHCb data correctly as discussed in beginning of Section 5.4. Therefore, the overall selection efficiency is determined from the corrected efficiencies in the bins of Squared Dalitz variables (see Section 5.5.7). Efficiencies of applied vetoes are unknown prior to the *unblinding* but they can be later determined from the overall selection efficiency and all previously discussed efficiencies obtained from the simulation.

5.5.7 Efficiencies in bins of Squared Dalitz variables

Each stage of the event selection has potentially an influence on the distribution of efficiencies over the phase-space. The average global efficiency depends on the phase-space positions of the observed signal events. Given that the signal has never been observed so far, the distribution of signal events in phase-space is unknown. However, upon a successful observation of a significant signal, a correction using the *sPlot* method [66] and *sWeight* can be applied. For the moment, the MC simulation samples are used to access the efficiency distribution in the phase-space. The bins of square Dalitz plot variables are used to describe it. To be specific, we use the normalised helicity θ'_{hh} and the normalised mass m'_{hh} between the two Λ_b^0-daughter charged hadrons (protons in the signal channel or kaons in the normalisation mode) following the definitions given in Section 5.2.2 (see Equations 5.3 and 5.5).

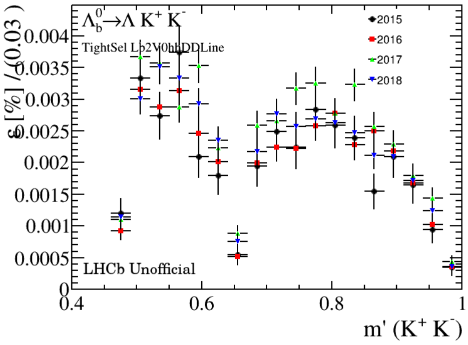

(a) DD sample for $\Lambda_b^0 \to \Lambda K^+ K^-$.

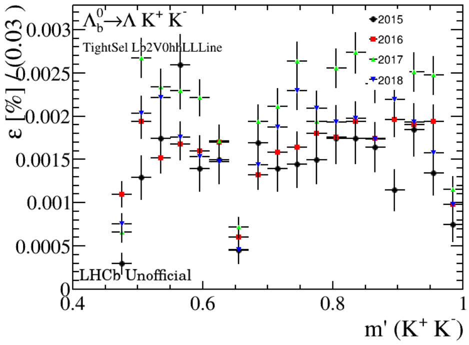

(b) LL sample for $\Lambda_b^0 \to \Lambda K^+ K^-$.

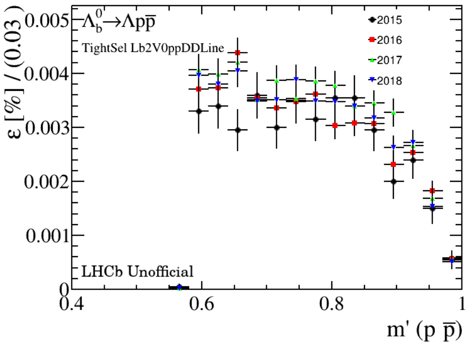

(c) DD sample for $\Lambda_b^0 \to \Lambda p\overline{p}$.

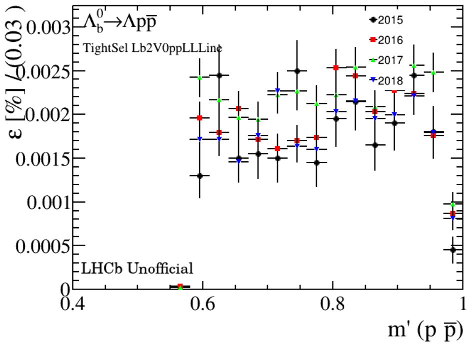

(d) LL sample for $\Lambda_b^0 \to \Lambda p\overline{p}$.

Figure 5.17 – Values of selection efficiencies (excluding generator level efficiencies) in bins of m'.

The distributions of selection efficiencies excluding generator level efficiencies in the bins of the squared Dalitz variables are reported in Fig. 5.17 for m' and in Fig. 5.18 for θ'_{hh}. Generator level efficiencies are excluded as they are constant in the bins of the squared Dalitz variables and they are introduced in the combined efficiency calculation separately (see Section 6.6.1). Note that certain intervals of m' are not fully shown because the content on the lower side of the spectrum is vetoed (see Section 5.3.5). Also, observed differences in efficiencies between the 2015-2016 and the 2017-2018 samples originate from differences in trigger efficiencies, as discussed in Section 5.5.3.

5.5.8 Simulation-based efficiency maps

Simulated samples are generated with uniform population in the plane defined by the squared Dalitz variables with known number of produced events (see Section 5.2.2). To determine the detection efficiency, we study the normalised distributions in this plane of simulated events passing the full selection.

Charm vetoes restrict us to the events with reconstructed invariant mass of two-body subsystem $m_{h\bar{h}} < 2.85\,\text{GeV}$ where $h\bar{h}$ represents a $p\overline{p}$ pair in the signal channel $\Lambda_b^0 \to \Lambda p\overline{p}$ and

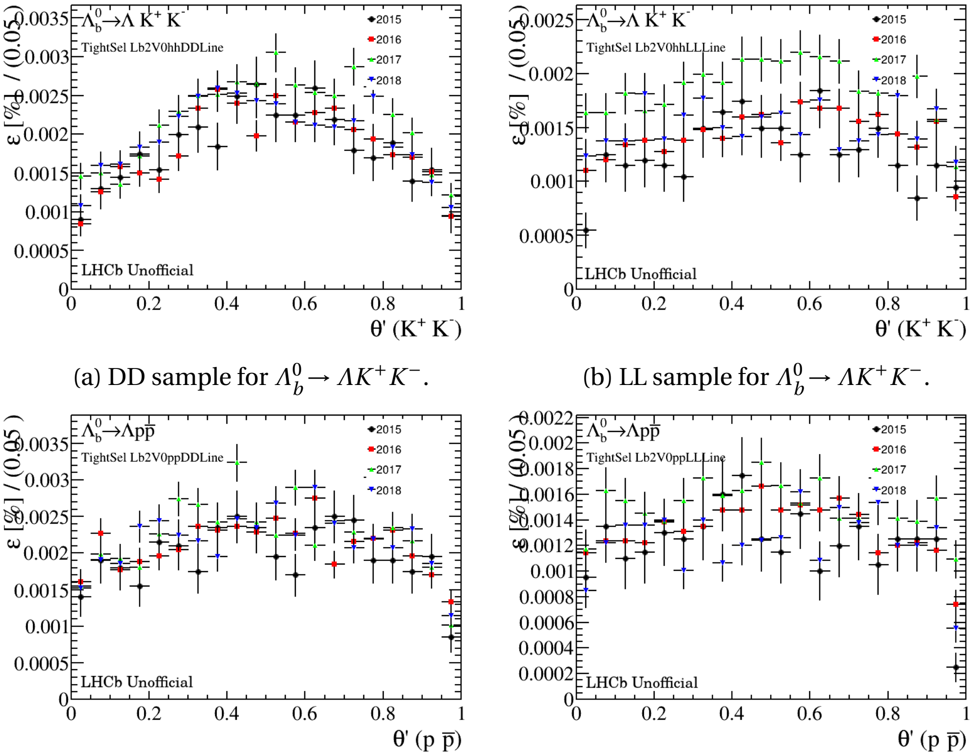

(a) DD sample for $\Lambda_b^0 \to \Lambda K^+ K^-$.

(b) LL sample for $\Lambda_b^0 \to \Lambda K^+ K^-$.

(c) DD sample for $\Lambda_b^0 \to \Lambda p\overline{p}$.

(d) Long track sample for $\Lambda_b^0 \to \Lambda p\overline{p}$.

Figure 5.18 – Values of selection efficiencies (excluding generator level efficiencies) in bins of θ'_{hh}.

a K^+K^- pair in the normalisation channel $\Lambda_b^0 \to \Lambda K^+ K^-$. Hence, the efficiency maps are reduced accordingly. Looking at Equation 5.3, which defines the square Dalitz mass m', we observe that it depends on invariant masses of the final state particles. Therefore, the requirement $m_{h\bar{h}} < 2.85\,\text{GeV}$ translates to $m'_{p\overline{p}} > 0.58$ in the signal mode and $m'_{K^+K^-} > 0.48$ in the normalisation mode. Examples of efficiency maps in the 2018 samples are provided in Fig. 5.19 and Fig. 5.20. Generator level efficiencies are not included in the maps as they are constant in all the square Dalitz bins and introduced in the combined efficiency calculation separately (see Section 6.6.1). As can be seen from these figures, the distributions in LL samples are closer to uniform distribution than in DD samples. This difference between DD and LL samples can be related to different selection requirement at stripping level and different MVA classifiers used for the two samples as discussed in Section 5.3.

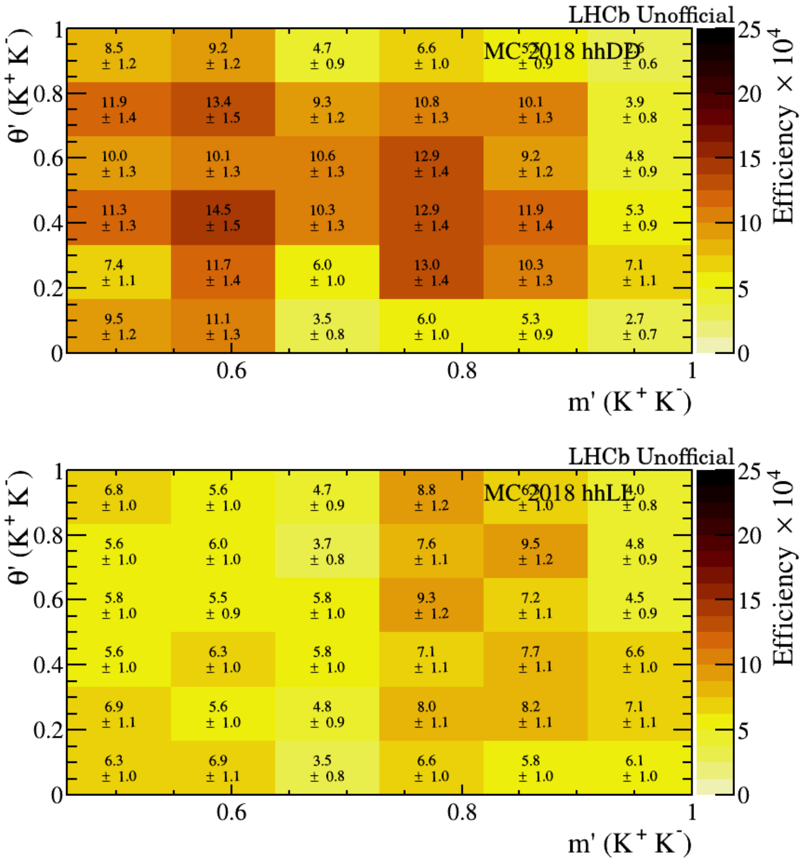

Figure 5.19 – Efficiency (excluding generator level efficiencies) maps in the 2018 $\Lambda_b^0 \to \Lambda K^+ K^-$ samples simulated uniformly in the square Dalitz plot plane. DD sample (top) and LL sample (bottom) are presented separately. The efficiencies are given in units of 10^{-4}.

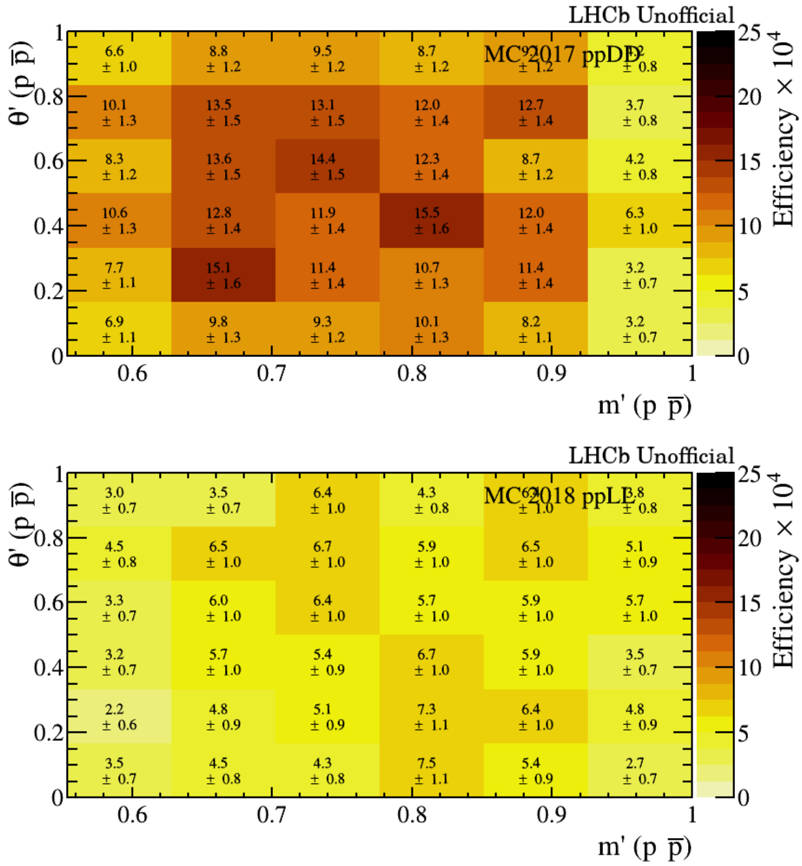

Figure 5.20 – Efficiency maps (excluding generator level efficiencies) in the 2018 $\Lambda_b^0 \to \Lambda p\overline{p}$ samples simulated uniformly in the square Dalitz plot plane. DD sample (top) and LL sample (bottom) are presented separately. The efficiencies are given in units of 10^{-4}.

5.6 Expected signal yields

$$Y_{DD}^{\Lambda_b^0} \approx 116$$

$$Y_{LL}^{\Lambda_b^0} \approx 88$$

Given the simulated samples describing the $\Xi_b^0 \to \Lambda p \overline{p}$ decay mode are not produced, its precise efficiency description is not available. Nevertheless, naive estimates can be made using aforementioned signal yields in the signal $\Lambda_b^0 \to \Lambda p \overline{p}$ channel the predicted branching fractions discussed in Section 2.2:

$$Y_{DD}^{\Xi_b^0} \approx 5$$

$$Y_{LL}^{\Xi_b^0} \approx 4$$

5.7 Fit model

Extended unbinned maximum likelihood fits are performed in order to measure the yields in the signal channel and also measure the branching fraction ratio between the signal $\Lambda_b^0 \to \Lambda p \overline{p}$ and normalisation $\Lambda_b^0 \to \Lambda K^+ K^-$ channels in a simultaneous fit to their respective samples. Two independent fits are performed for the DD and LL samples. For each track category the fit is run simultaneously over the 4 samples (years 2015-2018) in each of the normalisation mode and the signal mode.

5.7.1 Fit components and models

The mass spectrum of the normalisation channel comprises the following components:

- The signal decay $\Lambda_b^0 \to \Lambda K^+ K^-$ modelled by a double Crystal Ball (DCB) function (see details below).
- Partially reconstructed decays represented by the $\Lambda_b^0 \to \Sigma^0(\Lambda\gamma) K^+ K^-$ template illustrated in Fig. 5.15 (see Section 5.4.5).
- Combinatorial background represented by an exponential function (see Section 5.4).

The situation for the mass spectra of the signal channel is simpler given that the sample is clean. This is not only because there are fewer decay modes that can be found in the signal region, for example as partially reconstructed, but also thanks to the higher mass of the proton with respect to that of kaons:

- Decays of the signal $\Lambda_b^0 \to \Lambda p \overline{p}$ modelled by a DCB function (see details below).

- Decays of the signal $\Xi_b^0 \to \Lambda p\overline{p}$ modelled by a constrained DCB function (see Section 5.7.2).

- Combinatorial background represented by an exponential function (see Section 5.4).

It could be assumed that there is no signal in the $\Xi_b^0 \to \Lambda p\overline{p}$ mode considering predictions suggesting that it is beyond current LHCb reach. However, this mode is included in the signal channel fit for completeness.

Double Crystal Ball functions

The Crystal Ball function is defined as a central Gaussian function with a power-law tail:

$$\mathscr{C}(t; n, \alpha, \sigma) = \mathcal{N} \begin{cases} \exp\left(\frac{-t^2}{2\sigma^2}\right) & \text{if } t/\sigma > -\alpha \\ \left(\frac{n}{|\alpha|}\right)^n \left(\frac{n-\alpha^2}{|\alpha|} - \frac{t}{\sigma}\right)^{-n} \exp\left(-\alpha^2/2\right) & \text{if } t/\sigma \leq -\alpha \end{cases} \tag{5.17}$$

where $t = m - \mu$ is the reduced reconstructed mass, m is the reconstructed mass, μ and σ correspond to the central value and resolution of the Gaussian function, and $\mathcal{N}$ represents a normalisation factor. The tails modeled by a power-law function have a control parameter n. The sign of the α parameter implies the relative side with respect to the mean of the central Gaussian.

The *Double Crystal Ball function*[VI] is defined as the sum of two Crystal Ball functions with the same values for the core Gaussian mean and width. Generally, functions are summed with their normalisation coefficients. However, in case of two functions, one ratio $f_{\mathcal{N}} = \frac{\mathcal{N}_L}{\mathcal{N}_R}$ of Crystal Balls normalisations is sufficient to describe the situation instead of two normalisation parameters. Indices L and R are used to denote left and right Crystal Ball parts. DCB tails give freedom to account for detector effects such as resolution or in the case of the left tail also possible radiative contributions.

The used values of shape parameters of the DCB functions used in the fit are obtained from fits performed on MC simulated samples[VII] and they are considered constant. The summary of the obtained values is provided in Table 5.17.

Exponential function

Combinatorial background exponential function is defined as:

$$\mathscr{E}(m; p) = \mathcal{N} \exp(pm) \tag{5.18}$$

[VI] Note that there are high energy physics publications which use different (non-equivalent) definition for the term Double Crystal Ball function, this work follows the convention from the LHCb publication on the channel $\Lambda_b^0 \to \Lambda K^+ K^-$ [20].

[VII] Values determined from 2016 samples.

Table 5.17 – List of constant DCB parameters determined from MC samples. Errors are quoted for completeness and are not used in the final fit.

	$\Lambda_b^0 \to \Lambda K^+K^-$		$\Lambda_b^0 \to \Lambda p\overline{p}$	
Parameter	DD	LL	DD	LL
n_L	2.589 ± 0.303	2.487 ± 0.340	1.431 ± 0.192	1.858 ± 0.249
n_R	1.787 ± 0.280	1.945 ± 0.751	1.319 ± 0.145	1.502 ± 0.269
α_L	-1.999 ± 0.101	-2.009 ± 0.110	-2.213 ± 0.171	-1.960 ± 0.144
α_R	1.299 ± 0.334	0.826 ± 0.581	1.930 ± 0.144	1.577 ± 0.316
$f_{\mathcal{N}}$	0.231 ± 0.105	0.128 ± 0.082	0.509 ± 0.148	0.301 ± 0.147

where p is the *exponential parameter*, m is the reconstructed invariant mass and $\mathcal{N}$ is the normalisation factor.

5.7.2 Free parameters of the fit

In the discussion below, a single track category (LL or DD) is considered, and the corresponding superscript will be omitted.

Signal parametrisation

In principle one can measure directly yields in the normalisation channel for each year of data taking (N_{15}, N_{16}, N_{17} and N_{18}). Similarly, one can in each year of data taking directly measure the yields in the signal modes $\Lambda_b^0 \to \Lambda p\overline{p}$ ($N_{15}^{\Lambda_b^0}$, $N_{16}^{\Lambda_b^0}$, $N_{17}^{\Lambda_b^0}$ and $N_{18}^{\Lambda_b^0}$) and $\Xi_b^0 \to \Lambda p\overline{p}$ ($N_{15}^{\Xi_b^0}$, $N_{16}^{\Xi_b^0}$, $N_{17}^{\Xi_b^0}$ and $N_{18}^{\Xi_b^0}$).

More convenient parametrisation using ratios of branching fractions can be also used. In order to use this parametrisation, efficiencies in the signal channel $\Lambda_b^0 \to \Lambda p\overline{p}$ ($\Xi_b^0 \to \Lambda p\overline{p}$), $\epsilon_{S,i}$, and normalisation mode, ϵ_N, i are considered for each of the yearly samples (i=15,16,17,18).

The 12 measured parameters are chosen to be: 4 yields in the normalisation channel, N_i (i=15,16,17,18), 4 branching fraction ratios between $\Lambda_b^0 \to \Lambda p\overline{p}$ and $\Lambda_b^0 \to \Lambda K^+K^-$,

$$R_{\Lambda_b^0,i} = \frac{N_i^{\Lambda_b^0}}{N_i}\frac{\epsilon_{N,i}}{\epsilon_{S,i}} \quad (i = 15, 16, 17, 18) \tag{5.19}$$

and 4 ratios between $\Xi_b^0 \to \Lambda p\overline{p}$ and $\Lambda_b^0 \to \Lambda K^+K^-$,

$$R_{\Xi_b^0,i} = \frac{N_i^{\Xi_b^0}}{N_i}\frac{\epsilon_{N,i}}{\epsilon_{S,i}} \quad (i = 15, 16, 17, 18). \tag{5.20}$$

The equalities

$$R_{\Lambda_b^0,15} = R_{\Lambda_b^0,16} = R_{\Lambda_b^0,17} = R_{\Lambda_b^0,18} \qquad \equiv R_{\Lambda_b^0}, \tag{5.21}$$

and

$$R_{\Xi_b^0,15} = R_{\Xi_b^0,16} = R_{\Xi_b^0,17} = R_{\Xi_b^0,18} \qquad \equiv R_{\Xi_b^0}, \tag{5.22}$$

effectively impose three constraints for each of the signal channels and the number of free parameters is reduced from 12 to 6. Also, one can define the total yield N_{Tot} in the normalisation mode $\Lambda_b^0 \to \Lambda K^+ K^-$ as the sum of yields of the normalisation channel:

$$N_{Tot} \equiv N_{15} + N_{16} + N_{17} + N_{18}, \tag{5.23}$$

and the fraction of the normalisation yields in the year j (j=15,16,17):

$$f_{\mathrm{j}} \equiv \frac{N_j}{N_{Tot}} \tag{5.24}$$

So the 6 parameters of the signal parametrisation become:

- $R_{\Lambda_b^0}$, the ratio of the $\Lambda_b^0 \to \Lambda p\overline{p}$ branching fraction over the $\Lambda_b^0 \to \Lambda K^+ K^-$ branching fraction;
- $R_{\Xi_b^0}$, the ratio of the $\Xi_b^0 \to \Lambda p\overline{p}$ branching fraction over the $\Lambda_b^0 \to \Lambda K^+ K^-$ branching fractions;
- N_{Tot}, the sum of yields of the normalisation channel;
- 3 parameters f_j (j=15,16,17), the fractions of the normalisation yields in the year sample j;

The 12 yields are obtained from these 6 parameters, and from the efficiencies, as:

$$N_j = N \cdot f_j \quad (j = 15, 16, 17) \tag{5.25}$$

$$N_{18} = N \cdot (1 - f_{15} - f_{16} - f_{17}) \tag{5.26}$$

$$N_{\mathrm{j}}^{\Lambda_b^0} = R_{\Lambda_b^0} \cdot \frac{\epsilon_{\mathrm{S,j}}}{\epsilon_{N,j}} \cdot N \cdot f_j \quad (j = 15, 16, 17) \tag{5.27}$$

$$N_{18}^{\Lambda_b^0} = R_{\Lambda_b^0} \cdot \frac{\epsilon_{\mathrm{S18}}}{\epsilon_{N18}} \cdot N \cdot (1 - f_{15} - f_{16} - f_{17}) \tag{5.28}$$

Yields in the Ξ_b^0 mode are obtained analogously but using the same efficiency ratios as for the $\Lambda_b^0 \to \Lambda p\overline{p}$ given that the modes are very similar.

Background parameters

The following free parameters describe the background contribution:

- One parameter for the slope of the exponential describing the combinatorial background in each studied channel - one in signal and one in the normalisation spectra.
- Eight yearly yields in the combinatorial background, 4 for each channel.
- Four yearly yields in the misreconstruction physics background in the normalisation mode.

Additional fit constraints

The following constraints are required by the fit for each of the track categories:

- The exponential parameters describing the combinatorial backgrounds in the yearly samples of $\Lambda_b^0 \to \Lambda p\overline{p}$ mode are all set to be equal to each other. The same requirement is applied to the normalisation mode $\Lambda_b^0 \to \Lambda K^+K^-$. Therefore, only two exponential parameters (one for signal and one for normalisation mode) are used to describe all yearly samples.
- The mean values of the DCB function describing $\Lambda_b^0 \to \Lambda p\overline{p}$ mode and normalisation mode are set to be equal.
- The core width of the DCB function describing $\Lambda_b^0 \to \Lambda p\overline{p}$ mode is proportional to the width of the DCB function describing normalisation mode with proportion coefficient determined from simulation.
- The mean of the DCB function describing decays of $\Xi_b^0 \to \Lambda p\overline{p}$ is calculated as the mean value of $\Lambda_b^0 \to \Lambda p\overline{p}$ mode DCB function plus 174.9 MeV, the known mass difference between Ξ_b^0 and Λ_b^0, as obtained from the PDG [6].
- The width of the DCB function describing decays of $\Xi_b^0 \to \Lambda p\overline{p}$ is equal to the width of the DCB function describing $\Lambda_b^0 \to \Lambda p\overline{p}$ mode.

Summary of fit parameters

The model consists of 22 free parameters which are obtained from the simultaneous fit over yearly samples in the signal and normalisation mode (4+4 samples). These parameters are:

- 2 parameters for mean and width of DCB in function describing normalisation mode.
- 2 exponential parameters describing combinatorial background - one in the signal mode and one in the normalisation mode.

- 4 parameters for total number of events in the normalisation mode and yearly fractions in years 2015-2017.
- 4 yields of misreconstruction background in normalisation mode corresponding to data taking years.
- 4 yields in the combinatorial background in normalisation mode.
- 4 yields in combinatorial background in signal mode.
- 2 parameters describing branching fraction ratios – one between the channels $\Lambda_b^0 \to \Lambda p\overline{p}$ and $\Lambda_b^0 \to \Lambda K^+ K^-$ and the other between $\Xi_b^0 \to \Lambda p\overline{p}$ and $\Lambda_b^0 \to \Lambda K^+ K^-$.

5.7.3 Fit validation

In order to ensure that the fit reproduces the measurements as expected, so called *toy studies* are performed: 2000 sample sets, *toy samples*, are generated from the probability density functions of the fit components. Each sample set contains 4 yearly invariant mass distributions in the normalisation channel and 4 yearly invariant mass distributions in the signal channel. The fit is performed on each sample set in order to estimate how well it can determine the generated values of parameters in a given signal parameter regime (see below). For each of the free fit parameters the distributions of fit values, their errors and corresponding pull values[VIII] are constructed. A Gaussian fit is performed on each of these distributions.

Toy studies are performed in two signal regimes: Firstly, in the regime with yields in the signal channel $\Lambda_b^0 \to \Lambda p\overline{p}$ following the predictions from publications on *Purely baryonic decay processes* [8, 14] for which the expected branching fraction of $\Lambda_b^0 \to \Lambda p\overline{p}$ is calculated to be $(3.2^{+0.8}_{-0.3} \pm 0.4 \pm 0.7) \times 10^{-6}$, where the uncertainties are associated with non-factorisable effects, CKM matrix elements, and hadronic form factors, respectively (see Section 2.2). Studies are performed independently for DD and LL fits. In both of them, the selection efficiency ratio between the signal and normalisation modes are set to 1. However, based on naive estimates of this ratio, studies are performed with slightly different generated number of events in LL and DD. In the case of DD, a total number of signal events in the samples from all years is $N_{Sig}^{DD} = 116$ and in LL $N_{Sig}^{LL} = 121$ based on the yield estimates presented in Section 5.4 scaled by the luminosity and the early estimates of the charm veto efficiency. Corresponding generated branching fraction ratios are $R_S^{DD} = 0.37$ and $R_S^{LL} = 0.34$. Secondly, the scenario with no signal events is explored. In both scenarios, it is assumed that there is no signal in the decay $\Xi_b^0 \to \Lambda p\overline{p}$.

Results of key parameters in the fit stability tests with non-zero signal yields are reported in Figures 5.21 (DD) and 5.22 (LL) and a summary of the results is provided in Tables 5.18 and 5.19. Similarly, Figures 5.23 (DD) and 5.24 (LL) and Tables 5.20 and 5.21 provide the

[VIII] A pull value is calculated as a difference between the fitted and the generated value divided by the uncertainty of the fitted value.

overview of results on the fit stability without signal events. In all cases pull values must be viewed in the context of the reconstructed central values of the parameter and their errors in order to correctly interpret the possible biases. Due to poor statistics in the 2015 samples, larger deviations are expected. The toy studies are conducted again with the configuration corresponding to the actual measured values in the signal channels and a systematic uncertainty is assigned based on the observed residual biases.

Table 5.18 – Reduced summary of Gaussian parameters characterising the toy studies distributions with DD samples in the expected signal regime. The full summary table is provided in Appendix A.2.

	Generator	Values		Errors		Pulls	
		μ^{Gauss}	σ^{Gauss}	μ^{Gauss}	σ^{Gauss}	μ^{Gauss}	σ^{Gauss}
$\mu_{\Lambda_b^0}$	5619.2	5619.0	0.8924	0.8916	0.074	0.00	1.00
$\sigma_{\Lambda_b^0}$	13.53	13.53	0.8923	0.8824	0.093	-0.06	1.01
$N_{Tot}^{\Lambda_b^0\to\Lambda K^+K^-}$	314.86	315.30	23.18	23.130	0.753	-0.01	1.02
$f_{15}^{\Lambda_b^0\to\Lambda K^+K^-}$	0.0467	0.0471	0.0126	0.01234	0.00128	-0.06	1.04
$f_{16}^{\Lambda_b^0\to\Lambda K^+K^-}$	0.3085	0.3090	0.0274	0.02704	0.00119	0.01	1.02
$f_{17}^{\Lambda_b^0\to\Lambda K^+K^-}$	0.3251	0.3231	0.0279	0.02750	0.00118	-0.09	1.02
$R_{\Lambda_b^0}$	0.3671	0.3709	0.0491	0.0481	0.00513	-0.03	1.02
$R_{\Xi_b^0}$	0.0000	0.0001	0.0157	0.0152	0.00243	-0.13	1.08

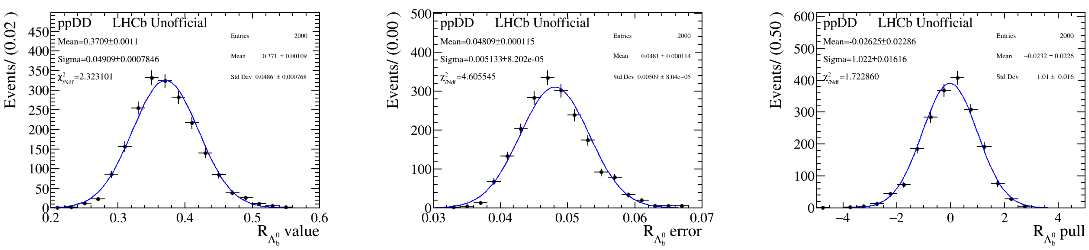

(a) $R_{\Lambda_b^0\to\Lambda p\overline{p}}$ values. (b) $R_{\Lambda_b^0\to\Lambda p\overline{p}}$ errors. (c) $R_{\Lambda_b^0\to\Lambda p\overline{p}}$ pulls.

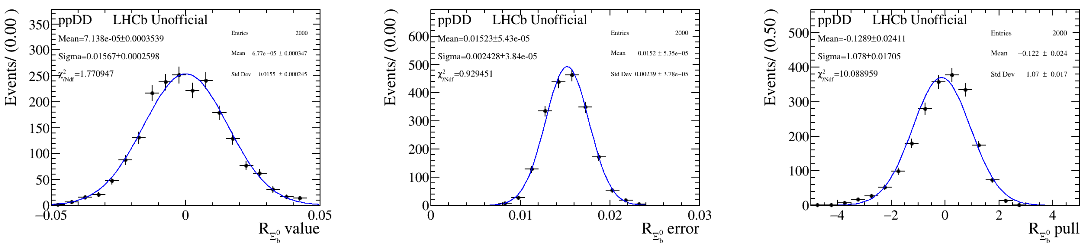

(d) $R_{\Xi_b^0\to\Lambda p\overline{p}}$ values. (e) $R_{\Xi_b^0\to\Lambda p\overline{p}}$ errors. (f) $R_{\Xi_b^0\to\Lambda p\overline{p}}$ pulls.

Figure 5.21 – Fit stability study in the DD samples in the expected signal regime.

Table 5.19 – Reduced summary of gaussian parameters characterising the toy studies distributions with LL samples in the expected signal regime. Full summary table is provided in Appendix A.2.

	Generator	Values		Errors		Pulls	
		μ^{Gauss}	σ^{Gauss}	μ^{Gauss}	σ^{Gauss}	μ^{Gauss}	σ^{Gauss}
$\mu_{\Lambda_b^0}$	5619.0	5619.0	0.8692	0.86	0.06	-0.01	1.00
$\sigma_{\Lambda_b^0}$	15.51	15.52	0.8039	0.78	0.06	-0.05	1.03
$N_{Tot}^{\Lambda_b^0 \to \Lambda K^+K^-}$	354.8	356.2	21.1300	21.02	0.568	0.04	1.01
$f_{15}^{\Lambda_b^0 \to \Lambda K^+K^-}$	0.070	0.074	0.0131	0.01	0.001	0.21	1.01
$f_{16}^{\Lambda_b^0 \to \Lambda K^+K^-}$	0.285	0.284	0.0226	0.02	0.001	-0.05	1.00
$f_{17}^{\Lambda_b^0 \to \Lambda K^+K^-}$	0.322	0.323	0.0244	0.02	0.001	-0.01	1.04
$R_{\Lambda_b^0}$	0.3420	0.3478	0.0401	0.0401	0.004	0.06	1.00
$R_{\Xi_b^0}$	0.0000	-0.0002	0.0105	0.0091	0.002	-0.17	1.14

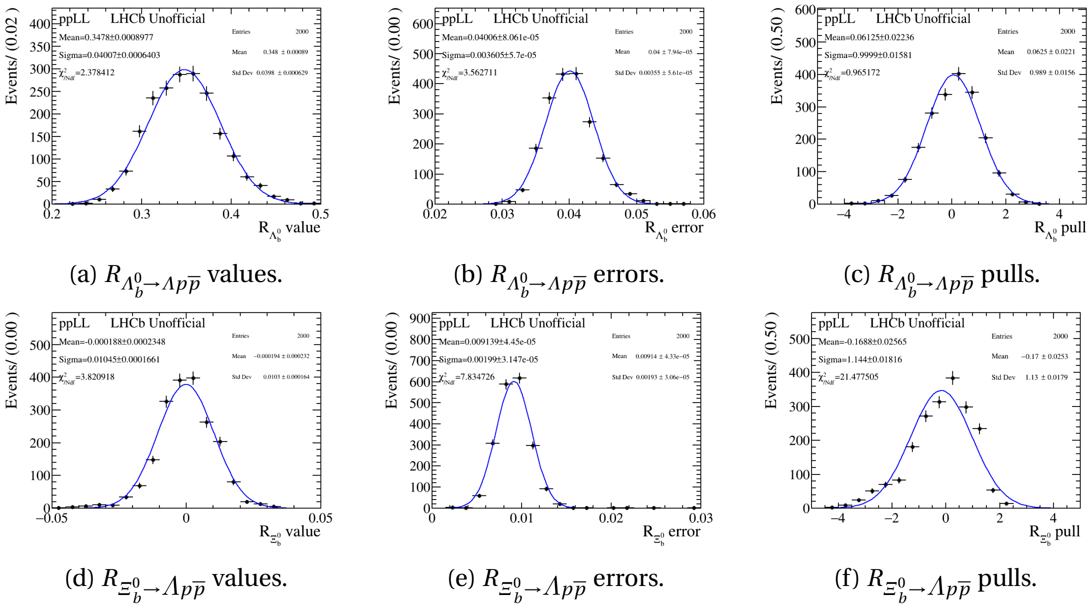

(a) $R_{\Lambda_b^0 \to \Lambda p\overline{p}}$ values. (b) $R_{\Lambda_b^0 \to \Lambda p\overline{p}}$ errors. (c) $R_{\Lambda_b^0 \to \Lambda p\overline{p}}$ pulls.

(d) $R_{\Xi_b^0 \to \Lambda p\overline{p}}$ values. (e) $R_{\Xi_b^0 \to \Lambda p\overline{p}}$ errors. (f) $R_{\Xi_b^0 \to \Lambda p\overline{p}}$ pulls.

Figure 5.22 – Fit stability study in the LL samples in the expected signal regime.

Table 5.20 – Reduced summary of Gaussian parameters characterising the toy studies distributions with DD samples in no signal regime. Full summary table is provided in Appendix A.2.

	Generator	Value		Errors		Pulls	
		μ^{Gauss}	σ^{Gauss}	μ^{Gauss}	σ^{Gauss}	μ^{Gauss}	σ^{Gauss}
$\mu_{\Lambda_b^0}$	5617.4	5617	1.19	1.16	0.116	0.05	1.04
$\sigma_{\Lambda_b^0}$	13.61	13.63	1.10	1.08	0.133	-0.08	1.03
$N_{Tot}^{\Lambda_b^0\to\Lambda K^+K^-}$	316.6	317.3	24.22	23.68	0.832	0.00	1.03
$f_{15}^{\Lambda_b^0\to\Lambda K^+K^-}$	0.03087	0.03038	0.01	0.01	0.002	-0.12	1.03
$f_{16}^{\Lambda_b^0\to\Lambda K^+K^-}$	0.3107	0.3094	0.03	0.03	0.002	-0.06	1.05
$f_{17}^{\Lambda_b^0\to\Lambda K^+K^-}$	0.3455	0.3458	0.03	0.03	0.002	-0.01	1.04
$R_{\Lambda_b^0}$	0.000000	-0.00034	0.02	0.02	0.002	-0.15	1.09
$R_{\Xi_b^0}$	0.000000	-0.000278	0.02	0.02	0.002	-0.16	1.12

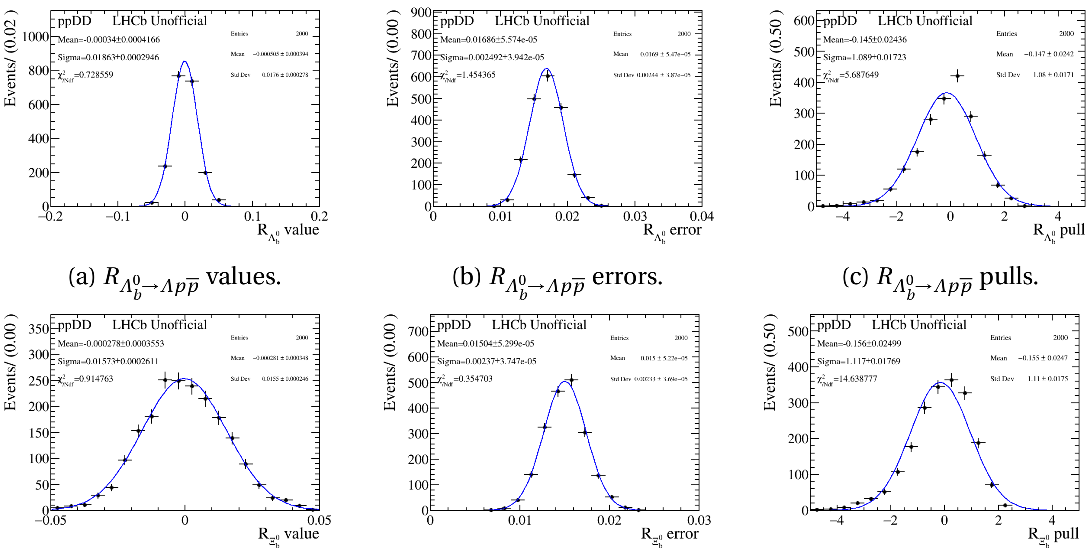

(a) $R_{\Lambda_b^0\to\Lambda p\overline{p}}$ values. (b) $R_{\Lambda_b^0\to\Lambda p\overline{p}}$ errors. (c) $R_{\Lambda_b^0\to\Lambda p\overline{p}}$ pulls.

(d) $R_{\Xi_b^0\to\Lambda p\overline{p}}$ values. (e) $R_{\Xi_b^0\to\Lambda p\overline{p}}$ errors. (f) $R_{\Xi_b^0\to\Lambda p\overline{p}}$ pulls.

Figure 5.23 – Fit stability study in the DD samples no signal regime.

Table 5.21 – Reduced of Gaussian parameters characterising the toy studies distributions with LL samples in no signal regime. Full summary table is provided in Appendix A.2.

	Generator	Values		Errors		Pulls	
		μ^{Gauss}	σ^{Gauss}	μ^{Gauss}	σ^{Gauss}	μ^{Gauss}	σ^{Gauss}
$\mu_{\Lambda_b^0}$	5618.5	5619	1.07	1.06	0.080	-0.01	1.03
$\sigma_{\Lambda_b^0}$	15.80	15.78	0.94	0.93	0.085	-0.07	1.03
$N_{Tot}^{\Lambda_b^0 \to \Lambda K^+ K^-}$	356.5	356.1	20.93	21.18	0.572	-0.03	1.01
$f_{15}^{\Lambda_b^0 \to \Lambda K^+ K^-}$	0.0552	0.0547	0.01	0.01	0.001	-0.14	1.05
$f_{16}^{\Lambda_b^0 \to \Lambda K^+ K^-}$	0.2858	0.2857	0.03	0.03	0.001	-0.03	1.02
$f_{17}^{\Lambda_b^0 \to \Lambda K^+ K^-}$	0.3253	0.3257	0.03	0.03	0.001	0.00	0.99
$R_{\Lambda_b^0}$	0.0000	0.00038	0.01	0.01	0.002	-0.09	1.08
$R_{\Xi_b^0}$	0.0000	-0.00044	0.01	0.01	0.002	-0.20	1.13

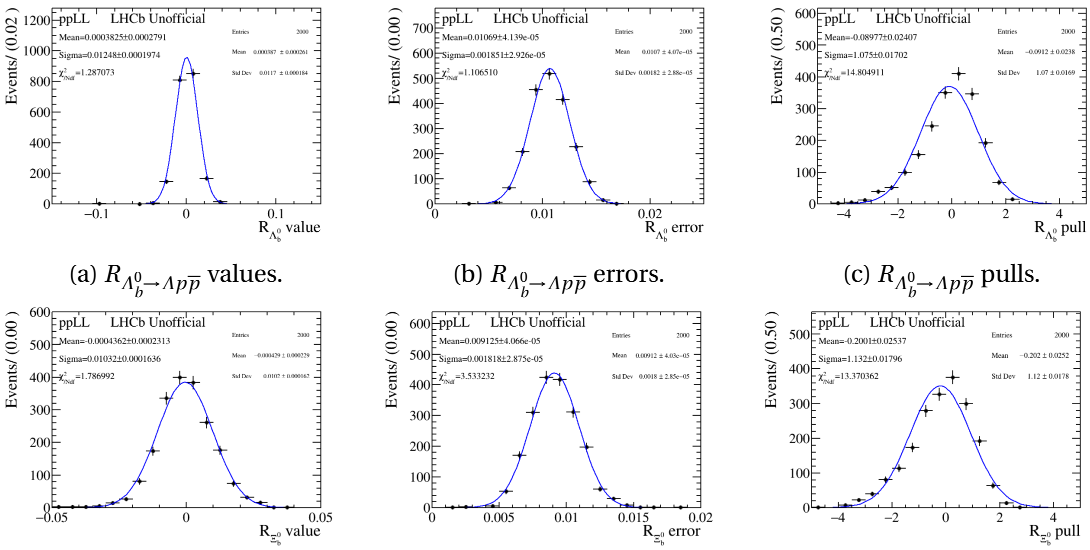

(a) $R_{\Lambda_b^0 \to \Lambda p\overline{p}}$ values. (b) $R_{\Lambda_b^0 \to \Lambda p\overline{p}}$ errors. (c) $R_{\Lambda_b^0 \to \Lambda p\overline{p}}$ pulls.

(d) $R_{\Xi_b^0 \to \Lambda p\overline{p}}$ values. (e) $R_{\Xi_b^0 \to \Lambda p\overline{p}}$ errors. (f) $R_{\Xi_b^0 \to \Lambda p\overline{p}}$ pulls.

Figure 5.24 – Fit stability study in the LL samples no signal regime: Parameters in the signal channel.

5.8 Blinded fit results

In order to demonstrate a good understanding of the normalisation channel $\Lambda_b^0 \to \Lambda K^+ K^-$, an invariant mass fit is performed on the $\Lambda K^+ K^-$ spectra.

5.8.1 Mass fit of the normalisation mode

The strategy of this fit is a simplified version of the one described in Section 5.7. To be specific, all parameters concerning the normalisation channel are as previously described and all the parameters for the signal channels are removed. Table 5.22 summarises the obtained values of the fit parameters. The parameters $N^{comb.,\Lambda K^+K^-}$ and $N^{misrec.}$ represent the yields in the combinatorial backgrounds and in the background originating from misreconstructed events, other parameters are defined in Section 5.7. Figures 5.25 and 5.26 show the projections of the simultaneous fit in each year of the normalisation channel data set. This check demonstrates the good fit quality of the normalisation channel, and shows that the normalisation yields are over 300 candidates for each DD and LL samples.

Table 5.22 – Results of the invariant mass fit of normalisation channel decays with the full selection and the vetoes applied. Note that $f_{18}^{\Lambda_b^0 \to \Lambda K^+ K^-}$ is calculated implicitly from Equation 5.23.

Parameter	DD Fit value	DD Fit error	LL Fit value	LL Fit error
$\mu_{\Lambda_b^0}$	5617.7	1.2	5618.8	1.1
$\sigma_{\Lambda_b^0}$	14.19	1.12	15.84	0.93
$p^{\Lambda K^+K^-}$	-0.00112	0.00022	-0.00262	0.00040
$N_{Tot}^{\Lambda_b^0 \to \Lambda K^+K^-}$	300.8	22.8	339.1	20.6
$f_{15}^{\Lambda_b^0 \to \Lambda K^+K^-}$	0.04	0.01	0.06	0.01
$f_{16}^{\Lambda_b^0 \to \Lambda K^+K^-}$	0.30	0.03	0.29	0.03
$f_{17}^{\Lambda_b^0 \to \Lambda K^+K^-}$	0.35	0.03	0.32	0.03
$N_{15}^{misrec.}$	8.9	6.9	2.1	4.7
$N_{16}^{misrec.}$	30.6	20.4	-3.1	15.0
$N_{17}^{misrec.}$	40.2	22.6	17.5	11.8
$N_{18}^{misrec.}$	17.4	22.1	-1.1	12.7
$N_{15}^{comb.,\Lambda K^+K^-}$	49.1	9.8	15.3	6.2
$N_{16}^{comb.,\Lambda K^+K^-}$	351.2	28.7	124.2	19.8
$N_{17}^{comb.,\Lambda K^+K^-}$	384.9	30.8	77.3	14.9
$N_{18}^{comb.,\Lambda K^+K^-}$	423.9	31.5	117.7	17.7

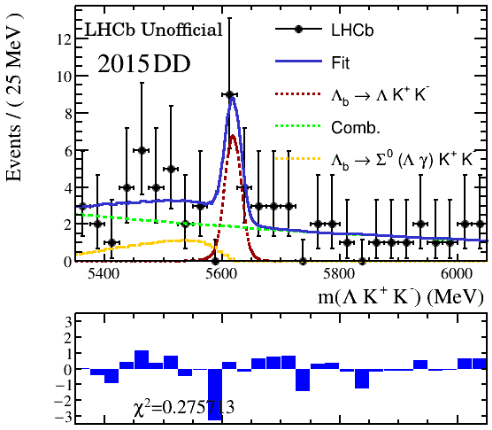

(a) 2015.

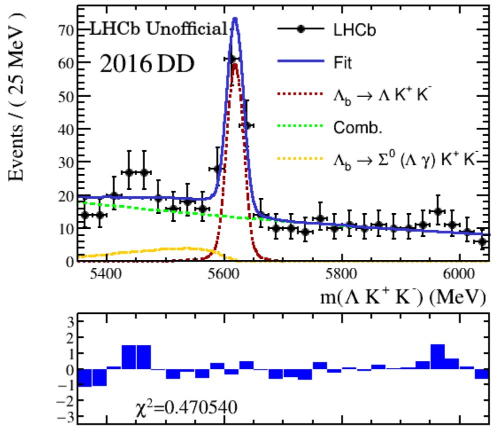

(b) 2016.

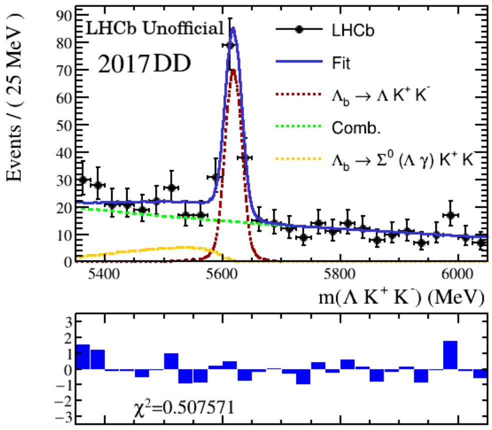

(c) 2017.

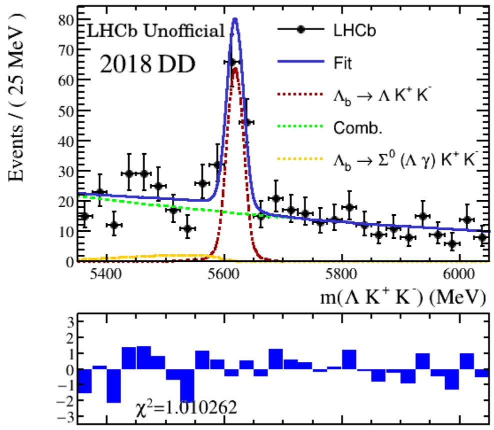

(d) 2018.

Figure 5.25 – Projection plots of normalisation yearly DD samples featuring LHCb data (black points) $\Lambda_b^0 \to \Lambda K^+ K^-$ contributions (brown line), $\Lambda_b^0 \to \Sigma^0 K^+ K^-$ contributions (yellow line), combinatorial background (green line), full fit model (blue line). The corresponding pull histogram is provided under each fit projection.

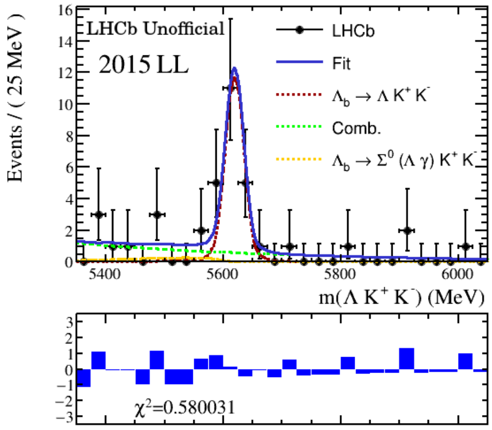

(a) 2015.

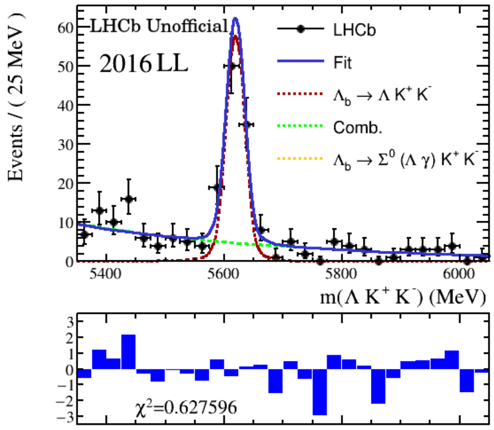

(b) 2016.

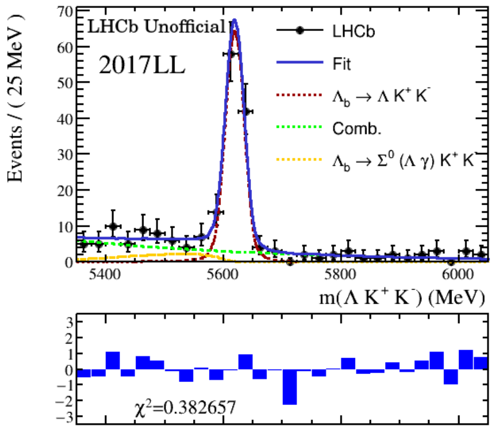

(c) 2017.

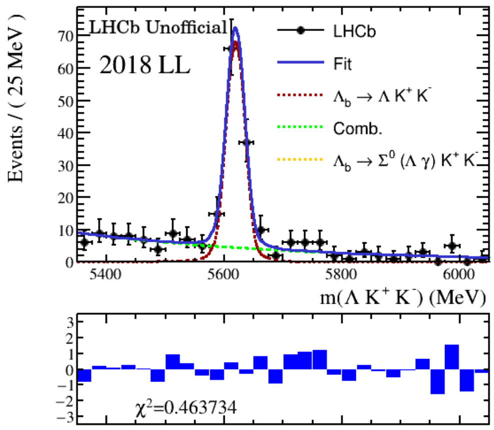

(d) 2018.

Figure 5.26 – Projection plots of normalisation yearly LL samples featuring LHCb data (black points) $\Lambda_b^0 \to \Lambda K^+ K^-$ contributions (brown line), $\Lambda_b^0 \to \Sigma^0 K^+ K^-$ contributions (yellow line), combinatorial background (green line), full fit model (blue line). The corresponding pull histogram is provided under each fit projection.

6 Results of the search for charmless purely baryonic processes

After validation of all the methods used, the blinded regions of the signal modes are *unblinded*. Testing of the signal hypotheses is performed in order to establish the significances of signal modes $\Lambda_b^0 \to \Lambda p\overline{p}$ and $\Xi_b^0 \to \Lambda p\overline{p}$, and the branching fractions are evaluated. In case of sufficient signal yield, the Dalitz distribution of the process is studied.

6.1 Signal hypotheses testing

For the purposes of signal hypothesis testing, the parametrisation of the fit model discussed in Section 5.7 is modified such that the six fit parameters describing the signal and normalisation yields (see section 5.7.2) are the total $\Lambda_b^0 \to \Lambda p\overline{p}$ yield, $Y^{\Lambda_b^0}$, the total $\Xi_b^0 \to \Lambda p\overline{p}$ yield, $Y^{\Xi_b^0}$, the normalisation yield, N_{Tot} (see Equation 5.23), and the yearly fractions, f_i (see Equation 5.24). Following the Equation 5.21 yearly fraction of the total yields in the signal modes are assumed to be identical to the fractions in the normalisation mode f_j (j=15,16,17).

After performing the final fit, the resulting parameter values are summarised in Table 6.1. Figures 6.1 and 6.2 show the projections of the simultaneous fit in each year of the signal channel data set. Projections in the normalisation channel are nearly identical to those already presented in Section 5.8. Combined projections of signal yearly samples are shown in Fig. 6.3. The total yields in the $\Lambda_b^0 \to \Lambda p\overline{p}$ channel are:

$$Y_{DD}^{\Lambda_b^0} = 20.3 \pm 7.7,$$

$$Y_{LL}^{\Lambda_b^0} = 19.0 \pm 5.9,$$

where DD and LL subscripts indicate the track category of the sample. Similarly in the $\Xi_b^0 \to \Lambda p\overline{p}$ channel:

$$Y^{\Xi_b^0} = 12.2 \pm 6.1,$$

$$Y^{\Xi_b^0} = 2.7 \pm 3.6.$$

Table 6.1 – Results of the simultaneous invariant mass fit of normalisation and signal channel samples. For parameter definitions see Sections 5.7 and 5.8.1.

Parameter	DD Fit value	DD Fit error	LL Fit value	LL Fit error
$\mu_{\Lambda_b^0}$	5617.3	1.19	5618.8	1.05
$\sigma_{\Lambda_b^0}$	14.241	1.11	15.65	0.905
$p^{\Lambda K^+K^-}$	-0.0011	0.0002	-0.0026	0.0003
$N_{Tot}^{\Lambda_b^0\to\Lambda K^+K^-}$	301.2	22.8	338.4	20.5
$f_{15}^{\Lambda_b^0\to\Lambda K^+K^-}$	0.033	0.0123	0.058	0.0138
$f_{16}^{\Lambda_b^0\to\Lambda K^+K^-}$	0.297	0.032	0.291	0.027
$f_{17}^{\Lambda_b^0\to\Lambda K^+K^-}$	0.335	0.033	0.308	0.027
$N_{15}^{misrec.}$	8.8	6.9	2.1	4.74
$N_{16}^{misrec.}$	29.7	20.4	-2.9	14.90
$N_{17}^{misrec.}$	39.0	22.6	17.6	11.9
$N_{18}^{misrec.}$	16.6	22.0	-1.0	12.7
$N_{15}^{comb.,\Lambda K^+K^-}$	49.6	9.9	15.3	6.2
$N_{16}^{comb.,\Lambda K^+K^-}$	351.9	28.7	123.9	19.7
$N_{17}^{comb.,\Lambda K^+K^-}$	387.4	30.9	78.0	15.0
$N_{18}^{comb.,\Lambda K^+K^-}$	422.9	31.4	117.5	17.7
$N_{15}^{comb.,\Lambda p\overline{p}}$	15.5	4.0	14.7	4.0
$N_{16}^{comb.,\Lambda p\overline{p}}$	106.2	10.8	43.3	6.9
$N_{17}^{comb.,\Lambda p\overline{p}}$	115.9	11.1	39.4	6.5
$N_{18}^{comb.,\Lambda p\overline{p}}$	174.0	14.0	45.9	7.3
$p^{\Lambda p\overline{p}}$	-0.0016	0.0003	-0.0021	0.0004
$Y^{\Xi_b^0}$	**12.19**	6.11	**2.68**	3.61
$Y^{\Lambda_b^0}$	**20.26**	7.74	**19.03**	5.88

6.2 Statistical significance of the observation of the signal channels

In order to measure the global statistical significance of the observation of the signal channels $\Lambda_b^0 \to \Lambda p\overline{p}$ and $\Xi_b^0 \to \Lambda p\overline{p}$, the fit is modified to be applied simultaneously to the DD and LL samples. This modification is implemented by a change of parametrisation introducing sums S and differences D in yields

$$S^{\Lambda_b^0} = Y_{LL}^{\Lambda_b^0} + Y_{DD}^{\Lambda_b^0} \tag{6.1}$$

$$D^{\Lambda_b^0} = Y_{LL}^{\Lambda_b^0} - Y_{DD}^{\Lambda_b^0} \tag{6.2}$$

$$S^{\Xi_b^0} = Y_{LL}^{\Xi_b^0} + Y_{DD}^{\Xi_b^0} \tag{6.3}$$

$$D^{\Xi_b^0} = Y_{LL}^{\Xi_b^0} - Y_{DD}^{\Xi_b^0} \tag{6.4}$$

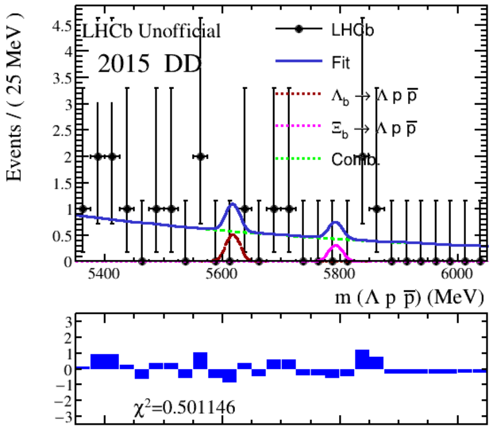

(a) 2015.

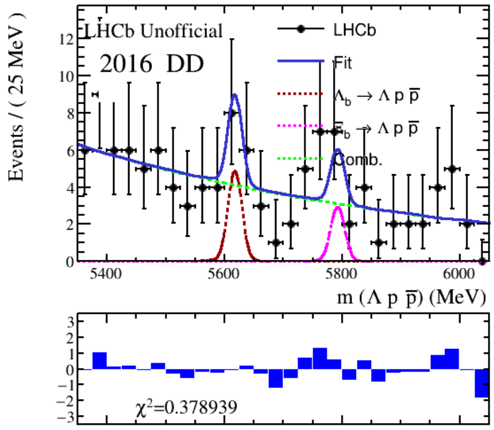

(b) 2016.

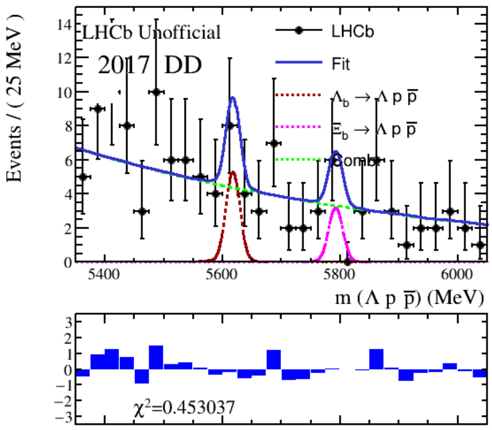

(c) 2017.

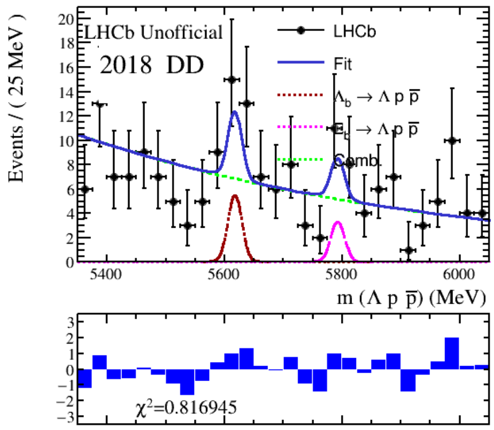

(d) 2018.

Figure 6.1 – Projection plots of signal yearly DD samples featuring LHCb data (black points) $\Lambda_b^0 \to \Lambda p\overline{p}$ contributions (brown line), $\Xi_b^0 \to \Lambda p\overline{p}$ contributions (pink line), combinatorial background (green line), full fit model (blue line). The corresponding pull histogram is provided under each fit projection.

The statistical significance is determined using hypothesis testing where we consider two hypotheses [64, 65]:

- *Null* hypothesis: the signal does not exist and the data can be described without any signal contribution. This corresponds to the value zero of $S^{\Lambda_b^0}$ parameter in the fit (zero signal contribution).
- *Signal* hypothesis: the signal contribution is included in the data description. The S parameter has a value of its *maximum likelihood estimate*, $S_{fit}^{\Lambda_b^0}$, which corresponds to the value of maximal likelihood obtained from the fit. Following the fit results (see Table 6.1) and Equation 6.1, we observe $S_{fit}^{\Lambda_b^0} = 39.29$.

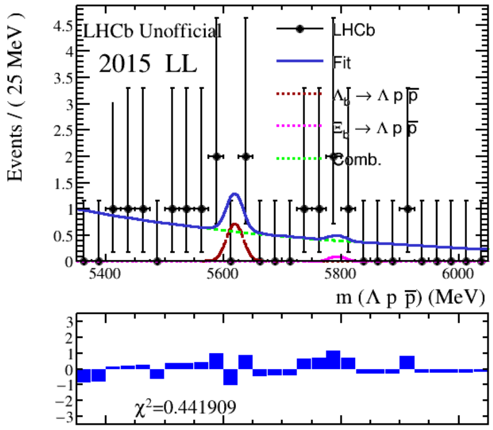

(a) 2015.

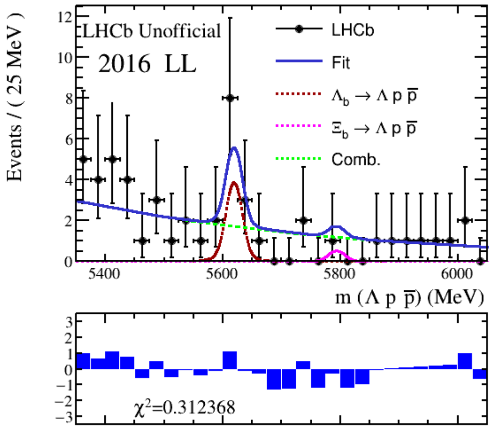

(b) 2016.

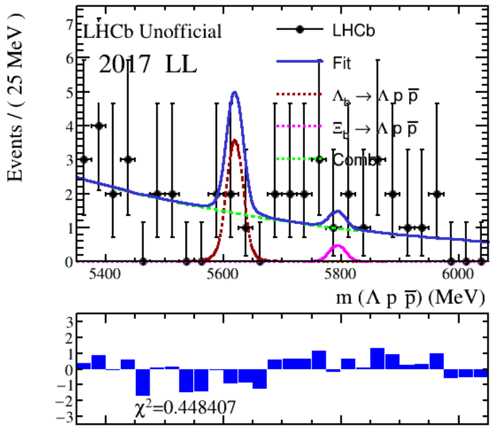

(c) 2017.

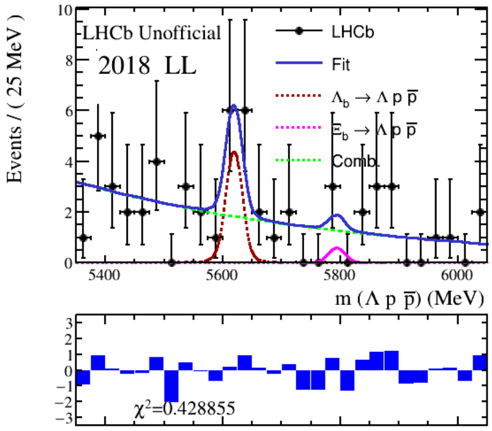

(d) 2018.

Figure 6.2 – Projection plots of signal yearly LL samples featuring LHCb data (black points) $\Lambda_b^0 \to \Lambda p\overline{p}$ contributions (brown line), $\Xi_b^0 \to \Lambda p\overline{p}$ contributions (pink line), combinatorial background (green line), full fit model (blue line). The corresponding pull histogram is provided under each fit projection.

If we let $\mathscr{L}(H)$ denote the likelihood of hypothesis H, then the statistical significance $\chi_{\Lambda_b^0}$, in terms of standard deviations σ is calculated as follows, excluding the systematic uncertainties:

$$\chi_{\Lambda_b^0} = \sqrt{2 \cdot \left(\ln \mathscr{L}(S^{\Lambda_b^0} = S_{fit}^{\Lambda_b^0}) - \ln \mathscr{L}(S^{\Lambda_b^0} = 0) \right)} \sigma. \tag{6.5}$$

The statistical significance of $\Xi_b^0 \to \Lambda p\overline{p}$, $\chi_{\Xi_b^0}$, is calculated analogously. The resulting statistical significance on the $\Lambda_b^0 \to \Lambda p\overline{p}$ decay contribution is found to be:

$$\chi_{\Lambda_b^0} = 4.9\,\sigma,$$

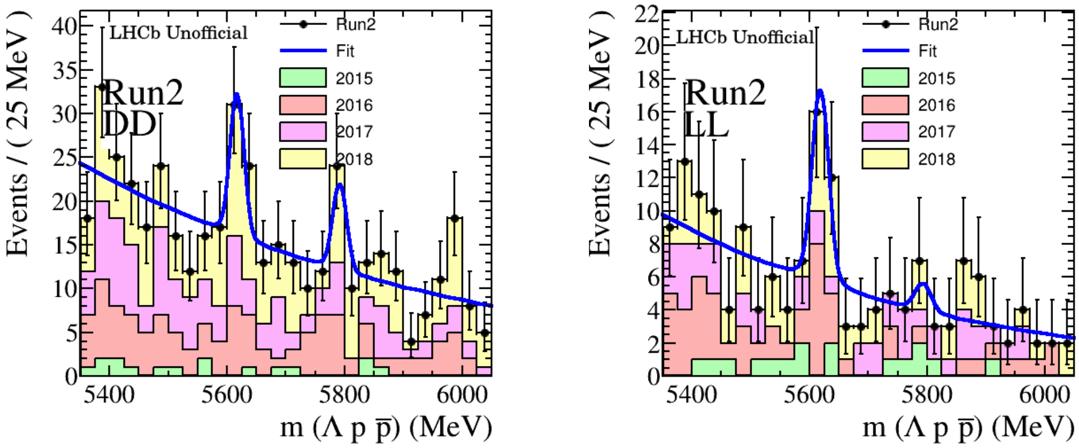

(a) DD samples.

(b) LL samples.

Figure 6.3 – Invariant mass fit of decays reconstructed in the signal channel with full selection and vetoes applied with all yearly samples.

and in case of $\Xi_b^0 \to \Lambda p\overline{p}$ channel it is found to be:

$$\chi_{\Xi_b^0} = 2.4\,\sigma.$$

6.3 Sources of significance related systematic uncertainties

Systematic uncertainties are all uncertainties that are not directly due to the statistics of the data [65]. Sources of these systematic uncertainties relevant for significance determination are presented in this section. Establishing and propagating systematic uncertainties is essential for determining the combined uncertainty and correct significance calculation (see Section 6.4).

6.3.1 Signal model

A systematic uncertainty associated with the choice of the model for the signal distributions is considered.

An alternative signal model is is studied. In this model, two-sided Hypathia functions [67] are used to describe the signals in the normalisation $\Lambda_b^0 \to \Lambda K^+ K^-$ and signal $\Lambda_b^0 \to \Lambda p\overline{p}$ and $\Xi_b^0 \to \Lambda p\overline{p}$ channels. Same as for the nominal signal model, only the central value of the invariant mass μ and the distribution width σ are free nuisance parameters in the fit. All other nuisance parameters of the Hypathia functions are determined from the simulation.

The resulting values of the combined yields S are compared with those measured by the nominal fit. The systematic uncertainty associated with the signal model is assigned to be the absolute value of the difference between the measured combined yields values in nominal and the alternative signal model fit configurations. The obtained uncertainties are

$$\Delta S^{\Lambda_b^0}_{sig.model} = 0.56,$$

and

$$\Delta S^{\Xi_b^0}_{sig.model} = 0.96.$$

6.3.2 Combinatorial background model

The choice of the model for the combinatorial background comes also with a systematic uncertainty on it. The second-order Chebychev polynomials are used to describe the background in the full model and the fit results are compared with the nominal fit. To be specific, the combined yields $S^{\Lambda_b^0}$ and $S^{\Xi_b^0}$ measured using the model with Chebychev polynomials are compared with the combined yields $S^{\Lambda_b^0}$ and $S^{\Xi_b^0}$ in the nominal configuration. The absolute value of the difference between the two measured combined yields values is the systematic uncertainty associated with the combinatorial background model. The obtained values are

$$\Delta S^{\Lambda_b^0}_{bkg.model} = 1.50,$$

and

$$\Delta S^{\Xi_b^0}_{bkg.model} = 1.35.$$

6.3.3 Common parameter of the combinatorial background model

In the nominal fit model, the exponential parameters $p^{\Lambda p\overline{p}}$ and $p^{\Lambda K^+K^-}$ describing the slope of the combinatorial background are assumed to be identical in all years of data taking. The systematic uncertainty associated with this assumption is evaluated as follows: Firstly, we allow for different yearly values $p_i^{\Lambda K^+K^-}$ (i=15,16,17,18) of the exponential parameters in the fit of the normalisation channel (signals are not fitted at this stage). We define them using scaling parameters b_i (i=15,16,17,18) which express ratios of slopes in the given year sample with respect to the slope in the 2018 sample ($b_{18} \equiv 1$)

$$p_i^{\Lambda K^+K^-} = p_{18}^{\Lambda K^+K^-} \cdot b_i \quad (i = 15, 16, 17, 18) \tag{6.6}$$

After performing the fit in the normalisation mode $\Lambda_b^0 \to \Lambda K^+K^-$, the values of slope-scaling parameters b_i (i=15,16,17,18) are found and summarised in Table 6.2.

In the second step, the fit over the normalisation and signal samples is performed in the following configuration: The slope scaling parameters b_i (i=15,16,17,18) in the normalisation channel are set to the constants stated in Table 6.2. While certain parameter values differ from the nominal value (-0.0011 ± 0.0002 in DD and -0.0026 ± 0.0003 in LL) by up to $\sim 45\%$, the impact on the exponential function in the studied region is minimal. The yearly slopes

Table 6.2 – The values of the slope-scaling parameters b_i (i=15,16,17,18).

Parameter	DD sample	LL sample
b_{15}	0.6542	0.518
b_{16}	0.5480	1.379
b_{17}	1.4317	0.552
b_{18}	1.000	1.000

$p_i^{\Lambda p\overline{p}}$ (i=15,16,17,18) in signal mode spectra $p^{\Lambda p\overline{p}}$ are required to scale with the same slope scaling parameters as in the normalisation mode.

$$p_i^{\Lambda p\overline{p}} = p_{18}^{\Lambda p\overline{p}} \cdot b_i \quad (i = 15, 16, 17, 18). \tag{6.7}$$

The resulting combined fit yields S are compared with the yields in the nominal fit configuration with the shared combinatorial background slope parameters. Absolute values of the difference between the two resulting yields are considered as systematic uncertainties and measured to be

$$\Delta S^{\Lambda_b^0}_{common.par} = 0.32,$$

and

$$\Delta S^{\Xi_b^0}_{common.par} = 0.95.$$

6.3.4 Fit biases

In order to estimate the systematic uncertainty associated with the fit biases, another instance of toy studies (see Section 5.7.3) is evaluated with 2000 toy samples. Samples are produced with the generator values of S_{Gen} parameters set to

$$S^{\Lambda_b^0}_{Gen} = 39.28,$$

and

$$S^{\Xi_b^0}_{Gen} = 14.87.$$

The fit is performed on each toy sample and the mean fitted values in toys are found to be:

$$S^{\Lambda_b^0}_{ToyMean} = 39.14 \pm 0.22,$$

and

$$S^{\Xi_b^0}_{ToyMean} = 14.89 \pm 0.16.$$

We define fit bias $\delta S^{\Lambda_b^0}$ in the signal channel $\Lambda_b^0 \to \Lambda p\overline{p}$ as

$$\delta S^{\Lambda_b^0} = S_{Gen}^{\Lambda_b^0} - S_{ToyMean}^{\Lambda_b^0} \tag{6.8}$$

and fit bias $\delta S^{\Xi_b^0}$ in $\Xi_b^0 \to \Lambda p\overline{p}$ signal channel is defined analogously. These definitions lead to the following resulting biases:

$$\delta S^{\Lambda_b^0} = -0.14 \pm 0.22$$

and

$$\delta S^{\Xi_b^0} = 0.02 \pm 0.16$$

The systematic uncertainty on fit biases is considered to be dependent both on the bias value and its uncertainty, which are added in quadrature:

$$\Delta S_{bias}^{\Lambda_b^0} = 0.26,$$

and

$$\Delta S_{bias}^{\Xi_b^0} = 0.17.$$

6.3.5 Background from falsely reconstructed Λ

A systematic uncertainty associated with so far unobserved [6] $\Lambda_b^0 \to p\overline{p}p\pi^-$ decays potentially contributing to the $\Lambda_b^0 \to \Lambda p\overline{p}$ spectra is considered negligible for the following reasons. Firstly, this missidentification cannot happen in the DD sample as $p\pi^-$ pair creates tracks in the VELO if it originates from a Λ_b^0 baryon. Secondly, following the studies with simulated signal events it is estimated that only ≈ 3% of signal-like events could pass the vertex separation requirement imposed in Section 5.3.4. Furthermore, candidates from $\Lambda_b^0 \to p\overline{p}p\pi^-$ would suffer from low efficiency from the another requirement imposed in Section 5.3.4: $p\pi^-$ system to be consistent with Λ baryon which is unlikely if $p\pi^-$ pair does not originate from Λ.

6.3.6 Combined systematic uncertainties

The standard error propagation method [61] is used to combine systematic uncertainties discussed in the previous sections. Table 6.3 provides an overview of estimated systematic uncertainties and their combined values. We obtain the combined systematic uncertainties on the yields equal to 1.65 events in the $\Lambda_b^0 \to \Lambda p\overline{p}$ channel and 1.91 events in the $\Xi_b^0 \to \Lambda p\overline{p}$ channel.

6.4 Significance calculation with systematical uncertainties

In order to calculate the significance of the measured signals, we take into account the statistical and systematic uncertainties.

Table 6.3 – Overview of estimated systematic uncertainties on combined yields S .

Source systematic uncertainty	$\Delta S^{\Lambda_b^0}$	$\Delta S^{\Xi_b^0}$
Signal model	0.56	0.96
Combinatorial background model	1.50	1.35
Common combinatorial parameters	0.32	0.95
Fit biases	0.26	0.17
Combined systematic uncertainty	1.65	1.91

In addition to the definitions from Section 6.2, we also consider the relations of Gaussian-distributed observable x and its maximum likelihood estimate x_0

$$\chi^2_{stat.}(x) = \frac{(x - x_0)}{\sigma^2_{stat.}}, \tag{6.9}$$

$$\chi^2_{sys.}(x) = \frac{(x - x_0)}{\sigma^2_{sys.}}, \tag{6.10}$$

and for the resulting combined distribution

$$\chi^2_{Tot.}(x) = \frac{(x - x_0)}{\sigma^2_{Tot.}}. \tag{6.11}$$

Now we consider the standard error propagation

$$\sigma^2_{Tot.} = \sigma^2_{stat.} + \sigma^2_{sys.}, \tag{6.12}$$

which, with Equations 6.9, 6.10 and 6.11, implies

$$\frac{1}{\chi^2_{Tot.}(x)} = \frac{1}{\chi^2_{stat.}(x)} + \frac{1}{\chi^2_{sys.}(x)}. \tag{6.13}$$

Therefore, the resulting distribution for $\chi^2_{Tot.}(x)$ is

$$\chi^2_{Tot.}(x) = \frac{\chi^2_{stat.}(x)}{1 + \chi^2_{stat.}(x)\frac{\sigma^2_{sys.}}{(x-x_0)^2}}, \tag{6.14}$$

which is used to determine the significance with systematic uncertainties.

In our case, the observable is S, its maximum likelihood estimate is S_{fit} and we test against

$S = 0$, therefore the significance is finally estimated as

$$\chi^2_{Tot.} \equiv \chi^2_{Tot.}(0) = \frac{\chi^2_{stat.}(0)}{1 + \chi^2_{stat.}(0)\frac{\sigma^2_{sys.}}{(0-S_{fit})^2}}. \tag{6.15}$$

If we take values of S parameters based on yields reported in Section 6.1, the values of significance reported in Section 6.2 and values of combined systematic uncertainties from Section 6.3.6, we can evaluate the values of total significance of studied channels with Equation 6.15. Resulting values are:

$$\chi^{\Lambda^0_b}_{Tot.} = 4.8\sigma$$

and

$$\chi^{\Xi^0_b}_{Tot.} = 2.3\sigma.$$

The resulting values imply evidence for the observation of the $\Lambda^0_b \to \Lambda p\overline{p}$ signal channel. Therefore, this mode is studied further to determine its branching fraction and invariant mass distributions of its two-body sub-systems. On the other hand, resulting values are compatible with non-observation of the $\Xi^0_b \to \Lambda p\overline{p}$ signal mode within the available statistics. Therefore, this mode is not studied further.

6.5 Background-subtracted Dalitz plots

Due to the low statistics in the signal mode $\Lambda^0_b \to \Lambda p\overline{p}$, no firm conclusions on the invariant masses of the two-body subsystems can be made. Nevertheless, combined Run 2 background-subtracted, so called *sWeighted*, Dalitz distributions without efficiency corrections are provided in Fig. 6.4. The corresponding one-dimensional invariant mass distributions are shown in Fig. 6.5. Looking at Fig. 6.5, only speculations can be made about the agreement with the theoretical predictions for mass distributions of two-body sub-systems presented in Fig. 2.3. The projections in the LL sample appear compatible with a $p\overline{p}$ threshold enhancement, with large masses for the Λp system, and intermediate masses for the $\Lambda\overline{p}$. Although not inconsistent, the DD sample does not strongly support these conclusions. While these observations are promising to contradict the theoretical prediction, the low statistics of the signal does not allow to conclude unambiguously on the existence of a threshold enhancement for this decay.

6.6 Signal efficiency determination

In order to measure the branching fraction ratio between the signal channel $\Lambda^0_b \to \Lambda p\overline{p}$ and the normalisation channel $\Lambda^0_b \to \Lambda K^+K^-$, it is necessary to determine the corresponding detection ratio of efficiencies. As the signal chanel $\Lambda^0_b \to \Lambda p\overline{p}$ suffers from low statistics, it is

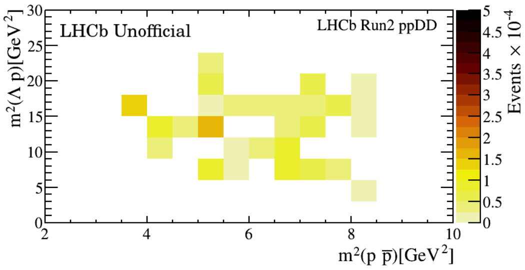

(a) $p\overline{p}$ and Λp subsystem, DD sample.

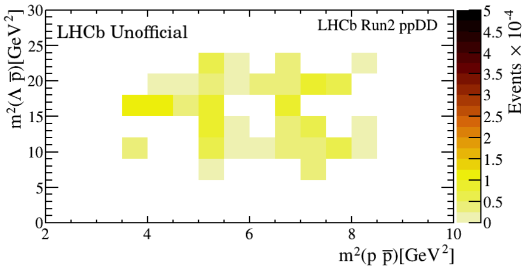

(b) $p\overline{p}$ and $\Lambda\overline{p}$ subsystem, DD sample.

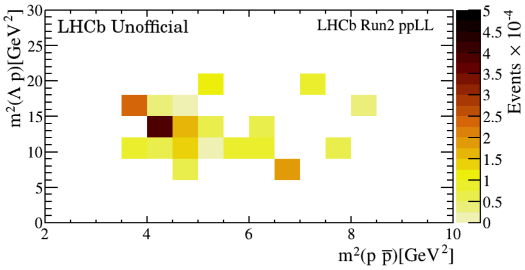

(c) $p\overline{p}$ and Λp subsystem, LL sample.

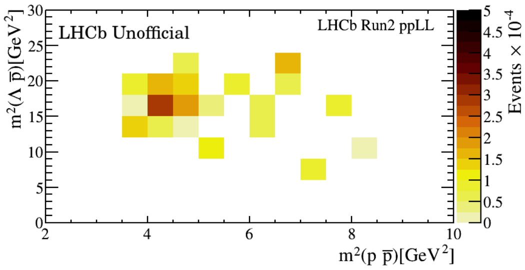

(d) $p\overline{p}$ and $\Lambda\overline{p}$ subsystem, LL sample.

Figure 6.4 – sWeighted Dalitz plots of $\Lambda_b^0 \to \Lambda p\overline{p}$ decays. The plot show (left) $m^2(\Lambda p)$ versus $m^2(p\overline{p})$, and (right) $m^2(\Lambda\overline{p})$ versus $m^2(p\overline{p})$, for the (top) DD and (bottom) LL samples.

not possible to properly determine yearly efficiencies. Instead, a combined *global* efficiency is calculated per channel and per track category taking. Global efficiencies are calculated based on simulated efficiency maps described by squared Dalitz variables (see Section 5.2.2) and weighted distributions of measured events. The event weights, so called *sWeights* are determined by the fit using *sPlot* method with the reconstructed Λ_b^0 invariant mass distributions as discriminating variable [66].

6.6.1 Combined efficiency calculation

In order to calculate the global efficiencies, we firstly assume that all the decays take place inside the detector and account for those which do not later on. To begin with, the signal sWeighted distribution is projected into the bins established in the simulated efficiency maps (see Section 5.5.8). Firstly, we consider sWeighted yield N_i in the bin i. We can calculate this sWeighted yield N_i as

$$N_i = \sum_{j}^{N_{i,bintotal}} w_{ij}, \tag{6.16}$$

where w_{ij} is the weight of event j inside bin i and $N_{i,bintotal}$ is the total number of events in the bin i.

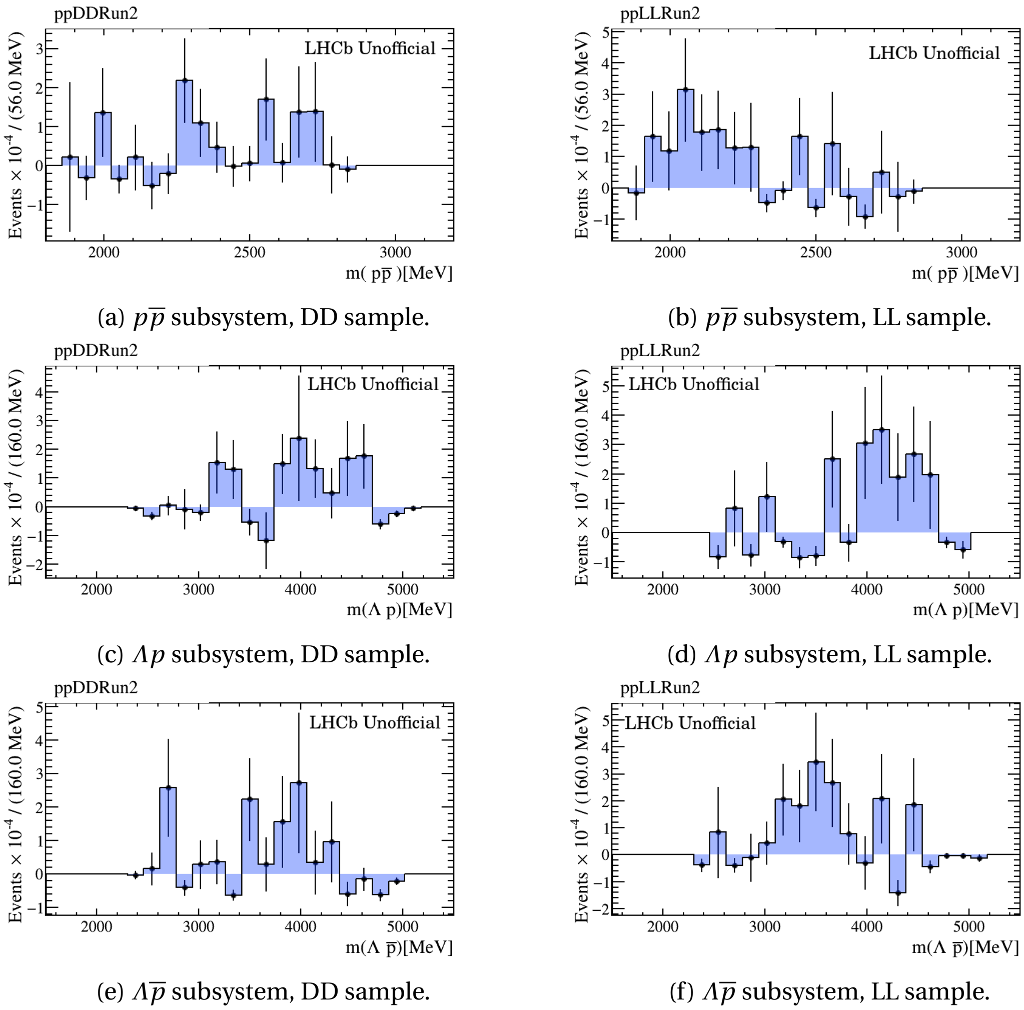

(a) $p\overline{p}$ subsystem, DD sample. (b) $p\overline{p}$ subsystem, LL sample.

(c) Λp subsystem, DD sample. (d) Λp subsystem, LL sample.

(e) $\Lambda\overline{p}$ subsystem, DD sample. (f) $\Lambda\overline{p}$ subsystem, LL sample.

Figure 6.5 – Distributions of invariant mass of two-body sub-systems showing DD (left) and LL samples (right) in the signal channel $\Lambda_b^0 \to \Lambda p\overline{p}$.

Secondly, we define the relation between sWeights and the total signal yield Y

$$\sum_{i}^{N_{bins}} N_i = \sum_{i}^{N_{bins}} \sum_{j}^{N_{i,bintotal}} w_{ij} = Y. \tag{6.17}$$

Thirdly, we calculate the *real* number of events in bin i, N_i^R which must have occurred in the detector in order to measure the observed number in the bin given the detection efficiency ϵ_i obtained from the simulated efficiency maps

$$N_i^R = \frac{N_i}{\epsilon_i}. \tag{6.18}$$

Naturally, this idea can be up-scaled to calculate the *ideal* yield Y^{ideal} which we would have obtained with an ideal detector with detection efficiency equal to 100%

$$Y^{ideal} = \sum_{i}^{N_{bins}} N_i^R. \tag{6.19}$$

We can now define the global efficiency ϵ_G as

$$\epsilon_G = \frac{Y}{Y^{ideal}} = \frac{Y}{\sum_i^{N_{bins}} \frac{N_i}{\epsilon_i}}. \tag{6.20}$$

As the efficiencies ϵ_i determined from simulation suffer from uncertainties $\Delta\epsilon_i$ as indicated in the efficiency maps (see Section 5.5.8) we use standard error propagation to calculate the uncertainty on the global efficiency $\Delta\epsilon_G$

$$\Delta\epsilon_G = \frac{\epsilon_G^2}{Y}\sqrt{\sum_{i}^{N_{bins}} \frac{N_i^2}{\epsilon_i^4}(\Delta\epsilon_i)^2}. \tag{6.21}$$

Combining yearly efficiencies

Given the low signal yield values it is not possible to determine the yearly efficiencies separately using the method above. Therefore, we perform a global efficiency calculation over all years as

$$\epsilon_G^{Run2} = \frac{\sum_{Q=15}^{18} Y^Q}{\sum_{Q=15}^{18}\sum_i^{N_{bins}} \frac{N_i^Q}{\epsilon_i^Q}}, \tag{6.22}$$

where index Q indicates that each of the previously defined quantities takes value from sample year Q of data taking or the corresponding efficiency map. The uncertainty is calculated analogously.

6.6.2 Combined efficiencies

Global efficiencies are calculated separately in DD and LL samples both for the signal mode $\Lambda_b^0 \to \Lambda p\overline{p}$ and the normalisation mode $\Lambda_b^0 \to \Lambda K^+K^-$. Results of the global efficiency calculation are summarised in Table 6.4.

Looking at Table 6.4 we can finally calculate efficiency ratios needed for the relative branching fraction measurements (see Section 5.7)

$$\frac{\epsilon_N}{\epsilon_S} = \frac{\epsilon_G^{Run2}(\Lambda_b^0 \to \Lambda K^+K^-)}{\epsilon_G^{Run2}(\Lambda_b^0 \to \Lambda p\overline{p})}. \tag{6.23}$$

Table 6.4 – Results of global efficiency calculation, in units of 10^{-4}.

Mode	Track Category	$\epsilon_G^{Run2} \times 10^4$	$\Delta\epsilon_G^{Run2} \times 10^4$	$\Delta\epsilon_G^{Run2}/\epsilon_G^{Run2}$
$\Lambda_b^0 \to \Lambda p\overline{p}$	DD	10.22	0.65	0.06
$\Lambda_b^0 \to \Lambda K^+K^-$	DD	7.81	0.27	0.03
$\Lambda_b^0 \to \Lambda p\overline{p}$	LL	6.63	0.46	0.07
$\Lambda_b^0 \to \Lambda K^+K^-$	LL	6.77	0.14	0.02

So far we assumed that all the decays take place inside the detector. To account for those which do not, we introduce the ratio of generator level efficiencies ϵ^{Gen} which are directly related to the detector geometrical acceptance to Equation 6.23

$$\frac{\epsilon_N}{\epsilon_S} = \frac{\epsilon_G^{Run2}(\Lambda_b^0 \to \Lambda K^+K^-)}{\epsilon_G^{Run2}(\Lambda_b^0 \to \Lambda p\overline{p})} \frac{\epsilon_N^{\text{Gen}}}{\epsilon_S^{\text{Gen}}}. \tag{6.24}$$

From values presented in Table 5.12 we obtain

$$\frac{\epsilon_N^{\text{Gen}}}{\epsilon_S^{\text{Gen}}} = 0.941 \pm 0.001.$$

Finally, the resulting values are, in the DD sample:

$$\frac{\epsilon_N^{DD}}{\epsilon_S^{DD}} = 0.72 \pm 0.06,$$

and in the LL sample:

$$\frac{\epsilon_N^{LL}}{\epsilon_S^{LL}} = 0.96 \pm 0.07.$$

6.7 Branching-fraction related systematic uncertainties

Systematic uncertainties on the measured branching fraction are yet to be determined. Therefore, they are not included in the reported results with the exception of the uncertainty on the branching fraction of the normalisation mode, which is propagated to the absolute branching fraction.

Systematic uncertainties are divided into three categories and their evaluation is discussed in the sections below:

- Uncertainty on the branching fraction of the normalisation mode
- Efficiency-independent uncertainties
- Efficiency-related uncertainties

6.7.1 $\Lambda_b^0 \to \Lambda K^+ K^-$ branching fraction

The branching fraction of the normalisation mode has been measured to be

$$\mathscr{B} = (15.9 \pm 2.6) \times 10^{-6}$$

with the Run I data sample [20].The first quoted uncertainty is statistical, the second is systematical and the last quoted uncertainty is due to the precision with which the normalisation channel branching fraction is known. Its uncertainty is taken as a systematic uncertainty on the ratio of branching fractions as given in Equation 5.2.

6.7.2 Efficiency-independent uncertainties

These uncertainties are currently work-in-progress for the LHCb publication that will be published after this thesis. They are to be determined using the nominal fit model with the branching fraction ratio considering the same sources of uncertainty and evaluation methods as discussed in Section 6.3.

6.7.3 Efficiency-related uncertainties

Examples of considered efficiency-related uncertainties are listed below:

L0 efficiency correction

Comparison of the ratios listed in the Table 5.15 can be used to estimate a preliminary systematic uncertainty on the L0 trigger efficiency. For the LL case, the nominal ratio is 0.67 and the alternative ratio is 0.66. These values differ by 1.8% (0.67/0.66 = 1.02), which is taken as systematic uncertainty. Similarly, for the DD case, the nominal ratio is 0.82 and the alternative ratio is 0.81. These values differ by 0.6%, which is taken as systematic uncertainty.

Ratio of corrected tracking efficiencies

Tracking efficiencies entering the ratio calculation may suffer from the systematic uncertainty on hadron tracking efficiencies due to different material interactions.

Uncertainty associated with the ratio of corrected tracking efficiencies is to be estimated from differences between protons and kaons interactions with detector materials. They are simulated by GEANT4 platform [37] and uncertainties on material composition of the detector, so called *material budget* [68].

PID selection efficiency

The systematic uncertainty is to be evaluated based on 3 potential sources [69] related to use of PIDCorr package:

- Number of events simulated calibration samples.
- Parametrisation of weighted PID control samples
- Subtraction of background from PID control samples using sWeights.

6.8 Measured branching fraction

The efficiency ratios established in the Section 6.6.2 are used as constants in the fit model defined in Section 5.7 and the fit is used to measure relative branching fraction $R^{\Lambda_b^0}$.

Firstly, the relative branching fraction is measured independently in the DD and LL categories and then simultaneously over the two categories linked only by the value of $R^{\Lambda_b^0}$ parameter. The measured values are summarised in Table 6.5.

Table 6.5 – Summary of measured relative branching fraction.

Track Category	$R^{\Lambda_b^0} \times 100$
DD	4.80 ± 1.86
LL	5.40 ± 1.70
Combined	**5.14** ± 1.25

Now we consider the previously measured branching fraction in the normalisation mode:

$$\mathscr{B}(\Lambda_b^0 \to \Lambda K^+ K^-) = (15.9 \pm 1.2 \pm 1.2 \pm 2.0) \cdot 10^{-6} = (15.9 \pm 2.6) \cdot 10^{-6}.$$

As this value is measured without the full set of charm vetoes deployed in this analysis the absolute branching fraction of $\Lambda_b^0 \to \Lambda p\overline{p}$ signal mode using the branching fraction $\mathscr{B}(\Lambda_b^0 \to \Lambda K^+ K^-)$ may be potentially biased. Nevertheless, if we assume that charm contributions to this branching fraction are not significant, we calculate the preliminary estimate of the absolute branching fraction of $\Lambda_b^0 \to \Lambda p\overline{p}$ signal mode:

$$\mathscr{B}(\Lambda_b^0 \to \Lambda p\overline{p}) = (0.82 \pm 0.20_{(stat.)} \pm 0.13_{(norm)}) \cdot 10^{-6} = (0.82 \pm 0.24) \cdot 10^{-6},$$

where the first uncertainty is statistical associated with $R^{\Lambda_b^0}$ and the second is associated with the uncertainty on the branching fraction of the normalisation mode $\Lambda_b^0 \to \Lambda K^+ K^-$. Systematical uncertainties are yet to be included in this branching fraction measurement once they are determined (currently work-in-progress, see Section 6.7).

Now we look at the theoretical prediction $\mathscr{B}(\Lambda_b^0 \to \Lambda p\overline{p}) = 3.2^{+1.1}_{-0.9}$ (see Section 2.2). Assuming Gaussian uncertainties, we conclude that the measured and predicted branching fraction are consistent at the 3.5σ level, where the uncertainties on the measurement are statistical only.

7 Conclusions and outlook

Predictions of the Standard Model, the theory which dominates the field of particle physics, have motivated many of the experimental searches and measurements carried out over the last few decades. Nowadays, it is known that the Standard Model alone is not sufficient to fully describe the properties of all elementary particles. Operation of the LHC and its experiments during the last decade in particular led to a broad range of new results and observations. While the vast majority of them is in agreement with the predictions, there are some which indicate discrepancies and, therefore, possibly lead to discovery of physics beyond the Standard Model. In addition, there are many results of measurements involving rare decay channels which are inconclusive due to low statistical precision. Nevertheless, searching for these rare channels is crucial to further test and constrain the Standard Model.

Following the strong need for better statistical precision, the detectors at the LHC are being, or will be, upgraded in order to profit from the upcoming years of operations of the LHC. Notably, the LHCb detector at CERN is currently undergoing a major upgrade with several sub-detectors being replaced. One of them is the Scintillating Fibre (SciFi) tracker. As its technology is not commercially available it is build by the LHCb collaboration. A crucial part of its construction is the production of hundreds of scintillating fibre arrays. It is managed by production centres hosted by selected universities, including EPFL. The complete SciFi sub-detector is currently being installed in the experiment hall of the LHCb detector.

The main focus in this thesis is the first search for charmless purely baryonic decays, processes that are theoretically predicted yet never experimentally observed. Following, the theoretical estimates indicating that the LHCb experiment is currently the only existing experiment capable of detecting these rare process, two signal decay channels are studied: $\Lambda_b^0 \to \Lambda p \overline{p}$ and $\Xi_b^0 \to \Lambda p \overline{p}$.

As these channels have so far not been observed, a blind analysis is performed. This implies that measurement techniques for searches in these rare channels are established and extensively validated using the simulations and the normalisation mode $\Lambda_b^0 \to \Lambda K^+ K^-$ before they are applied on the studied signal channels.

After the validation of all techniques involved, the measurements are carried out. The significance of existence of the $\Lambda_b^0 \to \Lambda p \overline{p}$ signal channel is found to be 4.8 σ including systematic uncertainties, constituting the first evidence for this channel, only slightly below the threshold set at 5.0σ for an unambiguous discovery. In the case of the $\Xi_b^0 \to \Lambda p\overline{p}$ channel, the measured significance is 2.3σ, which is compatible with the non observation of this channel with the present level of statistics.

Consequently, the measurement of the relative branching fraction, $R^{\Lambda_b^0}$ between the signal mode $\Lambda_b^0 \to \Lambda p\overline{p}$ and the normalisation mode $\Lambda_b^0 \to \Lambda K^+K^-$ is performed. The resulting value is

$$R^{\Lambda_b^0} = (5.14 \pm 1.25) \times 10^{-2}.$$

The indicated uncertainty is statistical only. This value can be used to calculate the absolute branching fraction of the signal mode $\Lambda_b^0 \to \Lambda p\overline{p}$. Currently, the only reported value of absolute branching fraction of the normalisation mode $\Lambda_b^0 \to \Lambda K^+K^-$ is measured without the full set of charm vetoes deployed in this analysis. If one assumes that charm contributions are negligible, the following absolute branching fraction is obtained:

$$\mathscr{B}(\Lambda_b^0 \to \Lambda p\overline{p}) = (0.82 \pm 0.20_{(stat.)} \pm 0.13_{(norm)}) \cdot 10^{-6},$$

where the first uncertainty is statistical associated with $R^{\Lambda_b^0}$, the second is associated with the uncertainty on the branching fraction of the normalisation mode $\Lambda_b^0 \to \Lambda K^+K^-$. The systematic uncertainty is yet to be evaluated.

We can compare the measured branching fraction with the theoretical prediction:

$$\mathscr{B}(\Lambda_b^0 \to \Lambda p\overline{p}) = (3.2^{+0.8}_{-0.3} \pm 0.4 \pm 0.7) \times 10^{-6},$$

where the uncertainties are associated with non-factorisable effects, CKM matrix elements, and hadronic form factors, respectively. Assuming Gaussian uncertainties, we conclude that the measured and predicted branching fraction are consistent at the 3.5σ level, where the uncertainties on the measurement are statistical only.

Also, non-observation of the $\Xi_b^0 \to \Lambda p\overline{p}$ decay mode is in agreement with the theoretical expectations at the current sensitivity. Dalitz plots of the $\Lambda_b^0 \to \Lambda p\overline{p}$ decays are also studied. However, given the low signal yield, the distributions are inconclusive.

The presented results of studies on the rare $\Lambda_b^0 \to \Lambda p\overline{p}$ decays using the LHCb detector suffer from low statistics. As the significance of the $\Lambda_b^0 \to \Lambda p\overline{p}$ signal channel is so close to the discovery threshold even minor improvements in signal statistics may lead to reaching this threshold. The signal statistics may be increased in two ways: Firstly, one can consider to reduce the conventional charm veto restricting us to the region $m_{h\bar{h}} < 2.85$ GeV. This way, we can include the region of $m_{p\overline{p}} > 3.75$ GeV where we do not expect peaking features in the signal mode given the region is above the $D\bar{D}$ meson pair production threshold. Secondly, this analysis may be extended to include the Run 1 samples and, therefore, increase overall number of analysed events. In both scenarios, the expected increase of the signal $\Lambda_b^0 \to \Lambda p\overline{p}$ events is sufficient reach the discovery threshold.

Furthermore, future updates using the data collected with the upgraded LHCb detector during the LHC Run 3 (2022-2024) and beyond will increase the statistics and resulting precision significantly. Following the early estimates, the number of the signal events in the $\Lambda_b^0 \to \Lambda p \overline{p}$ channel is expected to reach 300. Once this data will be available, it will be possible to perform CP-violation measurements and a detailed Dalitz plot analysis which may help to understand the underlying mechanism of formation of the two-body baryonic subsystems given both measurements are in the reach of the upgraded LHCb detector.

A Appendix

A.1 Alternative optimisation of the combined MVA-PID selection

As an alternative to the optimisation procedure described in Section 5.3, the following optimisation is considered in the normalisation channel: Instead of simulation optimisation of S_{MVA} and S_{PID} values, only one-dimensional optimisation using Punzi figure of merit with the value of S_{MVA} requirement set to a constant is used. The value of this constant is set to be equal to the optimal value of S_{MVA} identified in the signal mode. This could be potentially beneficial to reduce further the difference between the selection in the signal and the normalisation mode.

The results of this alternative optimisation are shown in the Fig. A.1. The found maximal values of the Punzi figure of merit are equivalent to those found with the previously described nominal approach in Section 5.3.4.

While the selection criteria resulting from this alternative optimisation increases even further the similarity between the signal and the normalisation modes, it also leads to a significant reduction of number of signal events in the DD samples. To be specific, combined Run 2 samples contain 350 events if the alternative selection is used. This represents only a small fraction of the 1793 events selected with the nominal selection implying higher statistical

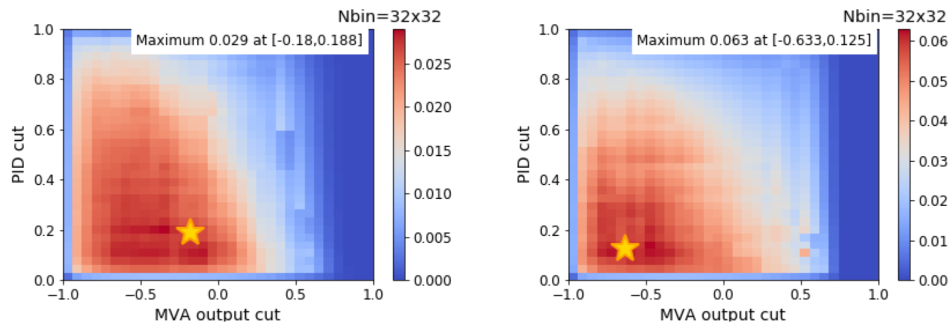

(a) DD track sample for $\Lambda_b^0 \to \Lambda K^+ K^-$. (b) LL track sample for $\Lambda_b^0 \to \Lambda K^+ K^-$.

Figure A.1 – Resulting alternative cut values from Punzi figure of merit across the 2-dimension optimisation plane. The S_{MVA} values are in the normalisation mode set to be equal to the optimal values found in the signal model in Section 5.3.4.

uncertainties which are already expected to dominate over the systematic ones. Therefore, this alternative selection is used only for purposes of L0 trigger efficiency corrections (see Section 5.15.

A.2 Complete summaries of Gaussian parameters characterising the distributions in the toy studies

This section summarises the complete lists of parameters characterising distributions in the toy studies in the two signal regimes - a regime with expected signal contribution (see Tables A.1 and A.2) and a regime with no signal contribution (see Tables A.3 and A.4) - as discussed in Section 5.7.3 in order to provide a complete overview of the fit outcome.

Table A.1 – Summary of Gaussian parameters characterising the toy studies distributions with DD samples in expected signal regime.

	Generator	Values		Errors		Pulls	
		μ^{Gauss}	σ^{Gauss}	μ^{Gauss}	σ^{Gauss}	μ^{Gauss}	σ^{Gauss}
$\mu_{\Lambda_b^0}$	5619.2	5619.0	0.8924	0.8916	0.074	0.00	1.00
$\sigma_{\Lambda_b^0}$	13.53	13.53	0.8923	0.8824	0.093	-0.06	1.01
$p^{\Lambda K^+K^-}$	-0.001	-0.001	0.0002	0.00021	0.00001	-0.01	0.98
$N_{Tot}^{\Lambda_b^0\to\Lambda K^+K^-}$	314.86	315.30	23.18	23.130	0.753	-0.01	1.02
$f_{15}^{\Lambda_b^0\to\Lambda K^+K^-}$	0.0467	0.0471	0.0126	0.01234	0.00128	-0.06	1.04
$f_{16}^{\Lambda_b^0\to\Lambda K^+K^-}$	0.3085	0.3090	0.0274	0.02704	0.00119	0.01	1.02
$f_{17}^{\Lambda_b^0\to\Lambda K^+K^-}$	0.3251	0.3231	0.0279	0.02750	0.00118	-0.09	1.02
$N_{15}^{misrec.}$	9.5	8.7	7.8	7.57	0.62	-0.14	1.03
$N_{16}^{misrec.}$	33.8	32.1	21.7	21.57	0.83	-0.09	1.01
$N_{17}^{misrec.}$	45.1	43.2	23.3	23.20	0.87	-0.08	1.00
$N_{18}^{misrec.}$	26.1	25.0	22.8	23.69	0.91	-0.05	0.97
$N_{15}^{comb.,\Lambda K^+K^-}$	59.2	56.5	10.7	10.63	0.99	-0.34	1.05
$N_{16}^{comb.,\Lambda K^+K^-}$	395.8	395.1	30.1	30.16	1.23	-0.06	1.01
$N_{17}^{comb.,\Lambda K^+K^-}$	433.2	436.9	31.9	32.00	1.26	0.08	0.99
$N_{18}^{comb.,\Lambda K^+K^-}$	475.5	474.1	33.3	33.33	1.24	-0.08	1.01
$N_{15}^{comb.,\Lambda p\bar{p}}$	17.0	20.1	4.7	4.67	0.54	0.54	0.97
$N_{16}^{comb.,\Lambda p\bar{p}}$	101.3	101.8	11.4	10.71	0.57	-0.01	1.03
$N_{17}^{comb.,\Lambda p\bar{p}}$	118.4	116.1	11.9	11.42	0.56	-0.25	1.03
$N_{18}^{comb.,\Lambda p\bar{p}}$	170.4	172.1	14.2	13.79	0.55	0.09	1.03
$p^{\Lambda p\bar{p}}$	-0.0014	-0.0014	0.0003	0.000256	0.000008	0.05	1.02
$R_{\Lambda_b^0}$	0.3671	0.3709	0.0491	0.0481	0.00513	-0.03	1.02
$R_{\Xi_b^0}$	0.0000	0.0001	0.0157	0.0152	0.00243	-0.13	1.08

Table A.2 – Summary of gaussian parameters characterising the toy studies distributions with LL samples in expected signal regime.

	Generator	Values		Errors		Pulls	
		μ^{Gauss}	σ^{Gauss}	μ^{Gauss}	σ^{Gauss}	μ^{Gauss}	σ^{Gauss}
$\mu_{\Lambda_b^0}$	5619.0	5619.0	0.8692	0.86	0.06	-0.01	1.00
$\sigma_{\Lambda_b^0}$	15.51	15.52	0.8039	0.78	0.06	-0.05	1.03
$p^{\Lambda K^+K^-}$	-0.002667	-0.002657	0.0004	0.0004	0.00003	-0.02	0.98
$N_{Tot}^{\Lambda_b^0\to\Lambda K^+K^-}$	354.8	356.2	21.1300	21.02	0.568	0.04	1.01
$f_{15}^{\Lambda_b^0\to\Lambda K^+K^-}$	0.070	0.074	0.0131	0.01	0.001	0.21	1.01
$f_{16}^{\Lambda_b^0\to\Lambda K^+K^-}$	0.285	0.284	0.0226	0.02	0.001	-0.05	1.00
$f_{17}^{\Lambda_b^0\to\Lambda K^+K^-}$	0.322	0.323	0.0244	0.02	0.001	-0.01	1.04
$N_{15}^{misrec.}$	1.00	0.97	4.84	4.59	0.85	-0.05	1.08
$N_{16}^{misrec.}$	3.00	3.14	13.91	13.75	0.92	0.00	1.01
$N_{17}^{misrec.}$	3.00	2.821	11.86	11.68	0.86	-0.03	1.03
$N_{18}^{misrec.}$	3.00	3.04	14.03	13.91	0.90	-0.02	1.01
$N_{15}^{comb.,\Lambda K^+K^-}$	14.9	14.9	6.79	6.09	1.26	-0.20	1.14
$N_{16}^{comb.,\Lambda K^+K^-}$	127.7	127.1	18.83	18.55	1.25	-0.09	1.03
$N_{17}^{comb.,\Lambda K^+K^-}$	91.2	91.1	15.22	15.68	1.21	-0.08	0.99
$N_{18}^{comb.,\Lambda K^+K^-}$	129.4	128.9	18.60	18.74	1.22	-0.09	1.02
$N_{15}^{comb.,\Lambda p\bar{p}}$	11.6	14.8	4.30	4.10	0.55	0.63	0.96
$N_{16}^{comb.,\Lambda p\bar{p}}$	44.9	44.79	7.32	7.32	0.59	-0.06	1.06
$N_{17}^{comb.,\Lambda p\bar{p}}$	40.0	40.31	7.28	7.01	0.64	-0.05	1.05
$N_{18}^{comb.,\Lambda p\bar{p}}$	42.4	40.87	7.46	7.05	0.64	-0.30	1.05
$p^{\Lambda p\bar{p}}$	-0.0020	-0.0020	0.0005	0.0005	0.00003	0.02	1.01
$R_{\Lambda_b^0}$	0.3420	0.3478	0.0401	0.0401	0.004	0.06	1.00
$R_{\Xi_b^0}$	0.0000	-0.0002	0.0105	0.0091	0.002	-0.17	1.14

Table A.3 – Summary of Gaussian parameters characterising the toy studies distributions with DD samples in no signal regime.

	Generator	Value		Errors		Pulls	
		μ^{Gauss}	σ^{Gauss}	μ^{Gauss}	σ^{Gauss}	μ^{Gauss}	σ^{Gauss}
$\mu_{\Lambda_b^0}$	5617.4	5617	1.19	1.16	0.116	0.05	1.04
$\sigma_{\Lambda_b^0}$	13.61	13.63	1.10	1.08	0.133	-0.08	1.03
$p^{\Lambda K^+K^-}$	-0.001130	-0.001125	0.0002	0.0002	0.00001	-0.02	1.02
$N_{Tot}^{\Lambda_b^0\to\Lambda K^+K^-}$	316.6	317.3	24.22	23.68	0.832	0.00	1.03
$f_{15}^{\Lambda_b^0\to\Lambda K^+K^-}$	0.03087	0.03038	0.01	0.01	0.002	-0.12	1.03
$f_{16}^{\Lambda_b^0\to\Lambda K^+K^-}$	0.3107	0.3094	0.03	0.03	0.002	-0.06	1.05
$f_{17}^{\Lambda_b^0\to\Lambda K^+K^-}$	0.3455	0.3458	0.03	0.03	0.002	-0.01	1.04
$N_{15}^{misrec.}$	8.81	8.51	8.09	7.82	0.611	-0.08	1.04
$N_{16}^{misrec.}$	29.89	28.52	21.71	21.61	0.848	-0.06	1.00
$N_{17}^{misrec.}$	41.04	38.86	23.40	23.05	0.859	-0.10	1.02
$N_{18}^{misrec.}$	21.85	19.87	23.84	23.80	0.903	-0.07	0.99
$N_{15}^{comb.,\Lambda K^+K^-}$	61.36	61.23	11.16	11.09	1.011	-0.10	1.04
$N_{16}^{comb.,\Lambda K^+K^-}$	399.0	398.9	30.97	30.33	1.250	-0.04	1.03
$N_{17}^{comb.,\Lambda K^+K^-}$	434.5	433.2	32.79	31.89	1.293	-0.08	1.04
$N_{18}^{comb.,\Lambda K^+K^-}$	480.0	481.2	33.77	33.62	1.240	0.01	1.02
$N_{15}^{comb.,\Lambda p\bar{p}}$	14.00	14.03	3.72	3.73	0.485	-0.14	1.05
$N_{16}^{comb.,\Lambda p\bar{p}}$	102.1	103.0	11.13	10.40	0.533	0.03	1.01
$N_{17}^{comb.,\Lambda p\bar{p}}$	117.5	117.6	12.04	11.15	0.527	-0.01	1.01
$N_{18}^{comb.,\Lambda p\bar{p}}$	174.5	175.0	14.10	13.44	0.519	0.02	1.01
$p^{\Lambda p\bar{p}}$	-0.001457	-0.001448	0.0003	0.0003	0.00001	0.03	1.01
$R_{\Lambda_b^0}$	0.000000	-0.00034	0.02	0.02	0.002	-0.15	1.09
$R_{\Xi_b^0}$	0.000000	-0.000278	0.02	0.02	0.002	-0.16	1.12

Table A.4 – Summary of Gaussian parameters characterising the toy studies distributions with LL samples in no signal regime.

	Generator	Values		Errors		Pulls	
		μ^{Gauss}	σ^{Gauss}	μ^{Gauss}	σ^{Gauss}	μ^{Gauss}	σ^{Gauss}
$\mu_{\Lambda_b^0}$	5618.5	5619	1.07	1.06	0.080	-0.01	1.03
$\sigma_{\Lambda_b^0}$	15.80	15.78	0.94	0.93	0.085	-0.07	1.03
$p^{\Lambda K^+K^-}$	-0.00269	-0.00267	0.0004	0.0004	0.00003	-0.02	1.02
$N_{Tot}^{\Lambda_b^0\to\Lambda K^+K^-}$	356.5	356.1	20.93	21.18	0.572	-0.03	1.01
$f_{15}^{\Lambda_b^0\to\Lambda K^+K^-}$	0.0552	0.0547	0.01	0.01	0.001	-0.14	1.05
$f_{16}^{\Lambda_b^0\to\Lambda K^+K^-}$	0.2858	0.2857	0.03	0.03	0.001	-0.03	1.02
$f_{17}^{\Lambda_b^0\to\Lambda K^+K^-}$	0.3253	0.3257	0.03	0.03	0.001	0.00	0.99
$N_{15}^{misrec.}$	1.000	0.997	4.86	4.66	0.808	-0.04	1.04
$N_{16}^{misrec.}$	3.000	2.924	14.35	13.83	0.918	-0.02	1.04
$N_{17}^{misrec.}$	3.000	2.416	11.84	11.76	0.907	-0.06	1.01
$N_{18}^{misrec.}$	3.000	3.353	14.18	14.00	0.922	0.02	1.02
$N_{15}^{comb.,\Lambda K^+K^-}$	15.47	15.54	6.55	6.25	1.226	-0.19	1.14
$N_{16}^{comb.,\Lambda K^+K^-}$	128.2	127.9	18.36	18.65	1.224	-0.07	1.00
$N_{17}^{comb.,\Lambda K^+K^-}$	91.4	91.58	15.98	15.77	1.263	-0.06	1.02
$N_{18}^{comb.,\Lambda K^+K^-}$	129.0	128.2	18.99	18.77	1.258	-0.09	1.03
$N_{15}^{comb.,\Lambda p\bar{p}}$	12.69	13.17	3.92	3.62	0.500	-0.02	1.07
$N_{16}^{comb.,\Lambda p\bar{p}}$	43.97	45.11	7.22	6.89	0.578	0.09	1.05
$N_{17}^{comb.,\Lambda p\bar{p}}$	42.98	44.86	7.06	6.91	0.554	0.21	1.00
$N_{18}^{comb.,\Lambda p\bar{p}}$	42.75	44.0	7.03	6.87	0.566	0.12	1.05
$p^{\Lambda p\bar{p}}$	-0.00196	-0.00195	0.0005	0.0004	0.00003	0.03	1.03
$R_{\Lambda_b^0}$	0.0000	0.00038	0.01	0.01	0.002	-0.09	1.08
R_{Ξ}	0.0000	-0.00044	0.01	0.01	0.002	-0.20	1.13

Bibliography

[1] D. Perkins, **Introduction to High Energy Physics, 4nd Edition**, Cambridge University Press, 2000.

[2] W.N. Cottinham, D.A Greenwood **An Introduction to the Standard Model of Particle Physics**, Cambridge University Press, 2007.

[3] ATLAS Collaboration, **Observation of a new particle in the search for the Standard Model Higgs boson with the ATLAS detector at the LHC** Physics Letters B, 716, 2012.

[4] The CMS Collaboration, **Observation of a new boson at a mass of 125 GeV with the CMS experiment at the LHC**, Physics Letters B, Volume 716, Issue 1, 2012.

[5] L. Canetti, M. Drewes and M. Shaposhnikov, **Matter and antimatter in the universe**, New Journal of Physics, Vol. 14, 2012.

[6] Particle Data Group, P.A. Zyla et al.*et al.,* **Review of Particle Physics**, PTEP, 2020.

[7] G. Bertone, D. Hooper, J. Silk **Particle Dark Matter: Evidence, Candidates and Constraints**, Phys.Rept.405:279-390, 2005.

[8] C. Q. Geng, Y. K. Hsiao and E. Rodrigues, **Exploring the simplest purely baryonic decay processes**, Phys. Rev. D 94, 014027, 2016.

[9] H. Clement, **On the History of Dibaryons and their Final Observation**, Prog. Part. Nucl. Phys. 93 195, 2017.

[10] J. Vijande, A. Valcarce and J. M. Richard, **Stability of hexaquarks in the string limit of confinement** Phys. Rev. D 85, 014019, 2012.

[11] ATLAS, CMS Collaborations, **Combined Measurement of the Higgs Boson Mass in pp Collisions at** $\sqrt{s} = 7$ **and 8 TeV with the ATLAS and CMS Experiments**, Phys. Rev. Lett. 114, 2015.

[12] M. Lubej, **The Standard Model image**, "https://www.physik.uzh.ch/groups/serra/StandardModel.html", 2015.

[13] LHCb collaboration, **Observation of the decay** $\Lambda_b^0 \to \Lambda_c^+ p\overline{p}\pi^-$, Physics Letters B, 2018.

[14] Y. K. Hsiao, C. Q. Geng and E. Rodrigues, **Baryon decays to purely baryonic final states**, Scientific Reports, 2019.

[15] M. S. Sozzi and I. Mannelli, **Measurements of direct CP violation**, Riv.Nuovo Cim., 2003.

[16] KTeV Collaboration Collaboration, **Precise Measurements of Direct CP Violation, CPT Symmetry, and Other Parameters in the Neutral Kaon System**, 2010.

[17] BaBar and Belle collaborations, **The physics of the B factories**, Eur. Phys. J.C74, 3026, 2014.

[18] LHCb collaboration, **First observation of a baryonic B_s^0 decay**, Phys. Rev. Lett.119, 041802, 2017.

[19] LHCb collaboration, **Observation of charmless baryonic decays $B_s^0 \to p\bar{p}h^+h^{'-}$**, Phys. Rev.D96, 051103, 2017.

[20] LHCb Collaboration, **Observations of $\Lambda_b^0 \to \Lambda K^+\pi^-$ and $\Lambda_b^0 \to \Lambda K^+K^-$ decays and searches for other Λ_b^0 and Ξ_b^0 decays to Λh^+h^- final states**, JHEP 05 081, 2016.

[21] L. Evans and P. Bryant (editors), **LHC machine**, JINST 3 S08001, 2008.

[22] CERN Graphics, **"https://cds.cern.ch/record/2684277"**, 2016.

[23] LHCb Collaboration, **The LHCb Detector at the LHC**, JINST 3 S08005, 2008.

[24] LHCb Collaboration, **Performance of the LHCb Vertex Locator**, JINST 9 P09007, 2014.

[25] LHCb Collaboration, **LHCb VELO TDR: Vertex locator. Technical design report**, CERN-LHCC-2001-011, 2001.

[26] C. Abellan Beteta et al, **Monitoring radiation damage in the LHCb Tracker Turicensis**, JINST 15 P08016, 2020.

[27] The LHCb Outer Tracker group, **Performance of the LHCb Outer Tracker**, JINST 9 P01002, 2014.

[28] LHCb collaboration, **LHCb magnet: Technical design report**, CERN-LHCC-2000-00, 2000.

[29] The LHCb Collaboration, **LHCb detector performance**, International Journal of Modern Physics A Vol. 30, No. 07, 1530022, 2015.

[30] C. Abellán Beteta et al, **Calibration and performance of the LHCb calorimeters in Run 1 and 2 at the LHC**, arXiv:2008.11556 CERN-LHCb-DP-2020-001, 2020.

[31] A. Puig Navarro, **First measurements of radiative B decays in LHCb**, CERN-THESIS-2012-025, 2012.

[32] J.P.Baud et al., **The LHCb Data Management System**, Journal of Physics: Conference Series 396, 2012.

[33] M. Clemencic et al., **The LHCb Simulation Application, Gauss: Design, Evolution and Experience**, J. Phys. Conf. Ser.331 032023, 2011.

[34] T. Sjostrand, S. Mrenna, and P. Z. Skands, **A Brief Introduction to PYTHIA 8.1**, Computer Physics Communications 178 852, 2008.

[35] D. J. Lange, **The EvtGen Particle Decay Simulation Package**, Nucl. Instrum. Meth.A462, 2001.

[36] P. Golonka and Z. Was, **PHOTOS Monte Carlo: A Precision Tool for QED Corrections in Z and W decays**, The European Physical Journal C - Particles and Fields volume 45, 2006.

[37] J. Allison et al, **Geant4 Developments and Applications**, IEEETrans. Nucl. Sci.53 270, 2006.

[38] LHCb Collaboration, LHCb operations webpage, **"http://lhcb-public.web.cern.ch/Images2015/Images2018/IntRecLumiR12.png"**, 2018.

[39] LHCb Collaboration, **Implications of LHCb measurements and future prospects**, The European Physical Journal C , Vol. 73 10.1140, 2013.

[40] LHCb Collaboration, **Framework TDR for the LHCb Upgrade: Technical Design Report**, CERN-LHCC-2012-007 LHCb-TDR-12, 2012.

[41] LHCb Collaboration, **LHCb Trigger and Online Upgrade Technical Design Report**, CERN-LHCC-2014-016, LHCB-TDR-016, 2014.

[42] LHCb Collaboration, **LHCb VELO Upgrade Technical Design Report**, CERN-LHCC-2013-021, LHCB-TDR-013, 2013.

[43] LHCb Collaboration, **LHCb Tracker Upgrade Technical Design Report**, CERN-LHCC-2014-001, LHCB-TDR-015, 2015.

[44] LHCb Collaboration, **LHCb technical design report: Reoptimized detector design and performance**, CERN-LHCC-2003-030, 2003.

[45] LHCb Collaboration, **LHCb: Inner tracker technical design report**, CERN-LHCC-2002-029, 2002.

[46] LHCb Collaboration, **LHCb: Outer tracker technical design report**, Phys. Rev. D 94, no. 1, 014027, 2016.

[47] LHC Commissioning page, **Longer term LHC schedule** "https://lhc-commissioning.web.cern.ch/schedule/LHC-long-term.htm", 2021.

[48] D. Blake on behalf of LHCb Collaboration, **Proceedings, 3rd International Conference on Technology and Instrumentation in Particle Physics (TIPP 2014)**, Amsterdam, Netherlands, June 2-6, 2014 PoS TIPP, 2014.

[49] R. H. Dalitz, **On the analysis of tau-meson data and the nature of the tau-meson**, Phil. Mag.44 1068, 1953.

[50] LHCb Collaboration, **Dalitz plot analysis of $B_s^0 \to \overline{D}^0 K^- \pi^+$ decays**, Phys. Rev., D90, 10.1103/PhysRevD.90.072003, 2014.

[51] S. Tolk et al, **Data driven trigger efficiency determination at LHCb**, CERN Document Server reports, 2014.

[52] W. D. Hulsbergen, **Decay chain fitting with a Kalman filter**, Nuclear Instruments and Methods in Physics Research Section A: Accelerators, Spectrometers, Detectors and Associated Equipment, Volume 552, Issue 3, 2005.

[53] Yandex open source projects and technologies, **Reproducible Experiment Platform** "https://yandex.github.io/rep/", 2016.

[54] Y. Jung, and J. Hu, **A K-fold Averaging Cross-validation Procedure**, Journal of Nonparametric Statistics, 2015.

[55] T. Chen and C. Guestrin. **XGBoost: A Scalable Tree Boosting System**, In Proceedings of the 22nd ACM SIGKDD International Conference on Knowledge Discovery and Data Mining. Association for Computing Machinery, New York, NY, USA, 785–794, 2016.

[56] F. J. Massey Jr., **The Kolmogorov-Smirnov Test for Goodness of Fit**, Journal of the American Statistical Association, 1951.

[57] D. Derkach et al, **Machine-Learning-based global particle-identification algorithms at the LHCb experiment**, J. Phys.: Conf. Ser.1085 042038, 2018.

[58] R. Van Rooyen et al, **AstroKAT and the MeerKAT observation framework** Proceedings Volume 11449, Observatory Operations: Strategies, Processes, and Systems VIII, 2020.

[59] G. Punzi, **Sensitivity of searches for new signals and its optimization**, Statistical Problems in Particle Physics, Astrophysics, and Cosmology, 2003.

[60] J. Podolanski and R. Armenteros. III. **Analysis of V-events**, The London, Edinburgh, and Dublin Philosophical Magazine and Journal of Science, 1954.

[61] G. Cowan, **Statistical Data Analysis**, Claredon press, Oxford, 1998.

[62] LHCb collaboration, **Analysis of $B^0 \to p\bar{p}$ and $B_s^0 \to p\bar{p}$ decays with the Run II LHCb data**, publication in preparation.

[63] LHCb Collaboration, **TrackCalib twiki pages** "https://twiki.cern.ch/twiki/bin/view/LHCb/TrackCalib", 2017.

[64] S. S. Wilks, , **The large-sample distribution of the likelihood ratio for testing composite hypotheses**, Ann. Math.Stat., 1938.

[65] O. Behnke et al, **Data Analysis in High Energy Physics**, Wiley, 2013.

[66] M. Pivk and F. R. Le Diberder, **Plots: A statistical tool to unfold data distributions**, Nuclear Instruments and Methods in Physics Research Section A: Accelerators, Spectrometers, Detectors and Associated Equipment 555, 2005.

[67] D. Martinez Santosa, F. Dupertuis, **Mass distributions marginalized over per-event errors** Nuclear Instruments and Methods in Physics Research Section A: Accelerators, Spectrometers, Detectors and Associated Equipment, 2014.

[68] LHCb Collaboration, **Measurement of the track reconstruction efficiency at LHCb**, Journal of Instrumentation, 2015.

[69] LHCb Collaboration **Unbinned PID resampling using kernel density estimation,** "https://twiki.cern.ch/twiki/bin/view/LHCb/MeerkatPIDResampling", 2017.

Vladimir Macko

✉ vmacko@protonmail.ch ☎ +41 779 166 558
Renens, Switzerland
Slovak nationality / Swiss Residence Permit B

Advanced in data science and data engineering with broad experience in presenting, communication and collaborative work, and keen interest in education, research and technology

Core experience & responsibilities

2016-2021 **Doctoral researcher at École Polytechnique Fédérale de Lausanne, Switzerland**
2016-2021 • High Energy Physics **research, analysis and software** development
2017-2019 • **Teaching** at the Bachelor and Master levels
2016-2018 • **Production quality assurance** for the construction of a scintillating fibre tracker

2014-2021 **Scientific collaborator at CERN (European Organization for Nuclear Research), Switzerland**
2016-2020 • Member of the LHCb collaboration
2016-2020 • **Data scientist and analyst** in the Charmless working group
Analyzing experimental and simulated events in order to discover very rare purely baryonic decays
2019-2020 • **Liaison delegate** for Statistics for the Charmless working group
Reporting and working on statistical questions raised in the Charmless working group
2017-2019 • **Liaison delegate** for Pattern recognition in LHCb collaboration
Reporting and working on machine learning tools used for particle identification
2016-2018 • **Operational data manager**
Responsable for data quality at the LHCb control centre during the data taking
2014-2016 • Member of the ATLAS collaboration
Focus on software improvements in flavour tagging and data analysis

2016 **Deutsches Elektronen-Synchrotron DESY Summer Student Programme**
2014-2015 **Erasmus student researcher at Stockholm University**
2014 **International student practice at Joint Institute of Nuclear Research of Russian Federation**
2013-2014 **Technical assistant at Department of Quantum Chemistry at Charles University in Prague**

Education

2016-2021 **PhD in High Energy Physics, École Polytechnique Fédérale de Lausanne, Switzerland**
Doctoral thesis: First indication of the Λ_b^0 baryon decay to a charmless baryonic final state
Advanced data analysis featuring Machine-learning based selections and modern statistical methods

2019-2020 **Français supérieur C1 axé sur l'écrit, Université populaire de Lausanne, Switzerland**
2019 **Analytics & Data Science Summer School (Deep learning track), University of Essex, United Kingdom**
2018 **Summer School on Machine Learning for High energy physics, University of Oxford, United Kingdom**
2018 **PSI Summer School on Particle Flavour Fever, Lyceum Alpinum Zuoz, Switzerland**
2017 **CHIPP Winter School of Particle Physics, Sörenberg, Switzerland**

2015-2016 **Master of Science in Physics (120 ETC), Stockholm University, Sweden**
Diploma thesis: Optimization of the JetFitter b-tagging algorithm in the ATLAS experiment in high pile-up conditions,
Analysis of the algorithm performance and assessment of impact of feasible adjustments
2011-2014 **Bachelor of Science in General Physics (180 ETC), Charles University in Prague, Czech Republic**

Programming languages, software & tools

Advanced in: Python, Tensorflow and Keras, Microsoft Office, Pandas, Anaconda, Jupyter, C/C++, ROOT/PyROOT and RooFit, Bash scripting, Git, MatLab, Linux distributions, LaTeX, Dirac Grid/Distributed computing (including Athena and Ganga), JIRA taskforce, Algorithm design,
Familiar with: PyTorch, Wolfram Mathematica, Borland Pascal, Docker, WordPress, OriginPro, Gnuplot, Molden

Publications & Conference contributions

2017-2021 **Author of 193 LHCb scientific publications as a collaboration member**
2021 **First indication of the Λ_b^0 baryon decay to a charmless baryonic final state**
(Publication in preparation)
2019 **LHCb results from Heavy quark spectroscopy, exotic states and QCD**
Lake Louise Winter Institute, Lake Louise, Canada
2018 **Author of winning solution of RAMP challenge on fast vertexing**
RAPID2018 Workshop, Dortmund, Germany
2018 **First steps towards the experimental observation of purely baryonic decay processes**
Swiss physics society Annual meeting Lausanne 2018, Lausanne, Switzerland
2017 **Production and Quality Assurance of Scintillating Fibre Detectors for the LHCb Upgrade**
Joint Annual Meeting of Swiss physics society and Austrian physics society, Genève, Switzerland
2016 **The JetFitter algorithm: Performance and Improvements**
ATLAS Flavour Tagging Workshop, Bonn, Germany
2015 **Performance of the JetFitter b-tagging algorithm in ATLAS in high pileup conditions**
Partikeldagarna 2015, Uppsala, Sweden

Languages

- English (fluent C2)
- French (proficient C1)
- German (Pre-Intermediate A2)
- Czech (fluent C2)
- Slovak (native)

Interests

- Data science challenges
- Project Management
- Algorithm development and Software design
- Online computing
- Data analysis and Statistics
- Machine learning
- Artificial intelligence
- Advanced research methods
- Education and Popular science